Manipulation of Si and Ge Crystallization

Thesis by

Chih M. Yang

In Partial Fulfillment of the Requirements

for the Degree of

Doctor of Philosophy

California Institute of Technology

Pasadena, California

1997

(Submitted December 20, 1996)

© 1997
Chih M. Yang
All Rights Reserved

Acknowledgements

I wish to thank Dr. Harry A. Atwater, my advisor. His enthusiasm for scientific knowledge and his understanding during difficult times has been inspirational. He has provided me with helpful advice as well as many opportunities in advancing my scientific career.

I thank Dr. Cho-Jen Tsai, Dr. James Im, Dr. Shouleh Nikzah, and Dr. Tom Walkman for their guidance and support during my early years as a graduate student.

I thank Rosalie Rowe for helping me with travel arrangements and reimbursements, and Pam Albertson for helping me with thesis presentation arrangements.

I am grateful for the cordial assistance of Channing Ahn and Carol Garland in performing transmission electron microscopy. I also wish to thank Mike Easterbrook for helping me with ion implantation and Rutherford backscattering spectrometry.

I am indebted to Dr. Hyun Joo, as well as my former colleagues, Dr. Imran Hashim, Dr. Ramana Murty, Dr. Selmer Wong, and Dr. Jung Shin, with whom I had many stimulating discussions, scientific and otherwise.

I am grateful for the friendship, loyalty, and support of Gang He, Maggie Taylor, and Claudine Chen. I thank Kirill Shcheglov and Kyu Min for our fruitful collaboration in the nanocrystal experiments. I would also like to acknowledge my colleagues Renato Camata, Joseph Christopherson, Elizabeth Boer, Regina Ragan, and Geraldine Nogaki, for making graduate school a more pleasant place for me.

I wish to thank Ellis Meng, who spent many hours helping me with the germanium crystallization experiment.

Last but not least, I thank my parents, as well as my brother and sister, for their continued support of my education. In particular, I want to express my love for my mother, who was the source of my inspiration, and the kindest, most loving person I have ever known.

Abstract

This thesis discusses methods for altering the crystallization kinetics of Si and Ge in order to obtain large-grained polycrystalline semiconductor thin films or size-selected semiconductor nanocrystals in silicon dioxide. Reduction of grain boundaries in polycrystalline semiconductor thin films is important for improving the performance of microelectronic devices because grain boundaries act as traps for charge carriers. Control of nanocrystal size and concentration in silicon dioxide is important in controlling the nanocrystal photoluminescence and electroluminescence characteristics. Results of modification of crystal nucleation and growth rate via ion beam irradiation, thermal annealing, metal-induced crystallization, and dopant enhanced solid phase epitaxy are presented.

Ion beam irradiation was used to induce amorphization of 1–50 nm Si crystals in amorphous Si. A size-dependent amorphization rate was calculated from the temporal evolution of the crystal size distribution under ion irradiation. A model for irradiation-induced, size-dependent crystal growth/amorphization is developed and it shows good quantitative agreement with the present experiment as well as other experiments.

Precipitation of 1–10 nm Ge nanocrystals and 1–2 nm Si nanocrystals in silicon dioxide was accomplished by ion implantation followed by thermal annealing. Nucleation of 1–2 nm Ge nanocrystals occurred during implantation, and annealing at temperatures higher than 600 °C induced coarsening. Increasing the Ge implantation dose resulted in increased nanocrystal concentration but not size. In contrast, no Si nanocrystals were observed in as-implanted samples or samples annealed at less than 1000 °C. Samples annealed at 1000 °C for 40 min contained 1–2 nm Si nanocrystals.

Large grained polycrystalline Ge thin films, with controlled grain location and size, were synthesized at low temperatures. Grain sizes of 10–20 μm in 50-nm-thick amorphous Ge were obtained at temperatures less than 475 °C, which represents a two-orders-of-magnitude improvement over previous efforts. Selective nucleation

was achieved by deposition of an array of 5-micron-diameter metal islands on top of amorphous Ge and annealing at low temperatures. During subsequent anneal at higher temperatures crystals that selectively nucleated underneath the metal islands grew tens of microns before random nucleation impeded their growth. The crystal growth rate was enhanced by doping Ge with B or P, resulting in even larger crystal sizes.

List of Publications

1. “Size-Dependent Evolution of Si Crystals in Amorphous Si under Ion Irradiation,” C. M. Yang and H. A. Atwater, to be submitted to J. of Appl. Phys..

2. “Selective Solid Phase Crystallization for Control of Grain Size and Location in Ge Thin Films on Silicon Dioxide,” C. M. Yang and H. A. Atwater, Appl. Phys. Lett. **68**, 3392 (1996).

3. “Correlation of Size and Photoluminescence for Ge Nanocrystals in SiO_2 Matrices,” C. M. Yang, K. V. Shcheglov, K. J. Vahala and H. A. Atwater, Nucl. Instr. and Meth. in Phys. Res. B **106**, 433 (1995).

4. “Correlation of Size and Photoluminescence for Ge Nanocrystals in SiO_2 Matrices,” C. M. Yang, K. V. Shcheglov, M. L. Brongersma, A. Polman, and H. A. Atwater, Mater. Res. Soc. Symp. Proc. **358**, 181 (1995).

5. “Defect-Related versus Excitonic Visible Light Emission from Ion Beam Synthesized Si Nanocrystals in SiO_2,” K. S. Min, K. V. Shcheglov, C. M. Yang, H. A. Atwater, M. L. Brongersma, and A. Polman, Appl. Phys. Lett. **69**, 2033 (1996).

6. “The Role of Quantum-Confined Excitons vs Defects in the Visible Luminescence of SiO_2 Films Containing Ge Nanocrystals,” K. S. Min, K. V. Shcheglov, C. M. Yang, H. A. Atwater, M. L. Brongersma, and A. Polman, Appl. Phys. Lett. **68**, 2511 (1996).

7. ‘Electroluminescence and Photoluminescence of Ge-Implanted $Si/SiO_2/Si$ Structures,” K. V. Shcheglov, C. M. Yang, K. J. Vahala, and H. A. Atwater, Appl. Phys. Lett. **66**, 745 (1994).

8. "Stability of Nanometer-Size Si Crystals in Amorphous Si Thin Films Under Ion Irradiation," C. M. Yang and H. A. Atwater, Mat. Res. Soc. Symp. Procs. **311**, 185 (1993).

Contents

Acknowledgements iii

Abstract iv

List of Publications vi

1 Introduction 1

2 Size-Dependent Evolution of Si Crystals in Amorphous Si Under Ion Irradiation 4

2.1 Introduction 4

2.2 Background 6

2.2.1 Solid phase epitaxy 6

2.2.2 Ion beam induced solid phase epitaxy 9

2.3 Experiment 12

2.3.1 Calculation of growth rate 18

2.3.2 Uncertainties in computing growth rate 23

2.4 Model 26

2.4.1 Jackson's model for ion beam induced solid phase epitaxy . . 26

2.4.2 A model for size-dependent ion beam induced crystal evolution 31

2.4.3 Critical radius under ion irradiation 37

2.5 Comparison of model to data 40

2.5.1 Data from present experiment 40

2.5.2 Data for ion beam induced crystal growth 45

2.6 Discussion 49

2.6.1 Spinella's model 49

2.6.2 Nucleation under ion irradiation 50

2.6.3 Activation energy for defect migration 50

2.7 Summary 52

3 Synthesis of Ge and Si Nanocrystals in SiO_2 via Ion Implantation and Precipitation 56

3.1 Introduction 56

3.2 Background 58

3.2.1 Ge and Si nanocrystal precipitation in SiO_2 58

3.2.2 Ostwald ripening 60

3.3 Experiment and results 60

3.3.1 Ge-implanted samples 61

3.3.2 Si-implanted samples 76

3.4 Discussion 79

3.4.1 Ge nanocrystal nucleation 79

3.4.2 Coarsening of Ge nanocrystals 80

3.4.3 Si nanocrystal precipitation 83

3.5 Summary 83

4 Selective Solid Phase Crystallization with Controlled Grain Size and Location in Ge Thin Films on Silicon Dioxide 87

4.1 Introduction 87

4.2 Methods of selective solid phase crystallization of Si and Ge 89

4.2.1 Ion irradiation 89

4.2.2 Metal-induced crystallization 92

4.3 Experiment and Results 93

4.4 Discussion 111

4.4.1 Metal-induced heterogeneous nucleation 111

4.4.2 Possible methods for obtaining one crystal per nucleation site 115

4.4.3 Methods for increasing ultimate grain size 116

4.5 Summary 117

A Program for Calculating Crystal Evolution Under Ion Irradiation **122**

A.1 Description 122

A.2 Source code 122

B Program for Calculating Time-Dependent Nucleation **130**

B.1 Introduction 130

B.2 Description 130

B.3 Sample outputs 130

B.4 Algorithm 131

B.5 Source code 142

List of Figures

2.1 Schematic of a $[1\bar{1}0]$ ledge on a $(11\bar{1})$ terrace separating the crystalline phase from the amorphous phase in Si 7

2.2 Interface displacement rate for various temperatures and ion fluxes for 1.5 MeV xenon ions 9

2.3 Dose rate dependence of the temperature for zero growth rate for 1.5 MeV Xe^+, Kr^+, Ar^+, and Ne^+ bombardments of Si 10

2.4 Bright field transmission electron micrographs of polycrystalline Si samples irradiated with various Ar^+ ion doses 14

2.5 The corresponding dark field transmission electron micrographs of samples shown in Fig. 2.4 15

2.6 High-resolution transmission electron micrographs of Si crystals in a film irradiated with 4×10^{15} ions/cm^2 17

2.7 A plot of the evolution of the crystal size distribution under ion irradiation 18

2.8 A plot of the variation of crystal density and average size with ion dose 19

2.9 Random and (100)-aligned backscattering spectra of 2 MeV $^4He^{++}$ ions incident on a sample before and after it was subjected to Ar^+ ion irradiation 20

2.10 Calculated growth velocity as a function of size 23

2.11 Schematic of the creation of defects by ions as they traverse through a Si sample 28

2.12 Schematic of defect concentration as a function of time 30

2.13 Free energy diagram of the reaction path of a defect 33

2.14 Schematic of size as a function of time for a grain under ion irradiation 36

2.15 Calculated growth rate as a function of size at various temperatures for the same experimental conditions as those in Figs. 2.4–2.6 38

2.16 Calculated growth rate as a function of size (from Fig. 2.10) and a fit from the present model 41

2.17 Plot of x as a function of radius 42

2.18 Plot of the critical radius as a function of temperature 43

2.19 Calculated and measured grain size distributions for ion beam induced amorphization 44

2.20 Calculated and measured grain size distributions for ion beam induced crystal growth 46

2.21 Critical size under ion irradiation, as a function of temperature 47

3.1 Room temperature visible photoluminescence spectra of 100 nm SiO_2 films 57

3.2 An illustration of the structure of silica 59

3.3 High-resolution transmission electron micrographs of Ge nanocrystals in 90 nm-thick SiO_2 implanted with 1.6×10^{16} /cm^2 70 keV $^{74}Ge^+$ . . 62

3.4 Bright field transmission electron micrographs of Ge nanocrystals in SiO_2 thin films implanted with 1.6×10^{16} Ge/cm^2, and then annealed for 40 min at various temperatures 63

3.5 Cross-sectional electron micrograph of a sample implanted with 1.6×10^{16} Ge/cm^2 and then annealed at 800 °C for 40 min 64

3.6 Germanium nanocrystal size distributions in SiO_2 films implanted with 1.6×10^{16} Ge/cm^2 and then annealed for 40 min at various temperatures 65

3.7 Bright field transmission electron micrographs of 1.6×10^{16} Ge/cm^2-implanted samples annealed at 1000 °C for various durations 67

3.8 A plot of the average nanocrystal radius $\bar{r}$ vs. isothermal annealing time for 1.6×10^{16} Ge/cm^2-implanted samples annealed at 1000 °C . 68

3.9 Bright field transmission electron micrograph of samples implanted with 1.6×10^{16} Ge/cm^2 or 3.6×10^{16} Ge/cm^2, then annealed at 1000 °C for 40 min 70

3.10 Rutherford backscattering spectrum of a sample implanted with 2×10^{16} Ge/cm^2 71

3.11 Rutherford backscattering spectra of samples implanted with various doses and then annealed at various temperatures 72

3.12 Concentration of Ge atoms as a function of film depth at various annealing temperatures for 1.6×10^{16} Ge/cm^2-implanted samples 73

3.13 Concentration of Ge atoms as a function of film depth for samples implanted with various doses and then annealed for 40 min at 1000 °C 74

3.14 Germanium-silicon binary phase diagram 75

3.15 Schematic of the chemical potential of Ge and Si atoms as a function of depth 76

3.16 High resolution transmission electron micrographs of samples implanted with Si or Ge at 1.6×10^{16} /cm^2 or 3.6×10^{16} /cm^2, then annealed at 1000 °C for 40 min 77

3.17 High resolution transmission electron micrographs of samples shown in the Fig. 3.16, except at a lower magnification 78

4.1 Schematic of a GaAs thin-film solar cell on top of a layer of Ge thin film, deposited on glass substrate 88

4.2 An illustration of the present approach for selective solid phase crystallization 90

4.3 In-Ge and Cu-Ge binary phase diagram 94

4.4 Optical micrograph of a glass slide with a 20-nm-thick In film on top, evaporated through a mechanical mask 95

4.5 Bright field transmission electron micrograph of 50-nm-thick Ge film annealed at 475 °C for 5 min, 20 min, or 40 min 97

4.6 Transmission electron diffraction pattern of 50-nm-thick Ge film annealed for 60 min at 425 °C, 450 °C, or 475 °C 98

4.7 Bright field transmission electron micrograph of 20-nm-thick Ge film with 20-nm-thick 5-μm-diameter Au, Cu, or In island on top, annealed at 350 °C for 20 min 100

4.8 Dark field transmission electron micrograph of 20-nm-thick Ge film with 20-nm-thick 5-μm-diameter Au, Cu, or In island on top, annealed at 350 °C for 20 min 101

4.9 Bright field and Dark field electron micrograph of 50-nm-thick Ge film with 20-nm-thick In island on top, annealed for 20 min at 350 °C . . 103

4.10 Bright field transmission electron micrograph illustrating selective nucleation and growth of Ge grains in a 50-nm-thick amorphous Ge film on SiO_2 104

4.11 Dark field micrographs of undoped and B-doped 50-nm-thick Ge film with 20-nm-thick In islands on top, annealed at 350 °C for 20 min and then 425 °C for 2 hr 105

4.12 Dark field micrographs of undoped and P-doped 50-nm-thick Ge film with 20-nm-thick In islands on top, annealed at 350 °C for 20 min and then 425 °C for 2 hr 106

4.13 Bright field and dark field micrograph of a nucleation site for selective nucleation and growth in a 50-nm-thick P-doped amorphous Ge film on SiO_2 107

4.14 Optical micrograph of 100-nm-thick a-Ge on SiO_2, implanted with 50 keV $^{31}P^+$ to a dose of 2×10^{15} at./cm^2, and then annealed at 400 °C for 100 min 108

4.15 Arrhenius plot of lateral solid phase epitaxial growth rate in 50 nm amorphous Ge films on SiO_2 109

4.16 Arrhenius plot of lateral solid phase epitaxial growth rate in 50 nm amorphous Ge films, undoped, B-doped, P-doped, or doped with both B and P, on SiO_2 110

4.17 Schematic of homogeneous nucleation vs. heterogeneous nucleation . . 111

4.18 Incubation time for crystal nucleation in 20 nm and 50 nm pure amorphous Ge at various temperatures 113
4.19 Illustration of possible mechanisms for metal-induced crystallization in Ge 115
4.20 Scenarios of In island deposition on amorphous Ge 116
4.21 Illustration of Ge crystal seed selection by patterned removal of amorphous Ge 117

B.1 Temporal evolution of nuclei population 131
B.2 Temporal evolution of nuclei flux 132
B.3 Temporal evolution of nuclei population 133
B.4 Temporal evolution of nuclei flux 134
B.5 Temporal evolution of nuclei population 135
B.6 Temporal evolution of nuclei flux 136
B.7 Nucleation rate during temperature oscillation 137

List of Tables

2.1 Table of the crystal size distributions shown in Fig. 2.7 21

3.1 Table of the average nanocrystal diameter, the standard deviation of nanocrystal diameter, the nanocrystal concentration, the inter-crystal distance, and the concentration of Ge atoms contained in the nanocrystals, for the size distributions shown in Fig. 3.6 65

3.2 Table of the minimum diffusion coefficient of Ge atoms in amorphous silica at various temperatures 68

4.1 Table of the metal-induced lowering of the crystallization temperature of 20 nm Ge thin films 96

Chapter 1 Introduction

Methods for altering the crystallization kinetics of Si and Ge in order to obtain large-grained polycrystalline semiconductor thin films or size-selected semiconductor nanocrystals inside dielectrics are of great technological interest. Reduction of grain boundaries in polycrystalline semiconductor thin films on amorphous substrates is important for improving the performance and reliability of microelectronic devices because grain boundaries act as traps for charge carriers. Furthermore, semiconductor devices such as photovoltaic cells and thin-film transistors in active matrix liquid crystal displays (AMLCD's) require the use of low cost substrates in order to be economically viable compared to other methods of energy production or devices for information display. Thus, crystallization of amorphous Si or Ge thin films must be performed below the softening temperatures of the substrates (most likely glass). Control of semiconductor nanocrystal size and concentration in silicon dioxide is important in controlling the nanocrystal photoluminescence and electroluminescence characteristics, which is critical for potential optoelectronic applications. In this thesis, results of modification of crystal nucleation and growth rate via ion beam irradiation, thermal annealing, metal-induced crystallization, and dopant enhanced solid phase epitaxy are presented.

Ion irradiation is one of the most widely used tools for modification of solid phase Si crystallization processes. It has been used to induce nucleation, suppress nucleation, induce growth, and induce amorphization. The optimal use of ion irradiation in the above processes requires an understanding of the dependence of crystal growth/amorphization rate on parameters such as crystal size, substrate temperature, ion energy, flux, and species. Although a model has been proposed in the past for this purpose, it has not been tested rigorously due to the fact that size-dependent growth rates have never been determined experimentally—usually only the crystal size distributions are reported. Instead, the size dependence of the growth/amorphization

rate has been inferred from the fact that in some irradiation experiments, the crystal sizes increased but the number of crystals decreased. The purpose of Chapter 2 is twofold: (1) show that crystal evolution rate as a function of size can be calculated from the crystal size distribution, and (2) develop a model and test it against the current experiment as well as other experiments. The size-dependent amorphization rate of 4–50 nm Si crystals in amorphous Si under 250 KeV Ar^+ irradiation at 170 °C was obtained by analyzing the temporal evolution of the crystal size distribution using a continuity equation. It indicates that the amorphization rate increases dramatically for crystals smaller than 10 nm. A new model is developed whose predicted crystal size distributions show excellent quantitative agreement with the size distributions in current experiment as well as those in other experiments. The differences between the current model and the previous model are discussed.

The usage of group IV semiconductors such as Si and Ge in optoelectronic devices has been limited because of their poor efficiency in conversion between electrical and optical energy, due to their indirect bandgap. However, recent theoretical and experimental studies have shown that 1–10 nm Si and Ge nanocrystals can exhibit efficient visible electroluminescence and photoluminescence. In particular, devices fabricated using Si and Ge nanocrystals embedded in silicon dioxide, a widely-used dielectric in Si microelectronics, have shown great promise. The purpose of Chapter 3 is to gain an understanding of the kinetics of precipitation of Ge and Si nanocrystals in silica, which might enable the synthesis of nanocrystals of chosen size and concentration. Precipitation of 1–10 nm Ge nanocrystals and 1–2 nm Si nanocrystals was achieved with ion implantation followed by annealing. It was found that Ge nanocrystal nucleation took place during implantation, without thermal annealing. This is in contrast to other methods of nanocrystal synthesis such as cosputtering of Ge and SiO_2, which requires thermal annealing to precipitate the nanocrystals. It is shown that coarsening of the Ge nanocrystals takes place above 600 °C, increasing the size but decreasing the concentration. However, the Ostwald ripening stops after 2.5 min, due to interaction of the elastic strain fields of the precipitates. In contrast to Ge nanocrystal precipitation, which is not diffusion-limited, Si nanocrystal precipitation is limited

by the low diffusivity of Si in silica. In addition, Si nanocrystals were observed only after a 1000 °C anneal.

Unlike Si and Ge, GaAs is a direct bandgap semiconductor that permits efficient conversion between electronic and photonic energy. Consequently, it is widely used in devices such as thin-film solar cells and solid-state lasers. However, single-crystal GaAs wafers are relatively expensive compared to the cost of photovoltaic cells. On the other hand, polycrystalline GaAs deposited directly on glass substrates shows reduced efficiency due to the presence of grain boundaries. Recently, it has been shown that a thin film of Ge, which is lattice-matched to GaAs, can be used to seed epitaxial growth of GaAs. Thus, a Ge thin film with large grain sizes could be used as a template to increase the grain sizes in GaAs. The purpose of Chapter 4 is to study the selective crystallization of Ge on silicon dioxide using metal-induced crystallization and dopant-enhance crystal growth rate. Grain sizes of 10–20 μm in 50-nm-thick amorphous Ge were obtained at selected locations, at temperatures less than 475 °C. The grain sizes obtained represent a two-orders-of-magnitude improvement over previous efforts. It is shown that metals that form binary compounds with Ge induce crystallization in a manner different from metals that form eutectics with Ge. The mechanisms of metal-induced crystallization are discussed. Doping of the Ge films with either B or P increases crystal growth rate, but doping with both B and P decreases crystal growth rate relative to undoped films. This is the first demonstration of dopant enhancement and dopant compensation of solid phase epitaxy rate in Ge.

Chapter 2 Size-Dependent Evolution of Si Crystals in Amorphous Si Under Ion Irradiation

2.1 Introduction

Ion irradiation can dramatically alter both nucleation and growth rate of Si crystals in amorphous Si. At high temperatures (> 500 °C), ion irradiation enhances the nucleation rate of Si crystals by 5 to 7 orders of magnitude [1, 2]. At intermediate to low temperatures (100–450 °C), it can induce crystal growth or amorphization [3, 4]. While irradiation-induced phase transformation in Si via layer-by-layer crystallization or amorphization at a pre-existing planar crystal-amorphous (c-a) interface has been extensively studied [5]–[7] and interpreted [8]–[10], irradiation-induced transformation in Si via nucleation and growth of crystals is poorly understood. In particular, the role of the interface energy and the volume free energy on the crystal nucleation and growth rate has been actively investigated [1, 2, 3, 4, 11].

In this chapter, a model for ion beam induced growth and amorphization of Si crystals in amorphous Si is developed, and compared to the present and other experimental data. The present experiment consist of amorphization of nanometer-size Si crystals at 170 °C by ion irradiation to obtain crystal size distributions at different irradiation doses. From the size distributions the amorphization rate as a function of size was calculated. The results indicate a substantial increase in amorphization rate for crystal sizes below 10 nm, which is in good agreement with the present model. The model developed in this chapter presents, for the first time, a unified rate equation for irradiation-induced evolution of Si crystals of all sizes. It is able to account for the observed size and temperature dependence of the growth or amorphization rate of

small Si crystals. Furthermore, within this model, the rate of motion of the interface between an amorphous layer and a crystalline substrate simply correspond to the evolution rate of an infinitely large crystal. In this model, which is a generalization of an existing model for planar interface motion under ion irradiation [8], the size evolution of crystals is governed by competition between an amorphization process and a crystallization process. Amorphization is due to the ballistic atomic displacements within the collision cascades of the ions, and is independent of temperature or crystal size. Crystallization is aided by the migration of a nonequilibrium population of defects created the ions. The rate of defect migration near the surface of a crystal depends on the change in the free energy of the crystal due to a thermally-activated defect jump, so is size and temperature dependent. The free energy of a crystal is assumed, as in classical nucleation theory, to be the sum of the surface free energy and the volume free energy.

The size-dependent evolution rate of small crystals under ion irradiation can, in principle, be obtained by *in-situ* observation (e.g., using transmission electron microscopy) of the size evolution of a crystal and subsequent calculation of its growth rate as a function of size. However, because of the difficulties involved in such an experiment (e.g., temperature calibration of the hotstage inside the microscope and degradation of microscope resolution due to sample heating), it has not been performed, to date. In the following experiments, size-dependent growth rate was obtained by irradiating samples with different ion doses and analyzing the change in the crystal size distribution, obtained by post-irradiation transmission electron microscopy (TEM), with a continuity equation. The continuity equation is a conservation equation that describes the drift of crystals, or grains (henceforth, the word grain will be used to denote a small crystal) in size space. The irradiations were performed at a low temperature, 170 °C, so that all of the crystals shrank. This ensured that those crystals too small to be seen by TEM would shrink and disappear. Therefore, knowledge of the population of sub-observable grains was not crucial in analyzing the size distributions obtained at different irradiation doses. Amorphization of Si crystals via ion irradiation at low temperature has already been reported

[12]; however in those experiments the size of crystals studied were relatively large ($\sim$ 100 nm), and the amorphization rate was found to be size independent. For the following experiments Si thin films with 4–50 nm grains were used.

This is the first time that a continuity equation has been used to experimentally determine the growth rate as a function of size and also to calculate the temporal evolution of the size distribution under ion irradiation. Prior to this, the comparison of model and data has been based on the determination of the critical size under ion irradiation, which can be obtained by comparison of the crystal population before and after ion irradiation, the underlying assumption being that all of the grains smaller than the critical size disappear after irradiation [3]. However, with this method continuation of irradiation after the disappearance of all sub-critical grains does not yield additional information about the size dependence of the crystal evolution rate. Furthermore, this method cannot be used to analyze experiments such as the present one, where even the largest crystals underwent amorphization; in other words, it cannot be used to analyze experiments in which the critical size approaches infinity. In contrast, by using a continuity equation comparison of model and experiment on irradiation induced crystal size evolution, at any given temperature, can be done in two dimensions—size and temporal space, using crystal size distributions obtained at different durations of irradiation, instead of in zero dimension, using the critical radius. Thus, the present method of analysis is able to test a given model against experimental data much more rigorously.

2.2 Background

2.2.1 Solid phase epitaxy

For a planar crystal-amorphous interface in Si, thermal annealing results in movement of the interface via layer-by-layer crystallization of the amorphous phase, or solid phase epitaxy (SPE). Typically the amorphous Si (a-Si) layer is created by either ion implantation or vacuum evaporation. For temperatures too low, or annealing times

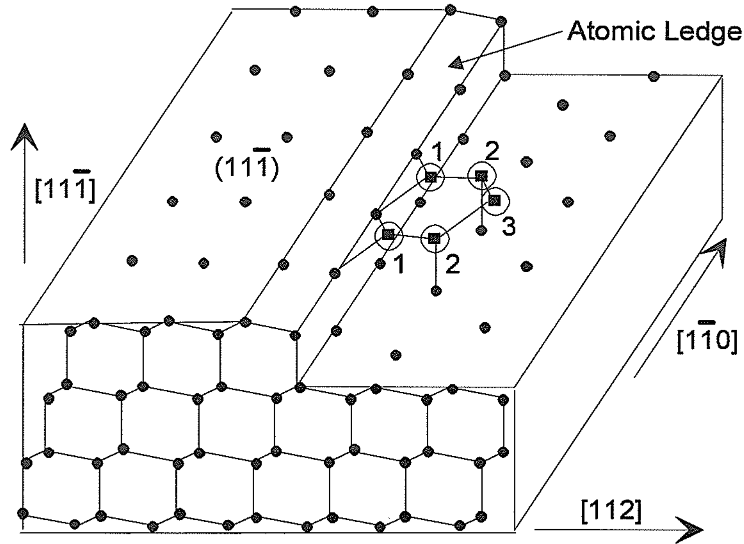

Figure 2.1: Schematic of a [1$\bar{1}$0] ledge on a (11$\bar{1}$) terrace separating the crystalline phase from the amorphous phase in Si. For simplicity the amorphous phase at the top is not shown. Atoms from the amorphous side of the interface break bonds with their neighbors and attach to the [1$\bar{1}$0] ledge. The numbers next to the atoms designate the order that the atoms are attached to the ledge. After Ref. [20].

too short, to induce homogeneous nucleation, the c-a interface remains atomically smooth during SPE [13, 14]. The rate of solid phase epitaxy in Si, which varies by over 10 orders of magnitude from about 500 °C to about 1300 °C, is characterized by a single activation energy—2.7 eV [15], and is strongly affected by the crystal orientation at the interface [16].

It has been proposed that a crystal-amorphous interface in Si is composed of (111) terraces bounded by [$\bar{1}$10] ledges [16, 17, 18], as illustrated in Fig. 2.1. Among the crystallographic planes that can divide the crystalline from the amorphous phase, the (111) planes have the minimum interfacial energy because each Si atom on the crystal side of the interface need only one—instead of two or three—bond to Si atoms on the amorphous side to maintain its tetrahedral coordination; thus, the number of unsatisfied bonds and the bond angle distortions near the interface can be kept to a minimum. The majority of the interfacial energy is attributed to bond angle distortion instead of bond length variation because the latter has a much higher force constant. In this model, solid phase epitaxy proceeds by advancement of the [$\bar{1}$10]

ledges, through bond breaking and rearrangement at the interface. It has been used to explain the effects of doping [19], interface orientation [16, 13], and twinning [20] on SPE rate. For example, it can be shown, by a simple geometric argument, that the density of $[\bar{1}10]$ ledges is proportional to $\sin\theta$, where θ is the angle between the surface normal of the c-a interface and the [111] direction. Accordingly, the SPE rate should be proportional to $\sin(\theta)$, which is in reasonable agreement with experimental data [16].

The SPE rate in the [100] and [110] directions are faster than that in the [111] directions by a factor of 25 and 3, respectively. Although the SPE rate is slowest for the (111) planes, it has been shown that formation of internal microtwins can increase the SPE rate of these planes [20]. Since the shape of a crystal growing in an amorphous matrix is expected to be bounded by the slowest moving planes, randomly nucleated crystals in amorphous Si usually exhibit (111) faceted structures, contain many internal twin boundaries, and have highly anisotropic shapes [21]. In addition, the growth velocity of these grains is comparable to that of the (111) SPE velocity [22].

Solid phase epitaxy is controlled by one thermally activated process, as evidenced by the fact that a single activation energy is obtained throughout the entire temperature range where SPE rate is measurable [15]. The fact that SPE rate depends on crystal orientation eliminates bulk diffusion of defects (such as vacancies and interstitials) to the interface as the rate-limiting step. In fact, recent experiments on the effects of hydrostatic [23] and uniaxial [24] stress on SPE rate support the notion that bond breaking and rearrangement at the interface are the operative mechanisms of SPE. The activation energy, as interpreted by a kinetic model [23], is believed to be the sum of the energy required to break a bond and the energy required to migrate a dangling bond.

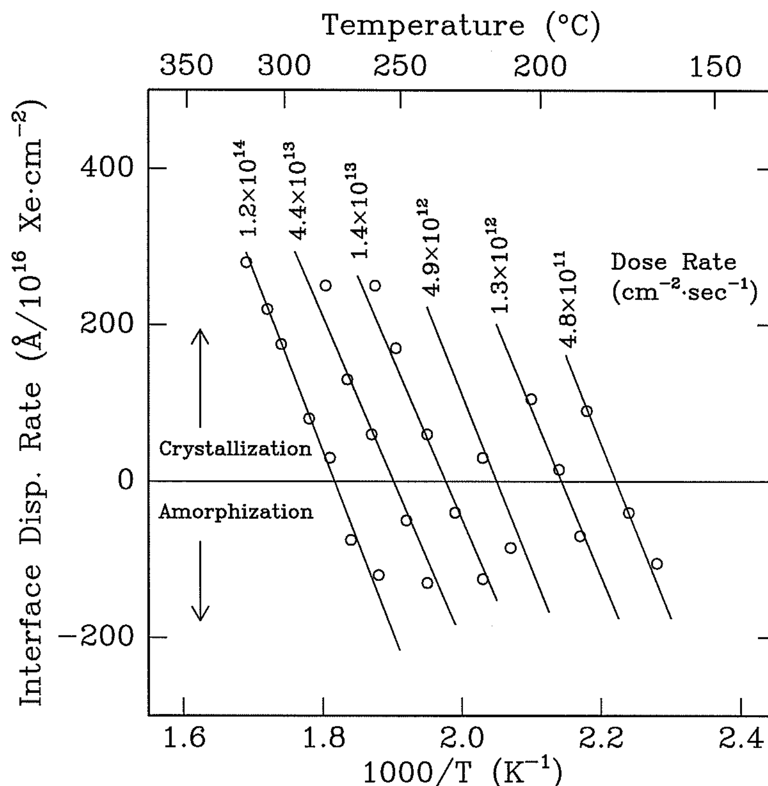

Figure 2.2: Interface displacement rate for various temperatures and ion fluxes for 1.5 MeV xenon ions. The interface displacement has been normalized to a dose of 10^{16} ions/cm^2. The data is from Ref. [25], and the lines were calculated using Jackson's [8] model (Eq. 2.36), which is discussed in Sec. 2.4.1.

2.2.2 Ion beam induced solid phase epitaxy

Under ion irradiation, the temperature and crystal orientation dependence of the SPE rate is much weaker (activation energy of $\sim$ 0.2–0.3 eV [6]) than in thermal-induced crystallization (activation energy of 2.7 eV [15]). At temperatures lower than 500 °C, where thermal SPE is negligible, ion irradiation significantly enhances the rate of the c-a interface movement. Furthermore, for a given ion flux, there is a transition temperature above which crystallization occurs, and below which amorphization occurs [5, 6, 7]. For a given temperature, high dose rates, and/or heavy ions, results in layer-by-layer amorphization while low dose rates, and/or light ions, results in epitaxial crystallization [6]. An example of the interface displacement rate at various temperatures and ion fluxes for 1.5 MeV Xe ions is shown in Fig. 2.2. For the cases

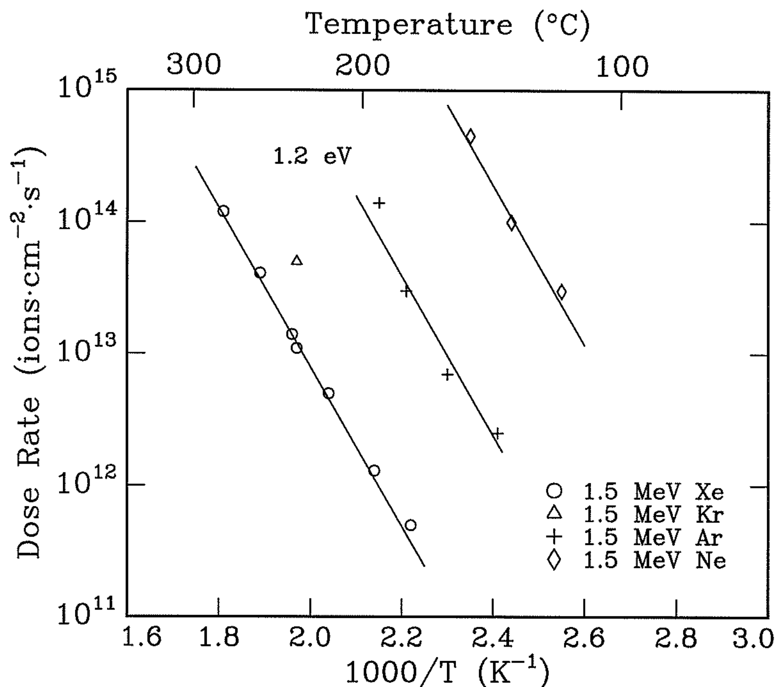

Figure 2.3: Dose rate dependence of the temperature for zero growth rate for 1.5 MeV Xe^+, Kr^+, Ar^+, and Ne^+ bombardments of Si. The data are from Ref. [25], and the lines were calculated using Jackson's [8] model (Eq. 2.39).

where irradiation results in no interface movement, the relationship between the ion flux and the transition temperature exhibits an Arrhenius form, with an activation energy of 1.2 eV [5] (see Fig. 2.3). The rate of interface movement scales with the nuclear energy loss of the ions, or the number of atoms displaced from their lattice sites (calculated by the TRIM Monte Carlo program [26]) by the ions [27]. The fact that amorphization occurs at high ion fluxes suggests that beam induced heating of samples is not responsible for ion beam induced crystallization.

The weak temperature dependence of the SPE rate under ion irradiation is due to the fact that defects responsible for SPE are generated athermally by the ion beam, so that the energy barrier for defect formation is essentially zero [8]. In contrast, in thermal SPE defects are generated by temperature fluctuation. The 1.2 eV activation energy described above is thought to be the energy barrier for defect migration under ion irradiation. If the same type of defect is responsible for both thermal and ion

induced SPE, then the formation energy of a pair (defects generate and annihilate in pairs) of defects via thermal activation is $2.7 - 1.2 = 1.5$ eV.

The disparity in SPE rate between different crystal orientations is smaller under ion irradiation than under pure thermal annealing. The crystallization rates of (100) and (110) planes under ion irradiation are almost identical, and about 4 times faster than that of (111) planes [27, 10]. Furthermore, after the formation of internal twin boundaries the SPE rate of (111) planes increases to about 70% of that of (100) planes [10]. It has been postulated that the smaller difference between the SPE rate of different crystal orientations under ion irradiation is due to the roughening of the $[\bar{1}10]$ ledges—the ledges where atoms in the amorphous phase are converted to the crystalline phase—by the ion beam, which increases the SPE rate near the [111] orientations by providing more ledge sites on the (111) terraces [10]. In thermal SPE the $[\bar{1}10]$ ledges are thought to be fairly straight because of the large thermal energy required for ledge roughening due to increased bond angle distortions near a ledge. At temperatures low enough that beam induced amorphization occurs, the interface velocity becomes orientation independent [27]. This is hardly surprising, since in this regime, amorphization is mainly governed by the displacement energy of Si atoms from their lattice sites, which is independent of interface structure. As a consequence of the weak orientation dependence of the interface velocity under ion irradiation, the shapes of Si crystals in irradiation induced grain growth or amorphization are much more isotropic than in pure thermal induced grain growth [32]. As in the case of thermal SPE, under ion irradiation the growth rate of large grains is equal to the velocity of the (111) planes [37].

For ion beam induced grain growth in a-Si, the interpretation that growth rate is size-dependent, and that a critical size exists, has been based the observation that the crystal population decreases with decreasing temperature [3]. In the next section it will be shown that the size dependence of the growth rate can be demonstrated even when all grains undergo amorphization—when a critical size cannot be obtained from population counting. It will be shown that crystals smaller than 10 nm shrink much faster than larger crystals.

2.3 Experiment

Amorphous Si of 100 nm thickness were deposited at < 100 °C by electron beam evaporation under ultrahigh vacuum (UHV) (base pressure of 5×10^{-10} Torr, typical pressure of 4–8 $\times 10^{-9}$ Torr during deposition) onto oxidized (100) Si wafers with 100 nm of SiO_2. Prior to deposition, the samples were cleaned by immersion in an oxidizing RCA solution (5:1:1 H_2O:H_2O_2:NH_4OH) for 20 min at 80 °C. They were then heated to 550 °C in UHV for 1 hr to desorb water molecules and other physisorbed gases. After deposition the samples were baked at 200 °C in UHV for 1 hr to densify the a-Si films. This prevents the formation of microvoids which could trap water vapor and other impurities when the films are exposed to air [28].

To ensure that the Si films were truly amorphous, the samples were irradiated with 100 keV $^{29}Si^+$ ions at 77 K, to a dose of 5×10^{15} ions/cm^2 [30]. During irradiation the beam current was kept below 1 μA/cm^2 to avoid beam heating of the samples. Si atoms with atomic mass of 29 were used instead of the more common ^{28}Si atoms to reduce the possibility of contamination from N_2 and CO molecules, both of which have atomic mass of 28. All of the ion irradiations described in this experiment were performed in high-vacuum, at about 2 $\times 10^{-7}$ torr.

To produce nanometer-size crystals, the samples were subsequently irradiated at 580 °C using 250 keV Ar^+ ions, with a flux of 1×10^{12} ions/cm^2 s, to a dose of 1.7×10^{15} ions/cm^2. This transformed the a-Si films into polycrystalline films with 4–50 nm crystals. The average crystal size was 16 nm. Ion irradiation induced nucleation was used to create the small crystals instead of chemical vapor deposition (CVD) of amorphous Si (which are known [32] to contain nanometer-scale crystals) for better reproducibility. For this irradiation step, the samples were glued to a stainless steel hotstage with silver paint to ensure good thermal contact. Sample temperature was measured using a thermocouple clipped onto the hotstage. The temperature measured with this thermocouple were calibrated by comparing it against the temperature of a thermocouple pressed onto the surface of a sample during one trial run, without the ion beam. This temperature calibration was done for 45–740 °C. In order to

ensure the temperature and thus the grain size uniformity across the samples, the sizes of the samples were kept to 1 cm^2 or less. During all the irradiation procedures the fluctuation in beam current, or flux, was kept below 15%, and the fluctuation in sample temperature below 3 °C. The accuracy of the current integrator was checked by implanting 1×10^{16} ions/cm^2 of 250 KeV Xe^+ ions into an a-Si film and counting the density of Xe atoms using Rutherford backscattering spectrometry (RBS).

To amorphize the nanometer crystals, the samples were irradiated at 170 °C with 250 keV Ar^+ ions, with a flux of 1×10^{12} ions/cm^2 s, at three different doses: 2, 3, or 4×10^{15} ions/cm^2. In order to ensure that the results of the above amorphization doses can be compared to each other, care was taken to make certain that the samples contained the same microstructures before irradiation. Therefore, a 1 cm $\times$ 1 cm sample rendered polycrystalline by the 580 °C irradiation procedure was cut into four 0.5 cm $\times$ 0.5 cm pieces; one was used to determine the initial microstructure by TEM, and the remaining three were used for the above amorphization step. The amorphization was done using a hotstage with four rotatable positions, each with its own copper heating block and thermocouple, which permitted irradiation of multiple samples without breaking vacuum. The sample temperature was directly measured with the thermocouples embedded in the copper blocks, since sample and hotstage temperature were found to be virtually identical for temperatures below 300 °C. The samples were glued to the hotstage with silicone heat-conducting paste to ensure good thermal, as well as electrical (to prevent charging of the sample), contact. The projected range (using the TRIM Monte-Carlo program [26]) of the 250 keV Ar ions is 100 nm into the Si substrate, leaving practically no Ar inside the 100 nm Si film.

Figure 2.4 and 2.5 show the bright field and dark field transmission electron micrographs, respectively, of samples irradiated with the three ion doses. It is evident that the Ar^+ irradiations at 170 °C reduced the number of crystals dramatically. In addition, as Fig. 2.5 (d) shows, crystals smaller than 10 nm had all but disappeared after an ion dose of 4×10^{15} ions/cm^2. Furthermore, the shapes of these crystals are quite isotropic, which is consistent with reports of irradiation-induced growth of crystals in CVD grown a-Si [32]. High-resolution transmission electron micrographs,

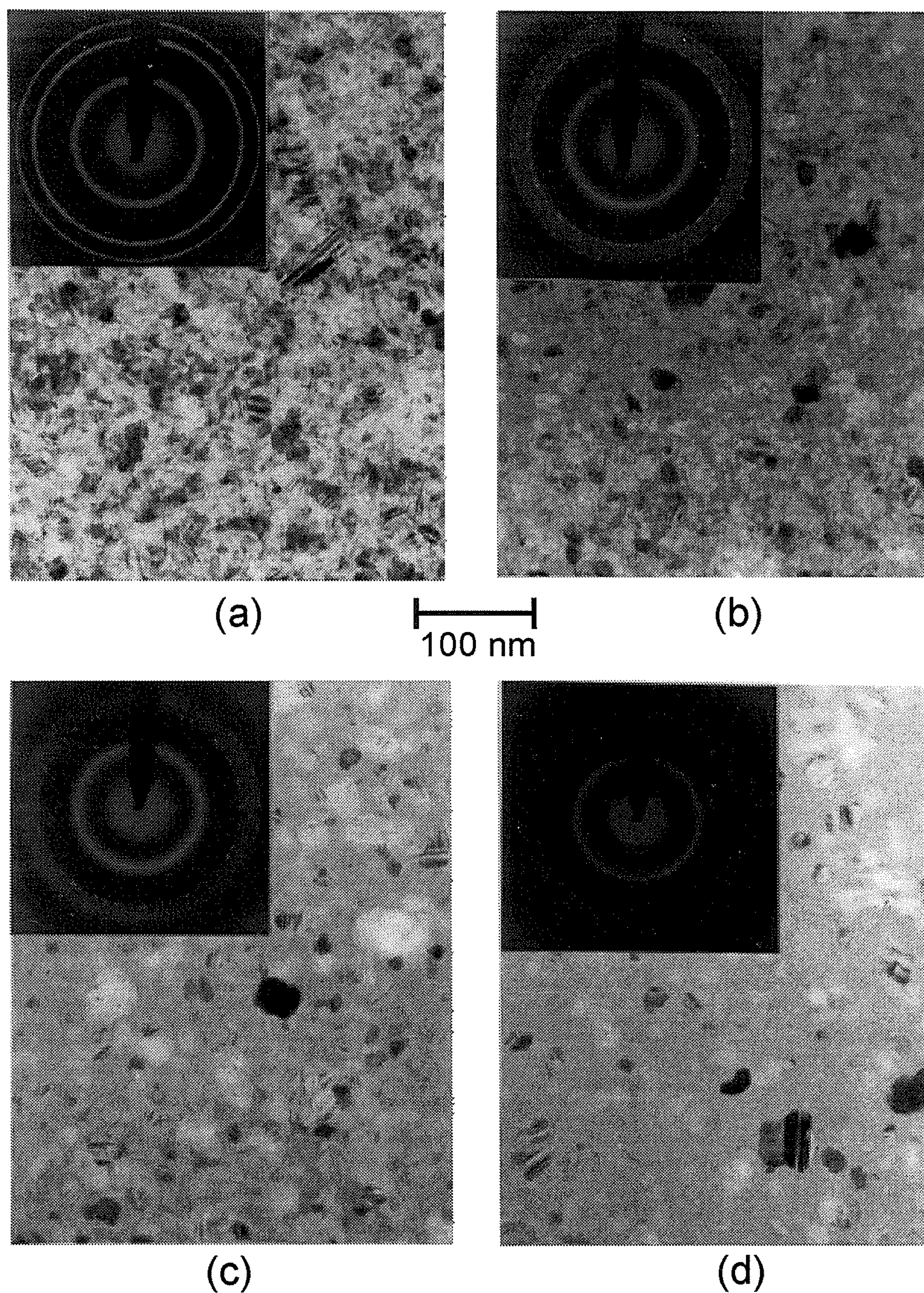

Figure 2.4: Bright field transmission electron micrographs of polycrystalline Si samples (100 nm Si on 100 nm SiO_2 on (100) Si) irradiated with various Ar^+ ion doses: (a) unirradiated, (b) 2×10^{15} ions/cm^2, (c) 3×10^{15} ions/cm^2 and (d) 4×10^{15} ions/cm^2. Sample temperature was 170 °C, the ion flux was 1×10^{12} ions/cm^2 s, and the ion energy was 250 keV. The projected range of the ions is 100 nm into the (100) Si substrate.

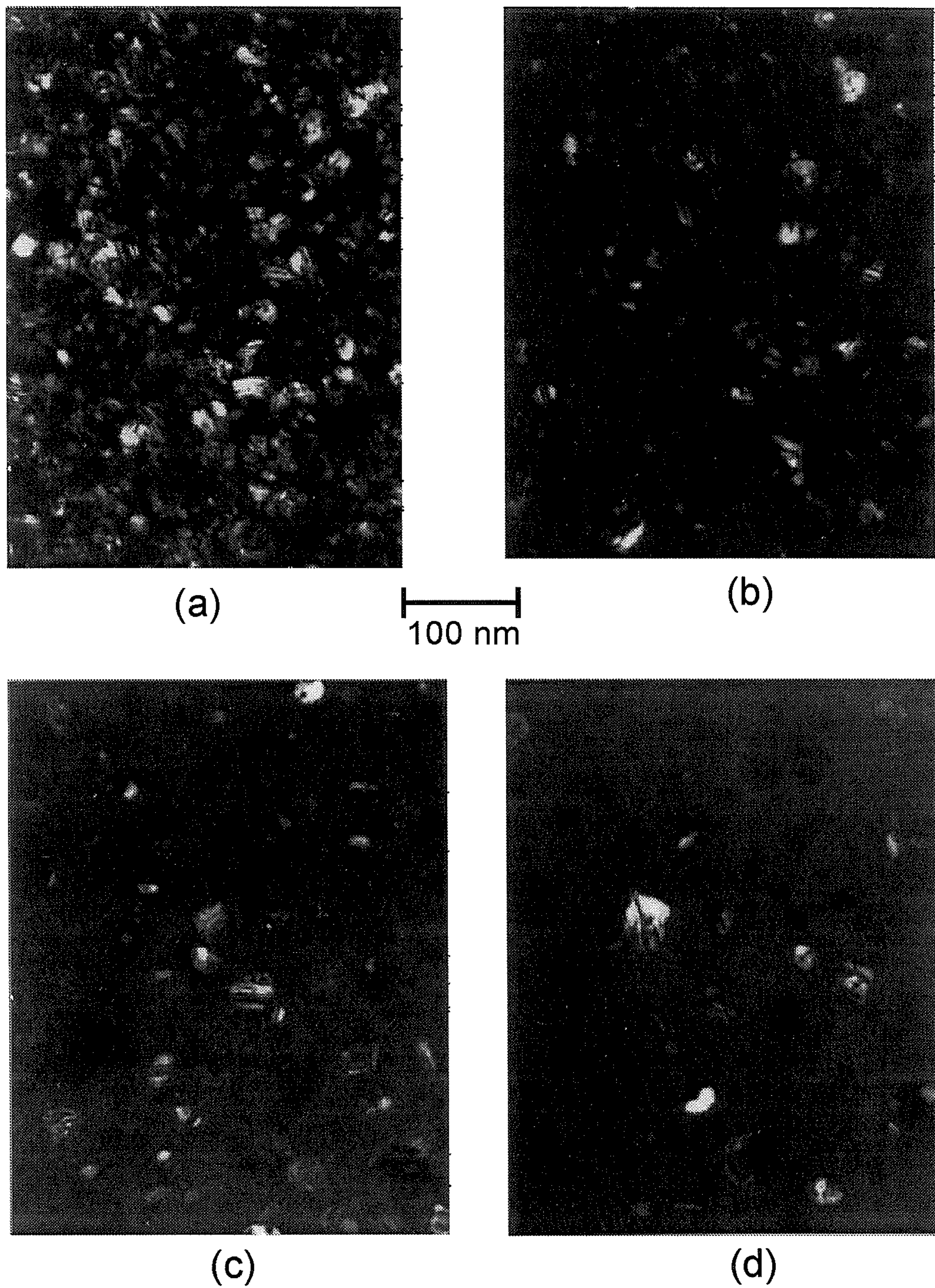

Figure 2.5: The corresponding dark field transmission electron micrographs of samples shown in Fig. 2.4: (a) unirradiated, (b) 2×10^{15} ions/cm^2, (c) 3×10^{15} ions/cm^2 and (d) 4×10^{15} ions/cm^2.

two examples of which are shown in Fig. 2.6, indicate that even after the largest ion dose, the crystals still retained well-defined, sharp c-a interfaces. This suggests that the amorphization of these crystals occurred in an interface-mediated, layer-by-layer fashion, as in the case of large crystals [12].

The evolution of the crystal size distribution with ion dose is shown in Fig. 2.7. Each distribution was obtained from approximately 350 grains, using dark field transmission electron micrographs taken at 122,000 times magnification. The reasons for using dark field micrographs instead of bright field images were: (a) higher contrast between the crystals and the matrix, and (b) fewer crystals in the images, which made it easier to identify individual crystals. At this magnification, for Si films of 100 nm thickness, the smallest size of crystals that could be clearly resolved was 4 nm. Therefore, the first bin of each of the histograms, toward which grains from 0 to 6 nm diameter were counted, is only a lower limit. It is apparent from Fig. 2.7 that crystals of all sizes decreased in number, suggesting that all of them underwent amorphization. In addition, the peak of the distribution shifted from about 9 nm to about 15 nm with increasing ion dose. The variation of grain density and average grain size with ion dose are shown in Fig. 2.8. While the grain density decreased with ion dose, the average grain size actually increased, reflecting the shift of the distribution peak.

Under ion irradiation, the amorphization rate of an infinitely large crystal should be the same as that of a (111) planar c-a interface. Since ion-assisted solid phase epitaxy is faster for the (100) planes than the (111) planes [10, 27], the velocity of a (100) c-a interface under identical irradiation conditions should serve as an upper limit on the growth rates of Si crystals in a-Si. Thus, ion irradiation of a Si film containing a (100) c-a interface was performed. The interface was constructed by depositing 100 nm of a-Si on an undoped (100) Si wafer, using the same deposition procedure described above. The thickness of the a-Si film was kept the same as those deposited on SiO_2, because it has been observed that SPE rate under ion irradiation increases with the depth of the c-a interface [27]. This sample was subjected to the same 170 °C Ar^+ irradiation step described above. The irradiation dose used was 4×10^{15}

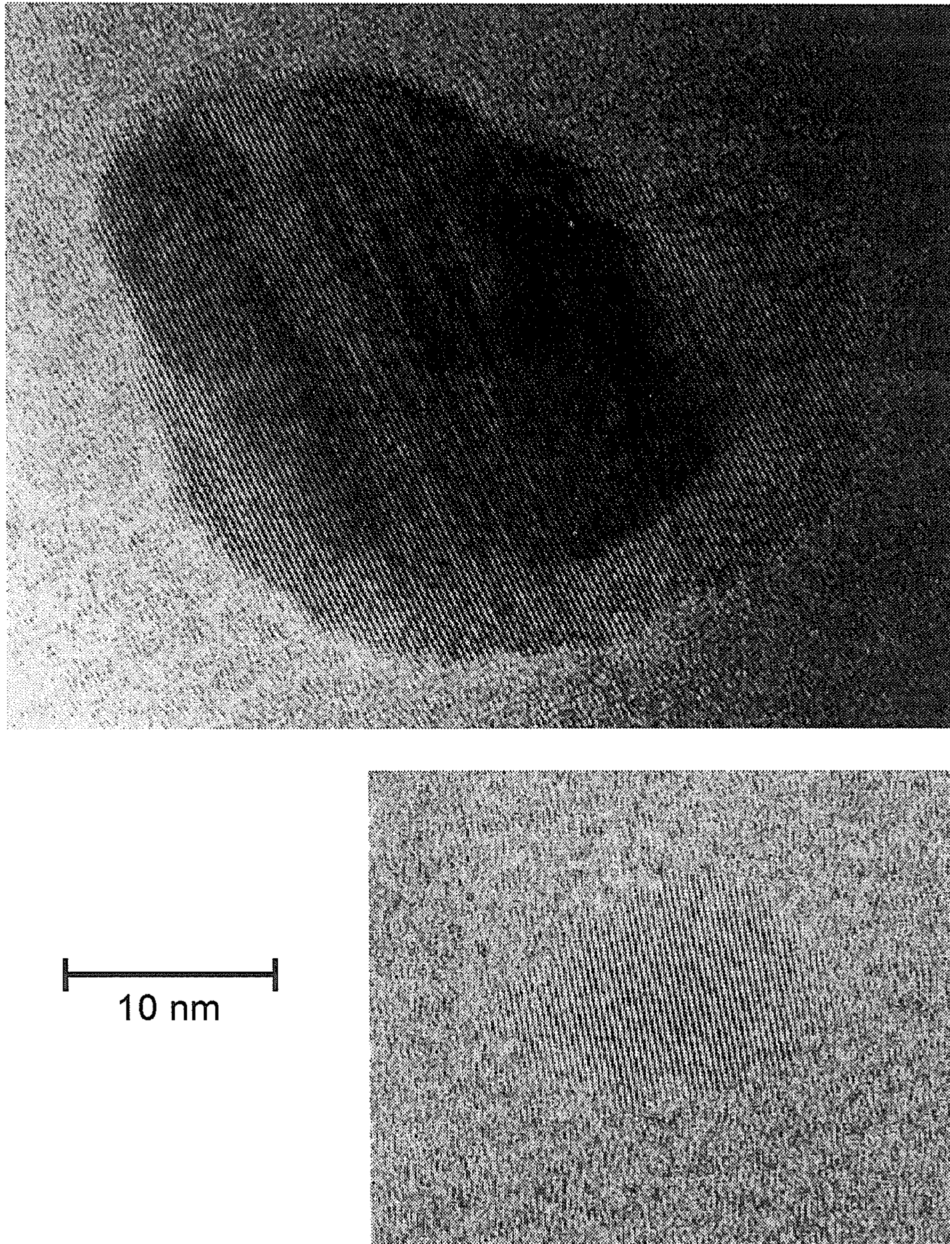

Figure 2.6: High-resolution transmission electron micrographs of Si crystals in a film irradiated with 4×10^{15} ions/cm^2. The lattice fringes of the crystals can be seen clearly, indicating that the interfaces between the crystals and the amorphous matrix are well-defined, even for this ion dose. Thus, shrinkage of the Si crystals by the Ar^+ irradiation probably occurred in a layer-by-layer fashion.

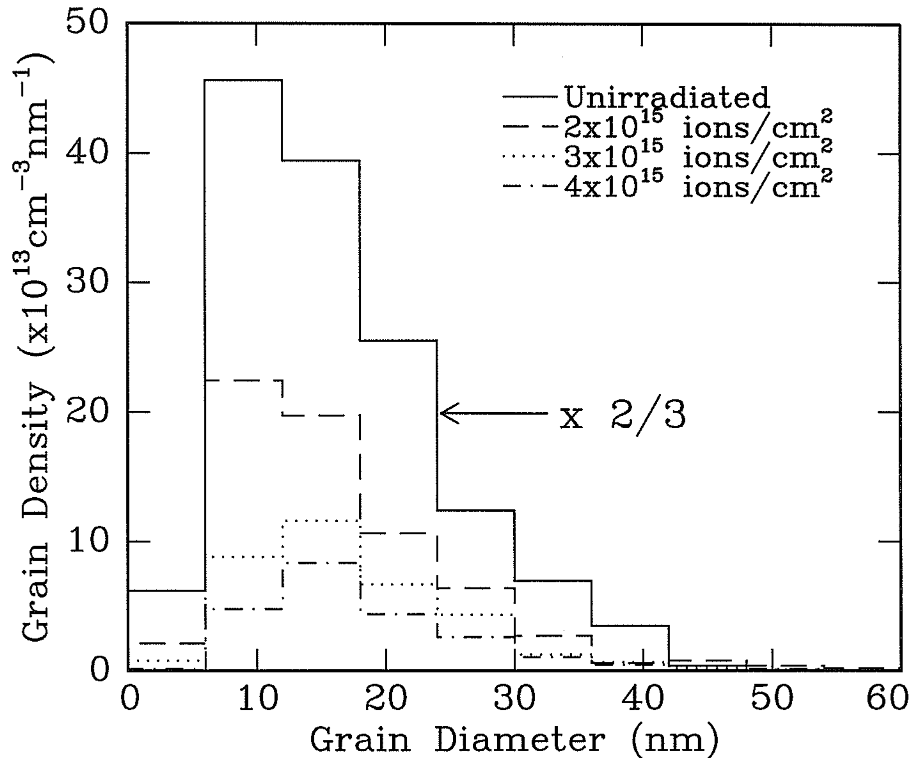

Figure 2.7: A plot of the evolution of the crystal size distribution under ion irradiation. The peak of the distribution increased from about 9 nm to about 15 nm with ion dose, even though crystals of all sizes decreased in number, suggesting that crystals smaller than 10 nm shrank faster than larger crystals.

ions/cm^2. The thickness of the amorphous layer before and after ion irradiation was measured by using the channeling mode of RBS, the result of which is shown in Fig. 2.9. Instead of amorphization, the ion irradiation induced crystallization at the interface, which is consistent with the reports of faster ion-assisted growth rate of (100) planes compared to (111) planes [10, 27]. The crystallization distance was 5.0 ± 1.0 nm, which corresponds to an interface velocity of $1.25 \pm .25 \times 10^{-3}$ nm/s.

2.3.1 Calculation of growth rate

If the growth rate of a crystal under ion irradiation depends only on the size of the crystal, then the evolution of the crystal size distribution can be described by a

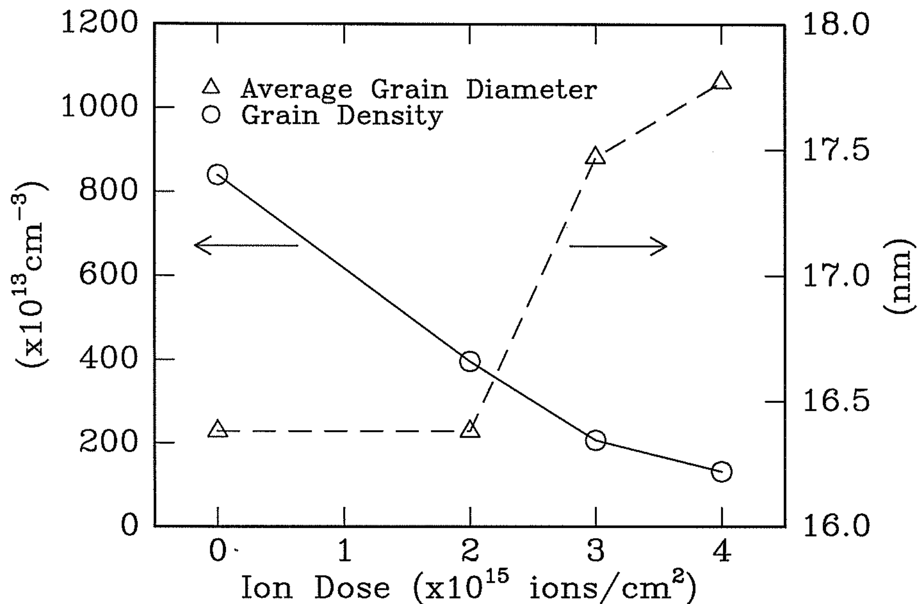

Figure 2.8: A plot of the variation of crystal density and average size with ion dose. While crystal density decreased with ion dose, the average size actually increased.

continuity equation of the form:

$$\frac{\partial f(r,t)}{\partial t} = -\frac{\partial}{\partial r}\left[f(r,t)\cdot\dot{r}(r)\right] + S_1(r,t) - f(r,t)S_2(r,t), \tag{2.1}$$

where $f(r,t)$ is the number of crystals of radius r at time t, and $\dot{r}(r)$ is the growth rate of a crystal of radius r. The first term on the LHS of the equation is the flux divergence term, and S_1 and fS_2 are the source and the sink term, respectively. The continuity equation is a conservation equation: it conserves the number of particles in size-space. For sample temperatures below 500 °C, ion irradiation induced nucleation in Si is negligible, so the source term S_1 can be taken to be zero. In addition, the size distributions obtained from transmission electron micrographs suggest that there were no complete amorphization of crystals by a single ion, i.e., no sinks in size-space, so S_2 is also equal to zero. Thus the continuity equation reduces to

$$\frac{\partial f(r,t)}{\partial t} = -\frac{\partial}{\partial r}\left[f(r,t)\cdot\dot{r}(r)\right]. \tag{2.2}$$

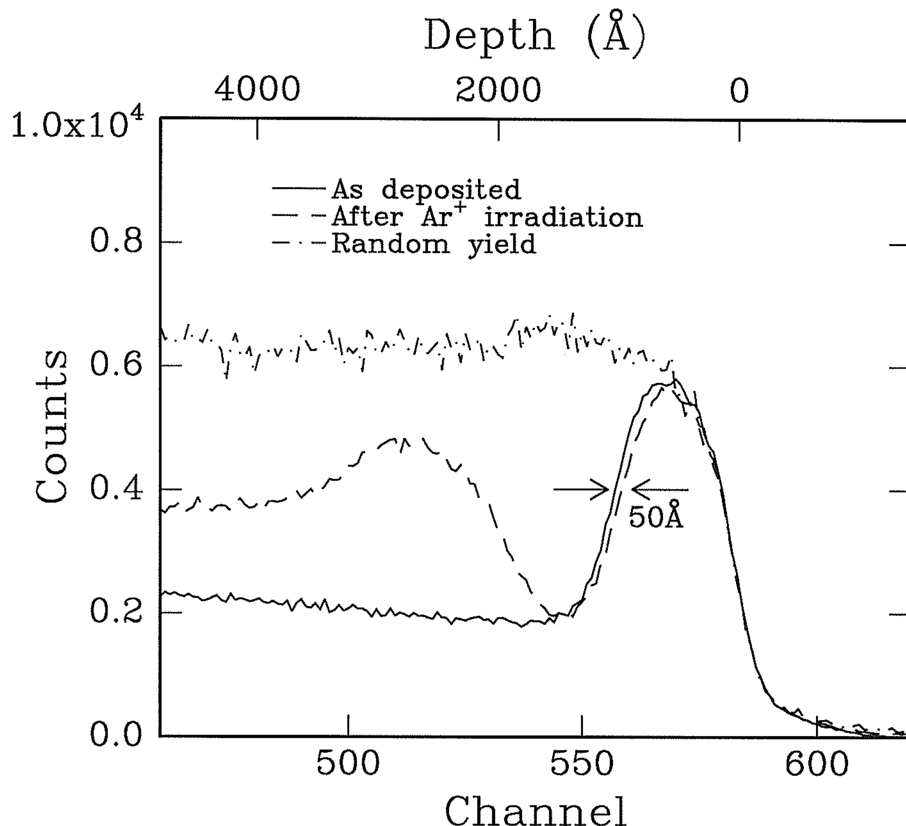

Figure 2.9: Random and (100)-aligned backscattering spectra of 2 MeV $^4He^{++}$ ions incident on a sample with 100 nm of amorphous Si on an (100) Si wafer, before and after the sample was subjected to Ar^+ ion irradiation. The Ar^+ irradiation conditions were the same as those in Fig. 2.6. The crystal-amorphous interface moved 5.0 nm toward the amorphous phase after the Ar^+ ion irradiation. For an ion flux of 1×10^{12} ions/cm^2 s and an ion dose of 4×10^{15} ions/cm^2, this crystallization distance corresponds to an interface velocity of $1.25 \pm .25 \times 10^{-3}$ nm/s.

It will be shown in Sec. 2.5.1 that the assumptions that $S_1 = 0$ and $S_2 = 0$ are valid. For size-independent growth rate, $\dot{r}$ is a constant, and the continuity equation reduces to:

$$\frac{\partial^2 f}{\partial t^2} = \dot{r}^2 \frac{\partial^2 f}{\partial r^2}, \tag{2.3}$$

a classical wave equation. Therefore, for constant growth rate the size distribution is a nondispersive wave traveling in size space—it shifts position without changing its shape. For the present experiment, Fig. 2.7 clearly shows that the size distribution not only shifted toward smaller sizes but also changed the position of the peak. Therefore,

i	r_i	f_i^0	f_i^2	f_i^3	f_i^4
0	1.5	18.56	4.253	1.547	0.2624
1	4.5	136.9	44.85	17.60	9.577
2	7.5	118.3	39.44	23.21	16.66
3	10.5	76.56	21.27	13.35	8.790
4	13.5	37.12	12.76	8.704	5.248
5	16.5	20.88	5.413	2.514	2.099
6	19.5	10.44	1.160	1.354	0.9184
7	22.5	1.160	1.547	0.3868	0.1312
8	25.5	0	0.7733	0.1934	0.2624
9	28.5	0	0.3867	0	0
10	31.5	0	0	0	0

Table 2.1: Table of the crystal size distributions shown in Fig. 2.7: i is the histogram bin number, r_i is the crystal radius at the center of bin i, and $f_i^j = f(r_i, t_j)$. Data for f_i^1 are not shown because ion irradiation with a dose of 1×10^{15} ions/cm^2 was not performed.

the growth rate was size-dependent. In order to calculate the growth rate as a function of r, a finite difference form of Eq. (2.2) is used. Start by writing $f(r,t)$ as a function whose value is known only at a fixed time and size interval:

$$f(r,t) = f(r_i, t_j) = f_i^j, \tag{2.4}$$

$$r_i = i\Delta r + r_0, \qquad i = 0 \cdots I, \tag{2.5}$$

$$t_j = j\Delta t + t_0, \qquad j = 0 \cdots J. \tag{2.6}$$

For this experiment the values are: $r_0 = 1.5$ nm, $\Delta r = 3$ nm, $t_0 = 0$ s, $\Delta t = 1000$ s, $I = 10$ and $J = 4$. The values of f_i^j, taken from the histograms shown in Fig. 2.7, are listed in Table 2.1. Note that since the histograms were generated using grain diameter rather than radius, the relation $f(r) = 2f(d)$, where d is grain diameter, was used in producing Table 2.1.

The finite difference form of Eq. 2.2 is

$$\left.\frac{\partial f}{\partial t}\right|_i^j = \frac{-(f\dot{r})_{i+1}^j + (f\dot{r})_i^j}{\Delta r} \tag{2.7}$$

$$\frac{f_i^{j+1} - f_i^j}{\Delta t} = \frac{-f_{i+1}^j \dot{r}_{i+1} + f_i^j \dot{r}_i}{\Delta r}. \tag{2.8}$$

So the growth rate as a function of size, or i, is

$$\dot{r}_i = \frac{1}{f_i^j}\left[\frac{\Delta r}{\Delta t}\left(f_i^{j+1} - f_i^j\right) + f_{i+1}^j \dot{r}_{i+1}\right]. \tag{2.9}$$

This is a recursive equation, since the value of $\dot{r}_i$ depends on the value of $\dot{r}_{i+1}$. To solve this equation, choose a large value of i such that $f_{i+1}^j = 0$. This can always be done since $f(r) \to 0$ as $r \to \infty$. For example, Table 2.1 shows that $f_8^0 = 0$; therefore, chose $i = 7$. Then $\dot{r}_i$ becomes

$$\dot{r}_i = \frac{1}{f_i^j}\left[\frac{\Delta r}{\Delta t}\left(f_i^{j+1} - f_i^j\right)\right], \tag{2.10}$$

a closed form solution. Then, Eq. 2.9 can be used iteratively to calculate all other values of $\dot{r}_i$.

The calculated growth rates are shown in Fig. 2.10. Two sets of growth rates were obtained: $\dot{r}_i^{(2-3)}$, calculated from the distributions f_i^2 and f_i^3, and $\dot{r}_i^{(3-4)}$, calculated from the distributions f_i^3 and f_i^4. The data shown in Fig. 2.10 are the averages of the two sets of growth rates. The initial size distribution, f_i^0, was not used in the computation because the time spacing between f_i^0 and f_i^2 was too large and would have made the results inaccurate. As shown in the figure, the growth rate changes considerably with size around $r = 5$ nm. Note that since grains with diameter less than 4 nm could not be observed in the present experiment, f_0^j underrepresent the number of crystals with diameter less than 6 nm; consequently, the value of $\dot{r}_0$ in Fig. 2.10 is not very accurate.

Another method of calculating size-dependent growth rate from the temporal evolution of the grain size distribution, called growth path envelope analysis (GPEA), was shown by Jayanth and Nash [33]. It was used to obtain the coarsening rate of γ' precipitates in Ni-Al and Ni-Al-Cr alloys. This method is essentially equivalent to solving the continuity equation using graphical constructions. Compared to GPEA, the method presented above is much easier to apply.

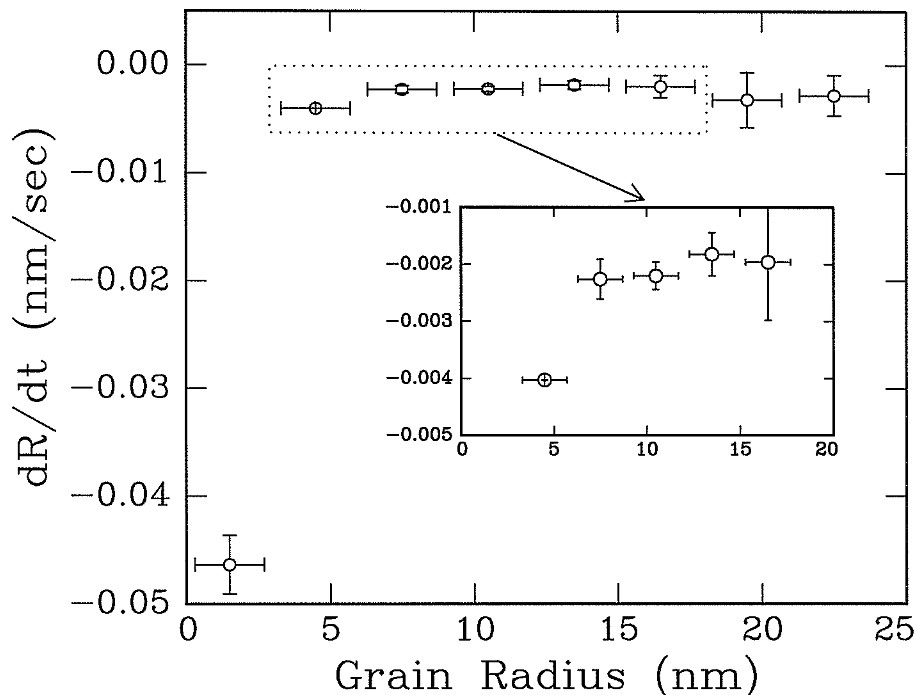

Figure 2.10: Calculated growth velocity as a function of size. A continuity equation was used to compute the growth velocity using the size distribution data in Table 2.1. Inset shows an expanded view of growth rates of 4–18 nm grain radius. It is evident that there is a dramatic increase in the amorphization rate for grain radius less than 5 nm.

2.3.2 Uncertainties in computing growth rate

The x and y error bars in Fig. 2.10 reflect the uncertainties in particle size measurement and histogram generation. The magnitudes of the y error bars, σ_y^i, are equal to one-half times the differences in the two set of growth rates:

$$\sigma_y^i = \frac{1}{2}\left|\dot{r}_i^{(2-3)} - \dot{r}_i^{(3-4)}\right|. \tag{2.11}$$

Note that the sizes of σ_y^i are smaller around r = 5–15 nm. This is due to the fact that the histograms have much higher counts for those particle sizes—the statistics are much better for those bins. Where the crystal size distributions tail off, at both size extremes, the particle statistics are relatively poor, resulting in large σ_y^i.

The uncertainty in radius, or the size of the x error bars, is a constant which

depends on both the bin size of the histograms and the uncertainty in particle size measurement. Since these two sources are independent, the uncertainty in x, σ_x, is given by

$$\sigma_x = \sqrt{\sigma_1^2 + \sigma_2^2}, \tag{2.12}$$

where σ_1 depends on the histogram bin size and σ_2 is associated with the size measurement. Due to the inherent difficulty of TEM imaging of very small particles, there is an uncertainty of ± 1 nm in their size (diameter) determination, so σ_2 is 0.5 nm. The magnitude of σ_1 is proportional to the histogram bin size, Δr. In generating the histograms, particles with radius between $r_i + \Delta r/2$ and $r_i - \Delta r/2$ were counted as having radius r_i. In other words,

$$f_i^j = f(r_i, t_j) = \frac{1}{\Delta r} \int_{r_i - \Delta r/2}^{r_i + \Delta r/2} f(r, t_j) dr. \tag{2.13}$$

Thus the upper limit of σ_1 is $\Delta r/2$. Here σ_1 is chosen to be $\Delta r/3$, or 1.0 nm. Therefore, σ_x equals 1.2 nm.

In order to use Eq. 2.9 to compute $\dot{r}_i$, the histogram bin size must be chosen carefully. Strictly speaking, the usage of the finite difference representation of the continuity equation is valid only when the time spacing Δt is small enough that $\partial f/\partial t$ does not change appreciably from one time step to the next. Conversely, if the time spacing is fixed, then the bin size must be large enough so that most grains in a given bin do not migrate out of that bin; otherwise f_i^j, and hence $\partial f/\partial t$, will change significantly after one time step. In short, for a fixed Δt, the bin size, Δd, must be chosen so that

$$\Delta d > \left|\dot{d} \Delta t\right|, \tag{2.14}$$

where $\dot{d} = 2\dot{r}$. Since the growth rate, $\dot{r}$, is a function of size, the above equation becomes

$$\Delta d > \left|2\dot{r}_j \Delta t\right|. \tag{2.15}$$

However, a compromise was needed when the bin size was chosen. Having a larger bin size would improve the accuracy of $\dot{r}_i$, and would reduce σ_y^i, since each bin would

have a larger number of counts; on the other hand, the number of data points for $\dot{r}_i$ would decrease, and σ_x would increase. The chosen bin size was 6 nm, which satisfies Eq. 2.15 for all data points in Fig. 2.10, except the two on the left. When the growth rates were calculated using histograms with a 5 nm bin size, σ_y^i became very large, mainly because the growth rates for large particle sizes became very inaccurate, and those were in turn used to compute the growth rates for small sizes.

The restriction in choosing the bin size can be relaxed if the growth rates were obtained implicitly, by integrating the continuity equation with a very small time step. For example, starting from the initial size distribution f_i^j, a M-step integration can used to calculate $f_i^{j+1/M}$, $f_i^{j+2/M}$,..., f_i^{j+1}, using Eq. 2.7 and the following equations:

$$f_i^{j+1/M} = f_i^j + \frac{\Delta t}{M} \left.\frac{\partial f}{\partial t}\right|_i^j \tag{2.16}$$

$$f_i^{j+2/M} = f_i^{j+1/M} + \frac{\Delta t}{M} \left.\frac{\partial f}{\partial t}\right|_i^{j+1/M} \tag{2.17}$$

$$\vdots$$

$$f_i^{j+1} = f_i^{j+(M-1)/M} + \frac{\Delta t}{M} \left.\frac{\partial f}{\partial t}\right|_i^{j+(M-1)/M} . \tag{2.18}$$

Alternatively, a method like the Runge-Kutta [34] can be used to perform each of the integration step above. The values of $\dot{r}_i$ shown in Fig. 2.10, which were obtained from Eq. 2.9, can be used as initial values, and constantly refined until the M-step integration produces f_i^{j+1} which agree with experimentally determined values. In fact, since both f_i^j and f_i^{j+1} size distributions are known from experiment, this becomes a two point boundary value problem, in which multiple roots must be determined simultaneously—a multidimensional root-finding problem. In this case, Eq. 2.15 becomes

$$\Delta d > \left|\frac{2\dot{r}_j \Delta t}{M}\right|, \tag{2.19}$$

which can be satisfied for any bin size Δd, provided that one chooses an appropriate value of M.

Because of its numerical computation complexity, calculation of growth rates via

M-step integration has not been performed. Instead, a model for grain growth and amorphization under ion irradiation is developed and fitted to the amorphization rates obtained in Fig. 2.10. It will be shown that these amorphization rates are already very accurate.

2.4 Model

2.4.1 Jackson's model for ion beam induced solid phase epitaxy

A model for ion beam-induced motion of a planar crystal-amorphous interface via crystallization or amorphization at the interface has been developed by Jackson [8]. This model has been successfully tested against many experimental data. For example, as Figs. 2.2 and 2.3 partially reveal, it gives excellent agreement with data reported for irradiation-induced Si crystallization or amorphization using 1.5 MeV Xe^+, Kr^+, Ar^+, and Ne^+ ions, with ion fluxes between 5×10^{11}–5×10^{14} ions/cm^2 s, and sample temperatures between 150–500 °C [8]. In addition, it has been widely used by other authors as a basis for explaining planar c-a interface motion, as well as nucleation and growth of Si crystals in a-Si [1, 3, 4, 11], under ion irradiation. In the next section, it will be extended to include the effect of the surface free energy (which does not affect velocity of a planar c-a interface because it has a zero surface-to-volume ratio) of a crystal on its growth and amorphization rate. It will be shown that, as the size of a crystal under ion irradiation approaches infinity, the growth rate calculated with this generalized model agrees with that calculated with the original model, as it should. In order to provide a framework for discussing this generalized model, Jackson's model is outlined below.

In Jackson's model, the rate of interface movement, R_{ca}, is the difference between the crystallization rate and the amorphization rate:

$$R_{ca} = R_c - R_a. \tag{2.20}$$

The amorphization rate, R_a, is directly proportional to the ion flux, ϕ:

$$R_a = V_a \phi, \tag{2.21}$$

where V_a is the volume of amorphous region created at a c-a interface by an ion and is temperature independent. As for crystallization, it is assumed to be caused by the motion of a type of defect in Si created by the ions. The nature of the defects is not specified in this model, only that the defects must annihilate in pairs, and that they must have an activation energy for migration of 1.2 eV. This is the activation energy obtained from experiments when temperature vs. ion flux was plotted for the cases where $R_{ca} = 0$. Since a vacancy diffusing in Si has an activation energy of 0.33 eV, and that of a interstitial diffusing in Si is believed to be even smaller, they are deemed unlikely to be the defect type responsible for crystallization in this model. It was speculated by Jackson that the defects are dangling bonds in amorphous Si, which has a band gap energy comparable to 1.2 eV.

The crystallization rate, R_c, is proportional to the steady state defect density N_{av} and the defect jump rate ν:

$$R_c = a N_{av} \Lambda \nu, \tag{2.22}$$

where a is the defect jump distance, and Λ is the volume of crystal created by a defect each time it jumps. For simplicity, it is assumed that each ion creates a uniform density of defects within a cascade cylinder of diameter l_0 centered around the path of the ion. Then the volume density of defects at the interface is, within a geometrical factor,

$$N_0 = N_1 / l_0^2, \tag{2.23}$$

where N_1 is the number of defects created by an ion along its path, per unit distance. A schematic of the creation of defects around the paths of ions and also of the irradiation-induced movement of the crystal-amorphous interface is shown in Fig. 2.11. The average time between arrival of ions in a cascade cylinder is

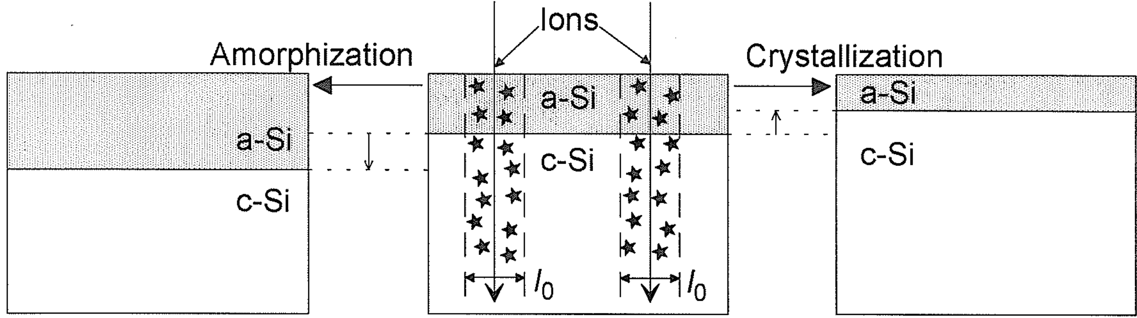

Figure 2.11: Schematic of the creation of defects by ions as they traverse through a Si sample containing an amorphous Si (a-Si) layer on top of crystalline Si (c-Si). In Jackson's model, it is assumed that a uniform density of defects is generated inside cylinders of diameter l_0 centered around the paths of the ions. In this model, the relative rate of the amorphization process (due to the amorphous regions created by the ions) and the crystallization process (due to the defect migrations) at the crystal-amorphous interface determines whether the ion irradiation induces layer-by-layer crystallization or amorphization.

$$\tau_0 = 1/l_0^2\phi. \tag{2.24}$$

The time average defect density can be calculated from the rate of change of defects, which is given by

$$\frac{dN}{dt} = -N(N\sigma^2 a\nu). \tag{2.25}$$

Here σ^2 is the cross section area for defect annihilation, and ν, the defect jump frequency is given by

$$\nu = \nu_0 e^{-E/kT}, \tag{2.26}$$

where E is the activation energy for defect migration, and ν_0 is the unbiased jump frequency. Therefore, $\sigma^2 a\nu$ is the capture volume swept out by a defect per unit time. Let τ_j denote the jump period, then

$$1/\tau_j = \nu. \tag{2.27}$$

The density after the arrival of the first ion is obtained by integrating Eq. 2.25:

$$N = N_0/(1 + N_0\sigma^2 at/\tau_j). \tag{2.28}$$

Defect density decreases with time until the the arrival of the next ion. After the ith ion, the defect density is given by

$$N^i = \frac{N_0^i}{1 + N_0^i \sigma^2 a(t - i\tau_0)/\tau_j}, \tag{2.29}$$

where N_0^i is the defect density immediately after the ith ion arrives. At steady state the decrease in density after period τ_0 is balanced by the increase in density by N_0 created by the next ion; thus

$$N_0^i = N_0^{i+1} = \frac{N_0^i}{1 + N_0^i \sigma^2 a \tau_0/\tau_j} + N_0. \tag{2.30}$$

Therefore the steady-state value of N_0^i is given by

$$(N_0^i)_{ss} = (N_0/2)(1 + \sqrt{1 + 4/\gamma}), \tag{2.31}$$

where

$$\gamma = N_0 \sigma^2 a \tau_0/\tau_j. \tag{2.32}$$

A diagram of defect density evolution with time inside a cascade cylinder is shown in Fig. 2.12. The average defect concentration in the period between arrival of the ith and $(i+1)^{th}$ ion is given by

$$\begin{aligned} < N^i > &= \frac{1}{\tau_0} \int_0^{\tau_0} \frac{N_0^i dt}{1 + N_0^i \gamma t / N_0 \tau_0} && (2.33) \\ &= (N_0/\gamma) \ln[1 + \gamma(N_0^i/N_0)]. && (2.34) \end{aligned}$$

So the average defect density at steady state is

$$N_{av} = \frac{N_0}{\gamma} \ln\left[1 + \frac{\gamma}{2}\left(1 + \sqrt{1 + \frac{4}{\gamma}}\right)\right]. \tag{2.35}$$

Finally, the interface movement rate is given by

$$R_{ca} = \frac{\Lambda l_0^2 \phi}{\sigma^2} \ln\left[1 + \frac{\gamma}{2}\left(1 + \sqrt{1 + \frac{4}{\gamma}}\right)\right] - V_a \phi. \tag{2.36}$$

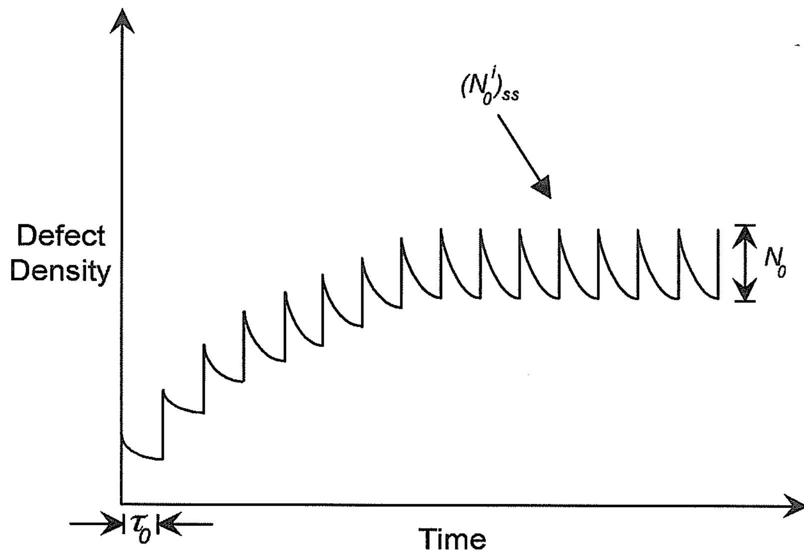

Figure 2.12: Schematic of defect concentration as a function of time. Defect concentration in a region increases by N_0 each time an ion passes through the region. Afterwards the defect density decreases with time via bimolecular recombination. Gradually the time average of the defect concentration increases, and eventually reaches a steady state.

For large γ the above equation becomes

$$R_{ca} = \frac{\Lambda l_0^2 \phi}{\sigma^2}\left[\ln\left(\frac{\phi_0}{\phi}\right) - \frac{E}{kT}\right], \tag{2.37}$$

where

$$\phi_0 = \frac{N_1 \sigma^2 a \nu_0}{l_0^4 \exp\left(V_a \sigma^2 / \Lambda l_0^2\right)}. \tag{2.38}$$

The flux for which no interface movement occurs is obtained by setting R_{ca} to 0 in Eq. 2.36, and is given by

$$\phi = \frac{N_1 \sigma^2 a \nu_0}{l_0^4} \frac{\eta}{(1-\eta)^2} e^{-E/kT}, \tag{2.39}$$

where

$$\eta = \exp\left(\frac{V_a \sigma^2}{\Lambda l_0^2}\right). \tag{2.40}$$

It is clear from the two above equations that in Jackson's model ion flux vs. transition temperature (temperature where $R_{ca} = 0$) has an Arrhenius form, and

the activation energy is independent of the ion species, which is in agreement with experiment, as Fig. 2.3 shows. Furthermore, from Eq. 2.37 it is evident that a weak temperature dependence of the interface velocity is predicted by this model, which is also in good agreement with experiment, as Fig. 2.2 shows. The interface velocity depends linearly on $1/kT$, instead of exponentially, like other thermally-activated processes such as SPE. As Jackson pointed out, this is due to the fact that the defect jump rate and the inverse of the defect lifetime has the same temperature dependence, so the number of jumps—and the volume of crystals—a defect can make does not dependent on temperature, to the first order. The slight temperature dependence of the interface displacement rate is due to the encounter between defects created by different ions. At low temperatures defects are less mobile and have longer life times, so more of them will be annihilated by defects generated by successive ions in the same region, resulting in less defect-promoted crystal growth.

2.4.2 A model for size-dependent ion beam induced crystal evolution

In this section a model for size-dependent crystal evolution under ion irradiation is presented. This is a generalization of Jackson's model, and includes two important thermodynamic parameters missing from that model—the surface and volume free energy of a crystal—in order to treat the case of *non-planar* interface motion under ion irradiation. For simplicity an interface with a constant curvature is assumed, which corresponds to the interface of a spherical crystal in an amorphous matrix. Thus, in the context of the present model, a planar interface corresponds to the interface of an infinitely large crystal. For a spherical grain, the rate of interface movement corresponds to the growth rate, i.e.,

$$R_{ca} = \frac{dr}{dt}. \tag{2.41}$$

The assumption of spherical grain shape under ion irradiation is reasonable, as Figs. 2.4–2.6 show.

The present model is based on transition-state theory [29]. In this model, as in classical nucleation theory, the stability and the growth rate of a grain is governed by its free energy, which is the sum of the volume and surface free energy. In classical nucleation theory, grains smaller than the critical size, r_{tc}, will likely shrink and grains larger than the critical size will likely grow in order to lower their free energy. However, under ion irradiation even a thermally stable grain—a grain larger than r_{tc}—might shrink because the amorphization due to atomic displacements by the ions could overcome the crystallization due to defect motions and reduce its size below r_{tc}. Therefore the critical size under ion irradiation, r_{ic}, is always larger than r_{tc}.

Following the Turnbull and Fisher model [29], the forward transition rate of a system, from state i to state $(i+1)$, is given by

$$\nu_f = \nu_0 e^{-(E_m + \frac{1}{2}\Delta E_i)/kT} \tag{2.42}$$

where ΔE_i is the free energy difference between state $(i+1)$ and state i. Similarly, the backward transition rate is given by

$$\nu_b = \nu_0 e^{-(E_m - \frac{1}{2}\Delta E_{i-1})/kT}. \tag{2.43}$$

The free energy diagram of the reaction path is illustrated in Fig. 2.13. Suppose that a grain is in state i, characterized by a volume V_i, which has an associated energy of E_i. When a defect on the surface of the grain jumps forward in phase space—a distance a in real space, crystallization occurs, and the grain volume becomes V_{i+1}; conversely, when a defect jumps backward in phase space, amorphization occurs, and the grain volume becomes V_{i-1}.

The rate of transition from state i to state $(i+1)$ for a grain is proportional to the density of defects on its surface and the forward jump rate of those defects.

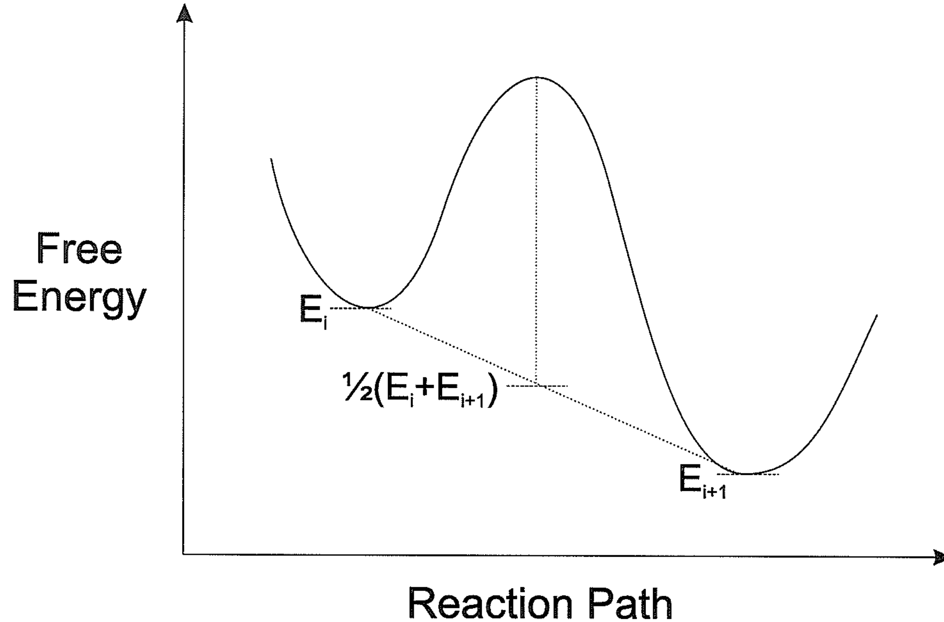

Figure 2.13: Free energy diagram of the reaction path of a defect. When a Si crystal is in state i it has a free energy of E_i. A forward jump of a defect on the surface of the crystal brings the crystal into state $(i+1)$, with energy E_{i+1}, and vice versa. The energy barrier of a defect jump depends on the free energy of the crystal before and after the jump. The barrier is lowered if the crystal has a lower free energy after the jump, and vice versa.

Similarly, the rate of transition from state i to state $(i-1)$ is proportional to the defect density and their backward jump rate. Accordingly, the crystallization term, Eq. 2.22, becomes

$$R_c = aN_{av}\Lambda(\nu_f - \nu_b), \tag{2.44}$$

where the net crystallization rate equals the forward transition rate minus the backward transition rate. In addition, the rate of defect annihilation (Eq. 2.25) becomes

$$\frac{dN}{dt} = -N[N\sigma^2 a(\nu_f + \nu_b)]. \tag{2.45}$$

Note that in this case the net defect jump rate is the sum, rather than the difference, of the forward and the reverse rate. This makes sense intuitively, since $\sigma^2 a(\nu_f + \nu_b)$ is the collision volume traversed by a defect per unit time.

To calculate the amorphization rate of a grain, R_a, assume that amorphization

occurs in a layer-by-layer fashion at the surface of a crystal. This has been shown to be true for large crystals at 150–225 °C [12]. Accordingly, the time average rate of amorphization of a grain of radius r can be written as

$$R_a = -\overline{\frac{dr}{dt}} = V_a\phi, \tag{2.46}$$

which is the same as in the case of a planar c-a interface. Thus the rate of interface movement is given by

$$R_{ca} = \frac{dr}{dt} = \frac{\Lambda l_0^2 \phi}{\sigma^2}\left(\frac{\nu_1}{\nu_2}\right) \ln\left[1 + \frac{\gamma_r}{2}\left(1 + \sqrt{1 + \frac{4}{\gamma_r}}\right)\right] - V_a\phi, \tag{2.47}$$

where

$$\nu_1 = \nu_f - \nu_b \tag{2.48}$$

$$\nu_2 = \nu_f + \nu_b \tag{2.49}$$

and

$$\gamma_r = N_0\sigma^2 a\tau_0\nu_2. \tag{2.50}$$

In order to evaluate the above expressions, ν_f and ν_b, which depend on ΔE_i, must be calculated. By definition,

$$\Delta E_i = \Delta G_{i+1} - \Delta G_i, \tag{2.51}$$

where ΔG_i is the free energy required for form a grain of volume V_i, or a radius of r_i. Thus

$$\Delta G_i = \Delta G(V_i), \tag{2.52}$$

$$\Delta G_{i+1} = \Delta G(V_{i+1}), \tag{2.53}$$

and

$$V_i = \frac{4}{3}\pi r_i^3. \tag{2.54}$$

According to classical nucleation theory,

$$\Delta G(r) = -\frac{4}{3}\pi r^3 \Delta g_v + 4\pi r^2 \sigma_s, \tag{2.55}$$

where Δg_v is the change in free energy per unit volume upon crystallization, and σ_s is the c-a interface energy per unit area. A defect creates Λ volume of crystal each time it jumps, so $V_{i+1} = V_i + \Lambda$. Since Λ is very small (less than one atomic volume [8, 31]), $\Delta G(V_{i+1})$ can be expanded in a Taylor series:

$$\Delta G(V_i + \Lambda) = \Delta G(V_i) + \frac{d\Delta G}{dV}\Lambda + \cdots \tag{2.56}$$

$$= \Delta G(V_i) + \frac{d\Delta G}{dr}\frac{dr}{dV}\Lambda + \cdots \tag{2.57}$$

Using Eqs. 2.54 and 2.55 the above equation becomes

$$\Delta G(V_i + \Lambda) = \Delta G(V_i) + \left(-\Delta g_v + \frac{2\sigma_s}{r_i}\right)\Lambda, \tag{2.58}$$

where higher order terms in the Taylor series have been ignored. Thus,

$$\Delta E_i = \left(-\Delta g_v + \frac{2\sigma_s}{r_i}\right)\Lambda. \tag{2.59}$$

Putting the above expression into Eq. 2.42, the forward jump rate becomes

$$\nu_f = \nu_0 e^{-E_m/kT} e^{\frac{1}{2}(\Delta g_v - 2\sigma_s/r)\Lambda/kT}. \tag{2.60}$$

The reverse jump rate can be derived in a similar manner, and is given by

$$\nu_b = \nu_0 e^{-E_m/kT} e^{-\frac{1}{2}(\Delta g_v - 2\sigma_s/r)\Lambda/kT}. \tag{2.61}$$

The derivation above assumes that grain size as a function time can be approximated by a smooth curve, though in reality its has a serrated shape, on an atomic scale. Under irradiation, the temporal evolution of the volume of a grain is similar

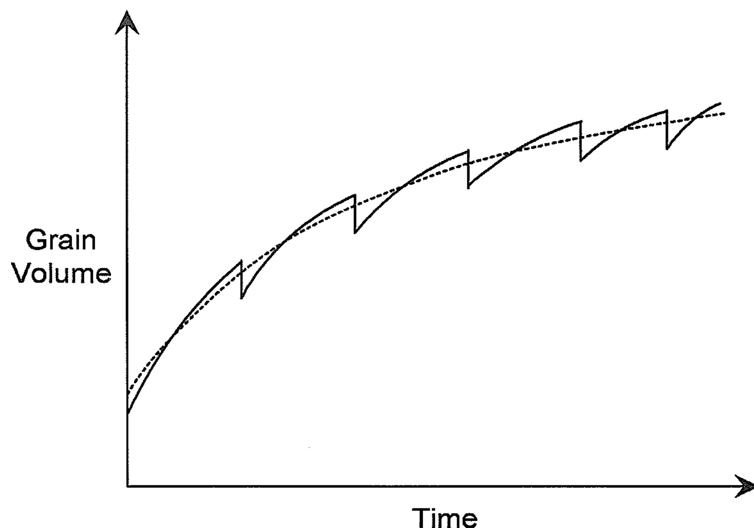

Figure 2.14: Schematic of size as a function of time for a grain under ion irradiation. Solid line: actual volume; dashed line: time average volume. When an ion traverses through a grain, the grain volume is instantly reduced by the atomic displacements within the collision cascade of the ion. Subsequently defects created by the ion increase the volume of the grain by thermal migration. As a grain grows the probability of it being hit by an ion increases, so the interval between arrival of ions decreases.

to that depicted in Fig. 2.14. When an ion traverses through the grain, the grain volume is instantly ($\sim 10^{-13}$ s) reduces by an amount proportional to V_a and the size of the crystal. After the ion passes, the defects created inside its collision cascade increase the grain volume via thermal migration. As time elapses the defect density decreases through recombination and the rate of crystallization declines. When the next ion arrives ($\sim 10^{-4}$–10^{2} s) the amorphization-crystallization cycle is repeated. As a crystal grows its cross section area increases, so the interval between arrival of ions shortens. For large grains, i.e., grains with volume $> V_a$ (about 20–100 atoms), the decrease in radius caused by each amorphization event is small enough that the instantaneous radius and the time average radius do not differ significantly. In these cases, the time-averaged radius can be used to calculate the forward and reverse jump rates using Eqs. 2.60 and 2.61.

For a planar c-a interface, i.e., for $r \to \infty$, the expression for growth rate from this model, Eq. 2.47, is equivalent to that of Jackson's model, Eq. 2.36. Specifically,

for $r \to \infty$, the jump rates become

$$\nu_f = \nu_0 e^{-E_m/kT} e^{\frac{1}{2}\Delta g_v \Lambda/kT}, \quad (2.62)$$

$$\nu_b = \nu_0 e^{-E_m/kT} e^{-\frac{1}{2}\Delta g_v \Lambda/kT}. \quad (2.63)$$

For $\frac{1}{2}\Delta g_v \Lambda > kT$, $\nu_f \gg \nu_b$. Therefore $\nu_1 \approx \nu_2 \approx \nu$, $\gamma_r \approx \gamma$, and Eq. 2.47 is equivalent to Eq. 2.36, provided that

$$E = E_m - \frac{1}{2}\Delta g_v \Lambda. \quad (2.64)$$

In other words, if the lowering in the free energy of a system due to a forward defect jump at its c-a interface is large compared to the thermal energy kT, then the reverse defect jump rate is negligible compared to the forward defect jump rate, and Jackson's model is recovered.

2.4.3 Critical radius under ion irradiation

Under ion irradiation, when the target temperature is low and/or the ion flux is high, layer-by-layer amorphization occurs at a planar c-a interface. In this amorphization regime, crystals of all sizes will shrink. However, in the crystallization regime for a planar c-a interface, there exists a temperature-dependent critical radius, r_{ic}; crystals larger than r_{ic} grow while crystals smaller than r_{ic} shrink. This is shown in Fig. 2.15, which is a plot of the growth rate (Eq. 2.47) as a function of size at different temperatures. The parameters for Eq. 2.47 were obtained by fitting it to the data from Fig. 2.10, and are discussed in Sec. 2.5.1.

To obtain the critical radius under ion irradiation, set dr/dt equal to zero. Then Eq. 2.47 becomes

$$\left[1 + \frac{\gamma_r}{2}\left(1 + \sqrt{1 + \frac{4}{\gamma_r}}\right)\right] = \beta \quad (2.65)$$

where

$$\beta = \exp\left[\frac{V_a \sigma^2}{\Lambda l_0^2}\frac{\nu_2}{\nu_1}\right]. \quad (2.66)$$

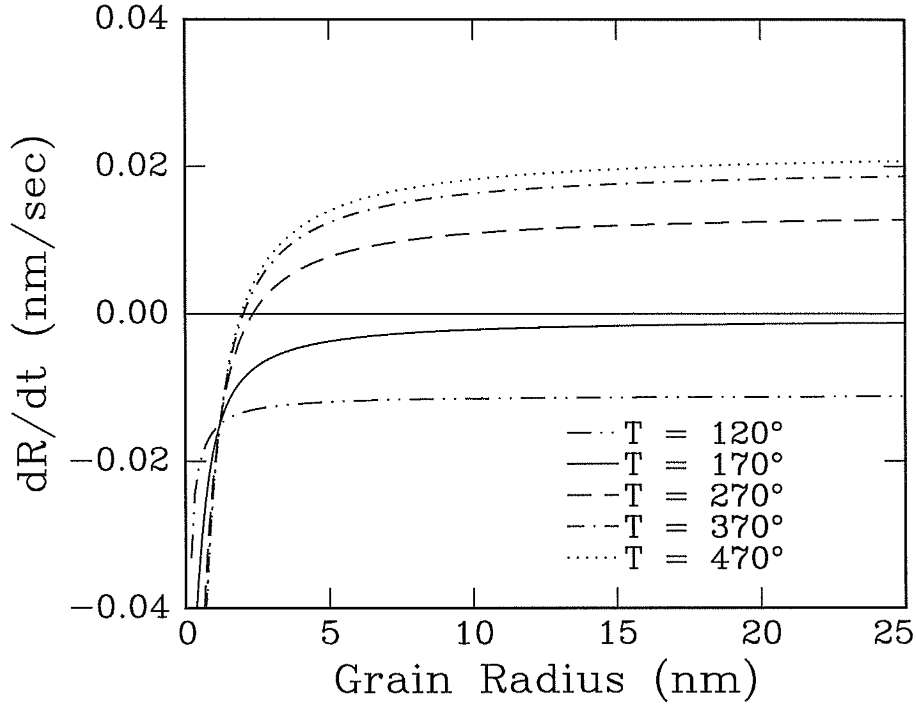

Figure 2.15: Calculated growth rate as a function of size at various temperatures for the same experimental conditions as those in Figs. 2.4–2.6. The Ar^+ ion energy is 250 keV, and the ion flux is 1×10^{12} ion/cm^2 s. The rest of the parameters for the growth rate are listed in Sec. 2.5.1. For temperatures below 173 °C, crystals of all sizes will shrink. For higher temperatures crystals larger than the temperature-dependent critical radius will grow.

Thus γ_r becomes

$$\gamma_r = \frac{(1-\beta)^2}{\beta} = \frac{1}{\beta} - 2 + \beta. \tag{2.67}$$

Since all the variables on the RHS of Eq. 2.66 are positive, β must be greater than 1. For large γ_r, $\beta \gg 1$, and γ_r can be approximated as

$$\gamma_r = \beta - 2. \tag{2.68}$$

This approximation becomes more accurate at high temperatures since γ_r increases with temperature. Simplify the expression for γ_r and β by letting

$$x = \frac{1}{2}\left(\Delta g_v - \frac{2\sigma_s}{r}\right)\Lambda/kT. \tag{2.69}$$

Then

$$\begin{aligned} \gamma_r &= 2N_0\sigma^2 a\tau_0\nu_0 e^{-E_m/kT}\left[\frac{e^x+e^{-x}}{2}\right] = A\left[\frac{e^x+e^{-x}}{2}\right] && (2.70)\\ &= A\cosh(x). && (2.71)\end{aligned}$$

Similarly, β becomes

$$\begin{aligned} \beta &= \exp\left[\frac{V_a\sigma^2}{\Lambda l_0^2}\frac{\nu_2}{\nu_1}\right] && (2.72)\\ &= \exp\left[\frac{V_a\sigma^2}{\Lambda l_0^2}\frac{\cosh(x)}{\sinh(x)}\right] && (2.73)\\ &= \exp\left[B\coth(x)\right]. && (2.74)\end{aligned}$$

It will be shown in the next section that the value of x is always less than 1 in the temperature range of interest, and decreases toward 0 as $r_{ic} \to r_{tc}$. In addition, it is apparent from the definition of x that its value decreases with temperature. For small x the term $A\cosh(x)$ can be approximated by the first two terms in a Taylor series, which, combined with Eq. 2.68 and 2.71, gives

$$\begin{aligned} \gamma_r = A &= \beta - 2 && (2.75)\\ A &= \exp\left[B\coth(x)\right] - 2, && (2.76)\end{aligned}$$

so

$$x = \tanh^{-1}\left[\frac{B}{\ln(A+2)}\right], \quad (2.77)$$

where

$$\begin{aligned} A &= 2N_0\sigma^2 a\tau_0\nu_0 e^{-E_m/kT} && (2.78)\\ B &= \frac{V_a\sigma^2}{\Lambda l_0^2}. && (2.79)\end{aligned}$$

The critical radius r_{ic} can be obtained from the definition of x, Eq. 2.69:

$$\frac{2xkT}{\Lambda} = \Delta g_v - \frac{2\sigma_s}{r_{ic}} \tag{2.80}$$

$$r_{ic} = \frac{2\sigma_s}{\Delta g_v - 2xkT/\Lambda}, \tag{2.81}$$

where x is given by Eq. 2.77. It should be noted that if $V_a = 0$, then $B = 0$; hence $x = 0$, and r_{ic} becomes

$$r_{ic} = \frac{2\sigma_s}{\Delta g_v}, \tag{2.82}$$

which is the critical size for thermal stability, r_{tc}. In other words, if ions do not create amorphous regions, then $r_{ic} = r_{tc}$, assuming that the value of σ_s and Δg_v are unchanged under ion irradiation.

2.5 Comparison of model to data

2.5.1 Data from present experiment

A fit of Eq. 2.47 to the experimentally determined growth rate from Fig. 2.10 is shown in Fig. 2.16. The two adjustable parameters are: $V_a = 1.5 \times 10^{-21}$ cm^3, and $l_0^2 = 1.77 \times 10^{-13}$ cm^2. These two parameters, along with N_1, depend on ion species and energy, while the rest of the parameters in Eq. 2.47 depend only on the target material. The value of N_1, 5.0×10^7 cm^{-1}, is equal to the number of atomic displacements created by a 250 KeV Ar^+ ion in Si, calculated using the TRIM program [26], in accordance with Jackson's method of data fitting [8]. The target-dependent parameters can be obtained from Jackson's model and from data on thermal SPE. The parameters are: $\sigma^2 = 2.93 \times 10^{-15}$ cm^2 [8], $\Lambda = 1.0 \times 10^{-23}$ cm^3, $\nu_0 = 4.265 \times 10^{15}$ s^{-1} [8], $E_m = 1.922 \times 10^{-19}$ J (1.2 eV) [8], $\Delta g_v = 801.0$ J/cm^3 (.1 eV/atom) [35], and $\sigma_s = 4.8 \times 10^{-5}$ J/cm^2 (.15 eV/atom) [36]. The fit between model and data is excellent, except for the observed growth rate at the smallest size class. This is due to the inaccuracy of the histogram at that size range, as explained previously. Extrapolating the growth rate to infinitely large crystal size using Eq. 2.47, a rate of

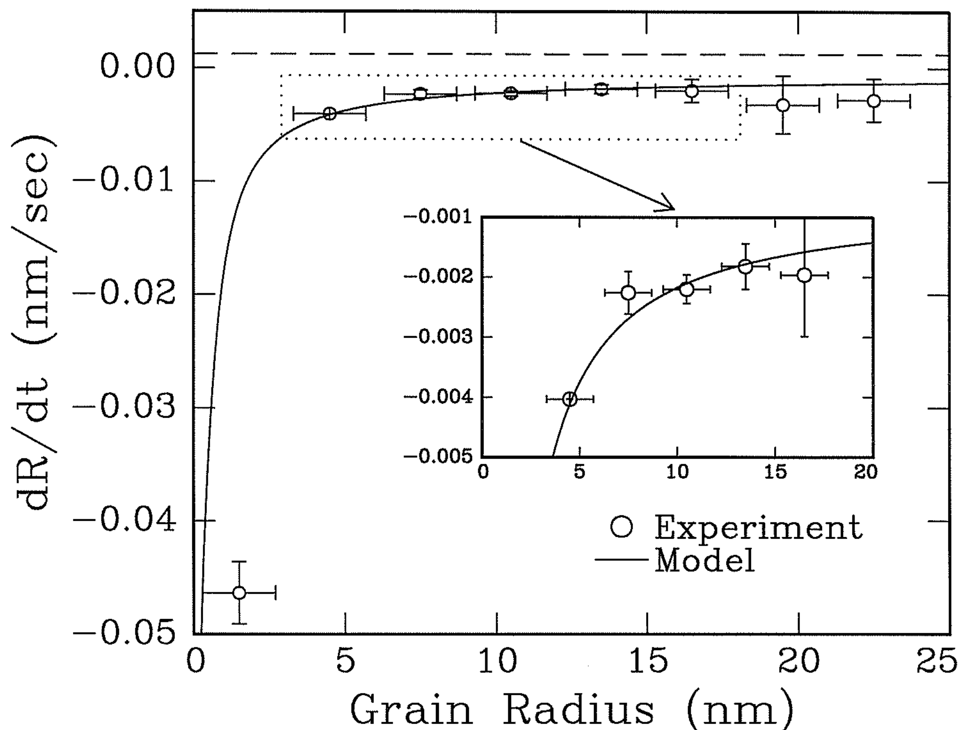

Figure 2.16: Calculated growth rate as a function of size (from Fig. 2.10) and a fit from the present model (Eq. 2.47). The dashed line is the interface velocity of a planar (100) c-a interface from Fig. 2.9, 1.25×10^{-3} nm/s. Because ion assisted SPE is faster for the (100) planes than for the (111) planes, this interface velocity should be higher than the evolution rate of an infinitely large crystal. Indeed, dr/dt for $r \to \infty$, from the present model, is -0.68×10^{-3} nm/s.

-0.68×10^{-3} nm/s is obtained. This is less than the [100] SPE rate of $1.25 \pm .25 \times 10^{-3}$ nm/s, obtained in Sec. 2.3, which is consistent with the observation that the ion-induced crystallization of (111) planes is slower than that of the (100) planes [10, 27],

A plot of x vs. r_{ic}, using Eq. 2.69 and the above parameters, is shown in Fig. 2.17. As the figure shows, x decreases with temperature, and is always less than 1. This justifies the use of Taylor expansion of $A\cosh(x)$ in Eq. 2.75. The parameters used to calculate x only depend on the properties of the target material; therefore Fig. 2.17 a universal curve for all irradiation experiments involving Si. In addition, as the critical size, r_{ic}, decreases toward r_{tc}, $x \to 0$, and Eq. 2.75 becomes an excellent approximation.

A plot of the critical radius vs. temperature using Eq. 2.81 is shown in Fig. 2.18.

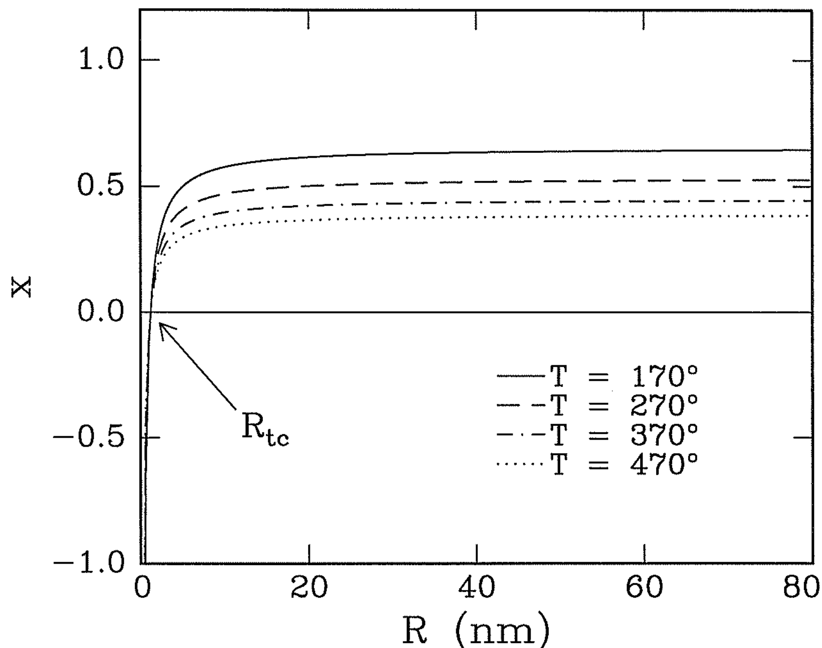

Figure 2.17: Plot of x as a function of radius. See text for definition of x. The value of x only depends on the target material used in the ion irradiation, not on the ion species used, and is always less than one. This justifies the use of Taylor expansion of $\cosh(x)$.

Also shown in the figure is the exact solution for r_{ic}, which was obtained by solving Eq. 2.65 numerically. The agreement between the two curves is excellent, especially at high temperatures. The critical radius decreases with temperature, but is always larger than r_{tc}, which is 12 Å.

By combining the rate equation of Eq. 2.47 and the continuity equation of Eq. 2.2, it's possible to calculate the temporal evolution for any crystal size distribution. This has been done for the size distributions in Fig. 2.7, and is shown in Fig. 2.19. The continuity equation was solved numerically using the computer program listed in Appendix A. The program is written in C, and uses a finite-difference algorithm described elsewhere [38]. A spline fit [34] of the size distribution from the unirradiated sample was used as the initial distribution. Next, size distributions were computed for the three ion doses using the parameters listed above for Eq. 2.47, and compared to the experimentally obtained distributions. In addition, size distributions were cal-

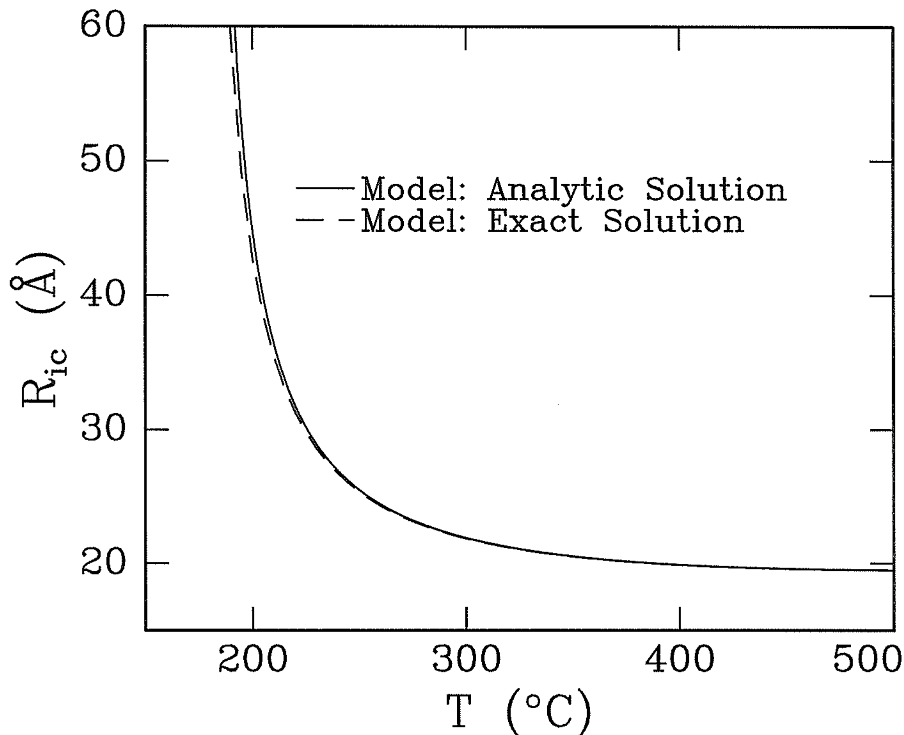

Figure 2.18: Plot of the critical radius as a function of temperature. The solid line is the analytic solution which involved some approximations, and the dashed line is the exact solution, obtained by solving the equation $dr/dt = 0$ numerically.

culated using a size-independent growth rate of -2.42×10^{-3} nm/s. It is obvious from Fig. 2.19 that the distributions calculated using the present model fit the observed distributions much better than the distributions calculated using a constant growth rate. The differences between the two computed distributions are especially noticeable for particle sizes of 6–12 nm. For this size class the distributions calculated for a constant growth rate differed from the observed distributions by a factor of two or more, for all three ion doses. Since the histogram statistics are very good for particles of this size class, these differences cannot be attributed to experimental error. Note that the computed distributions are not affected by the value—therefore, the uncertainty—of the initial distribution at the smallest size class, f_0^0, because all of the grains in that size class completely disappeared at an ion dose of 2×10^{15} ions/cm^2, the smallest ion dose used.

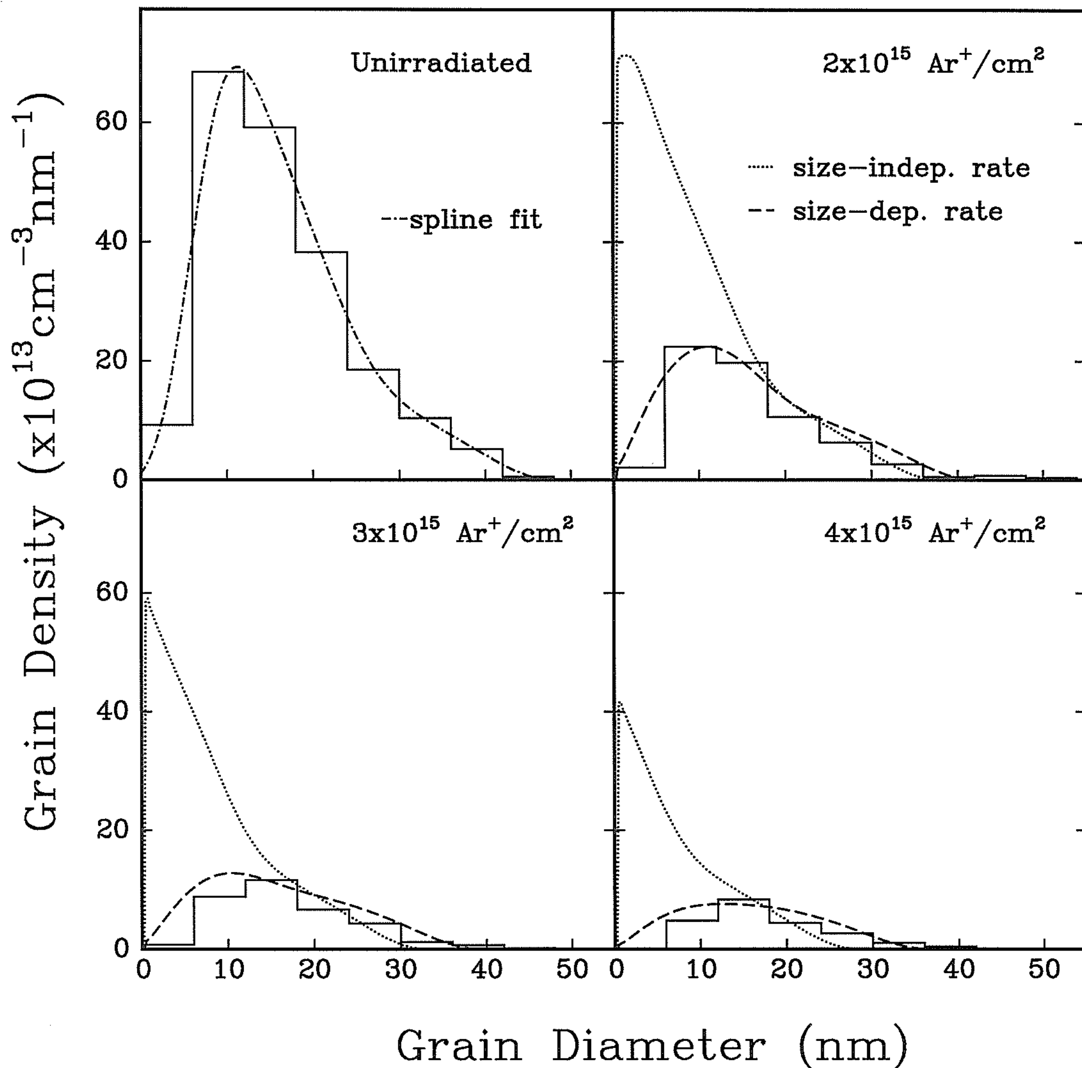

Figure 2.19: Calculated and measured grain size distributions for ion beam induced amorphization. The histograms are the same as those in Fig. 2.7. A spline fit of the size distribution from an unirradiated sample was used as the initial distribution. The dashed lines are the distributions calculated from the initial distribution using the size-dependent growth rate from the present model. The parameters for the growth rate are the same as those used in Fig. 2.16. The dotted lines are the size distributions calculated using a size-independent growth rate. It is clear that the distributions obtained with the growth rate from the present model show much better agreement with the observed distributions.

Since the size distributions were calculated using a continuity equation with no source or sink terms, the excellent agreement between the experimental and calculated size distributions confirms the assumptions that there was no crystal nucleation and no single-ion crystal amorphization during the ion irradiation. Had there been crystal nucleation during the 170 °C Ar^+ irradiation, the values of histograms would have been much higher than the calculated values. Similarly, had there been non-interfacial amorphization of crystals by the ions, the values of the histograms would have been much lower than the calculated values. Looking at Fig. 2.19, it might be tempting to suggest that the differences between the calculated and observed crystal populations at the smallest size class are the results of single-ion crystal amorphizations. However, it is more likely that these differences are caused by a limitation in the present experiment: only crystals larger than 4 nm could be observed. It should be noted that because of this limitation, if the ion irradiation had been performed at higher temperatures so that crystals smaller than 4 nm grew, the appearance of these crystals might have been mistaken for the results of irradiation induced nucleation.

2.5.2 Data for ion beam induced crystal growth

Oyoshi *et al.* [4] have performed irradiation induced growth of small crystals in amorphous Si (on glass substrates) at 350 °C. The Si^+ ion flux was 1.6×10^{13} ions/cm s, and the ion energy was 180 keV. The Si films were deposited at 600 °C with atmospheric CVD, and contained 20 nm seed crystals. Their data, along with size distributions calculated using Eq. 2.47 and Eq. 2.2, are shown in Fig. 2.20. The two fitting parameters are: $V_a = 1.5 \times 10^{-21}$ cm^3, and $l_0^2 = 1.14 \times 10^{-13}$ cm^2. The value of N_1, calculated by TRIM, is 3.5×10^7 cm^{-1}. Also shown are the distributions calculated for a constant growth rate of 4.17×10^{-2} nm/s. The broadening of the observed size distribution with ion dose is evident, and is modelled better by the size-dependent growth rate of Eq. 2.47. This is a general trend predicted by the present model, and has been observed in other experiments [37]: because growth rate increases monotonically with size, irradiation induced crystal growth will result in increased crystal

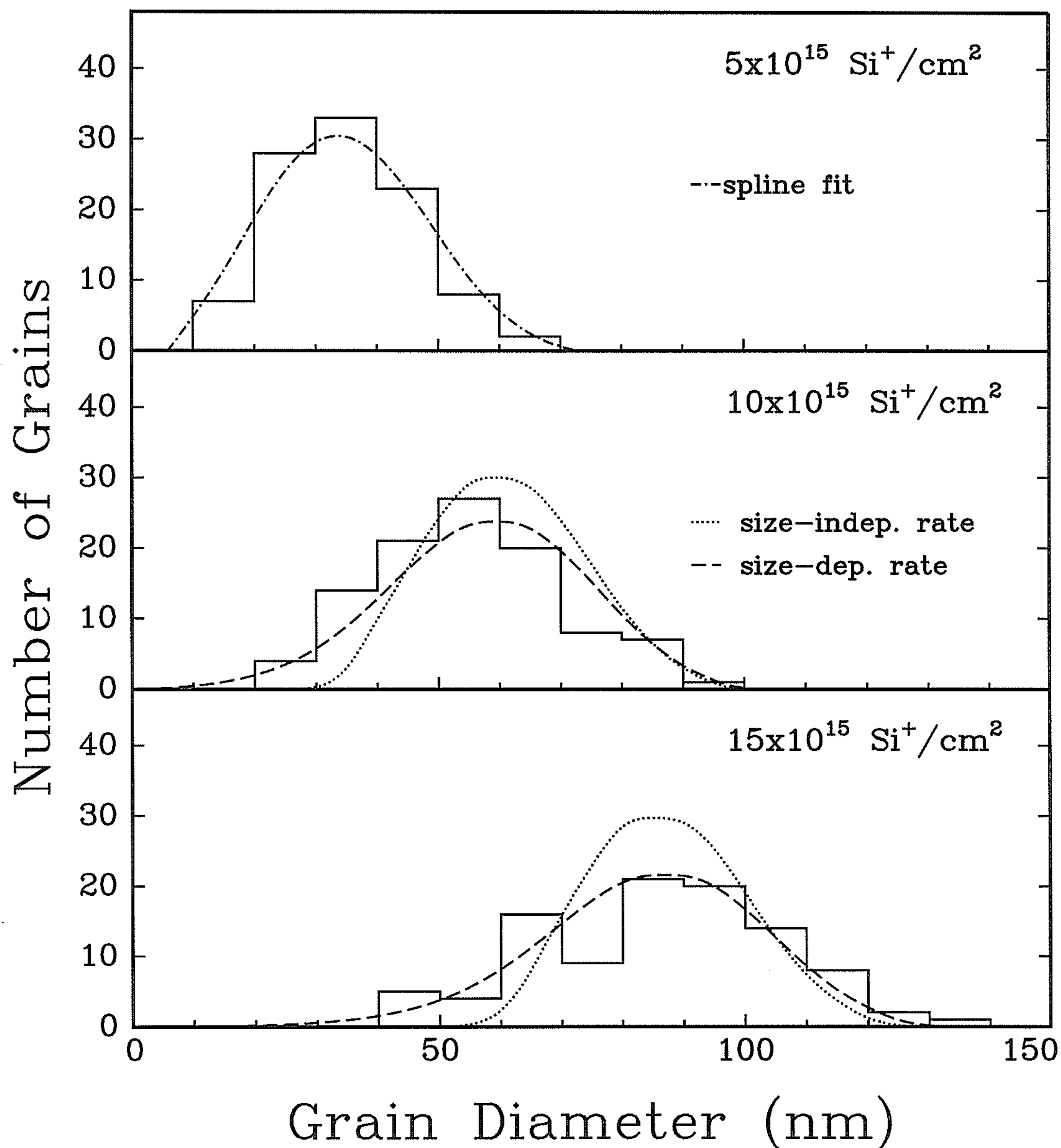

Figure 2.20: Calculated and measured grain size distributions for ion beam induced crystal growth. Data is from Ref. [4]. Samples were made by CVD of 160 nm of a-Si on glass substrates. The Si^+ ion energy was 180 keV, the ion flux was 1.6×10^{13} ions/cm^2 s, and the sample temperature was 350 °C. No size distribution was reported for the unirradiated sample, so the distribution from the 5×10^{15} ions/cm^2 irradiated sample was used as the initial size distribution. The broadening of the observed size distribution with ion dose is evident, and is modelled better by the size-dependent growth rate from the present model.

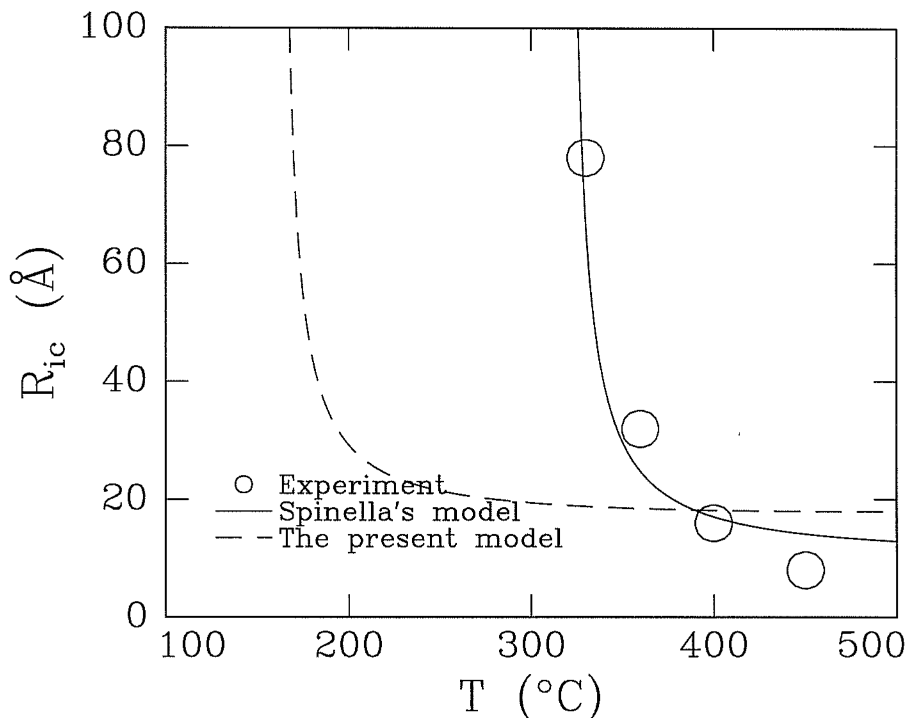

Figure 2.21: Critical size under ion irradiation, as a function of temperature. Data is from Ref. [3]. Samples were made by CVD of 30 nm of amorphous Si on SiO_2. The as-deposited films contained 2–8 nm Si crystals. The Kr^+ ion energy was 600 keV, the ion flux was 1×10^{12} ions/cm^2, and the ion doses were between 5×10^{14} and 3×10^{15} ions/cm^2. The critical radius was obtained from the experimental data by calculating the change in the grain population after ion irradiation, with the assumption that all of the crystals initially below the critical size disappeared after the irradiation. The large discrepancy between the two models and the details of the experiment are explained in the text.

size inhomogeneity. In the experiments of Oyoshi *et al.*, the initial and the final grain density was about the same. In the context of the present model, this indicates that most of the grains in their experiment must have been larger than the critical size. Indeed, the calculated critical radius for this experiment is 6.1 nm, while almost all of the grains counted in their histograms have diameters larger than 15 nm.

Critical size as a function of temperature under ion irradiation has been obtained by Spinella *et al.* [3]. They compared the initial and the final grain densities and calculated the critical sizes at four temperatures. The experiment involved irradiation of CVD grown a-Si films with 600 keV Kr^+ ions, at a dose rate of 1×10^{12} /cm^{2}s, at

temperatures of 330, 360, 400, and 450 °C. The as-deposited Si films contained 2–8 nm seed crystals. Grain size distribution of an unirradiated sample was obtained and fitted to an exponentially decaying function:

$$df/dr = -A\exp(-r/\lambda), \tag{2.83}$$

where $A = 5.4 \times 10^{10}$ cm^{-2} nm^{-1}, and $\lambda = 1$ nm. This function was integrated with respect to size to obtain an equation for the critical radius, which depends on the measured grain density, ρ, after ion irradiation:

$$r_{ic} = -\lambda \ln(\rho/A\lambda). \tag{2.84}$$

Their data, along with a fit from the present model, is presented in Fig. 2.21. Also shown in the figure is a fit of their model, which is discussed in the next section. The two fitting parameters for the present model are: $V_a = 1.5 \times 10^{-21}$ cm^3, and $l_0^2 = 2.0 \times 10^{-13}$ cm^2. The calculated value of N_1 is 1.0×10^8 cm^{-1}. The agreement between their data and the present model is extremely poor. It should be noted that in Fig. 2.21 the critical radius is 16 Å at 400 °C, and 8 Å at 450 °C; since only grains larger than 20 Å could be observed in their experiment, the value of the critical radius at 400 and 450 °C are only speculative at best—they were calculated by extrapolating Eq. 2.83 to sizes smaller than 20 Å. According to Eq. 2.83, the grain population at 10 Å is 7.4 times the grain population at 30 Å. In view of this extremely strong size-dependence, the extrapolation of Eq. 2.83 to $<$ 20 Å is questionable. In addition, from their model, $r_{ic} \rightarrow \infty$ at $T = 320$ °C. This means that the velocity of a *planar* c-a interface should be zero at 320 °C, for ion irradiations using 600 keV Kr$^+$, with a flux of 1×10^{12} ions/cm^2 s. However, data from a published report [39] suggest that this temperature should be in the range of 160–215 °C, which is in good agreement with the value of 160 °C obtained from the present model.

2.6 Discussion

2.6.1 Spinella's model

A model for ion irradiation induced grain growth has been proposed by Spinella [3]. Although this model is also an extension of Jackson's model, its rate equation does not agree with that of Jackson's when extrapolated to $r \to \infty$. Specifically, Spinella's model did not take into account that a) the change in free energy of a grain due to a defect jump depends on the change in the volume of grain caused by the jump, and b) defect concentration near the surface region of a grain depends on the size of the grain.

In Spinella's model, the crystallization rate is written as

$$R_c = a\Lambda N_{av}\nu \left[e^{-\Delta g_n/2kT} - e^{\Delta g_n/2kT}\right], \tag{2.85}$$

where Δg_n is the change in free energy of a crystal when it grows to $n+1$ atoms from n atoms. The above expression implies that each defect jump crystallizes one atom. In Jackson's model, each defect jump creates Λ volume of crystals, where Λ is not necessarily equal to one atomic volume. This has been taken into account in the present model, where R_c is given by

$$R_c = a\Lambda N'_{av}\nu \left[e^{-\Delta g_n \Omega/2kT} - e^{\Delta g_n \Omega/2kT}\right], \tag{2.86}$$

where Ω is the number of atoms crystallized per defect jump (Ω = atomic density of Si divided by Λ.) The above expression can be derived from the present model by writing ΔG as a function of n, expanding $\Delta G(n+\Omega)$ in a Taylor series, and following the same steps used to calculate Eq. 2.60. Incorporation of Λ (and hence Ω) into the pre-exponential term and the exponential terms Eq. 2.86 makes the present model self-consistent.

The forward and reverse defect jump rate on the surface region of a crystal depend on the size of the crystal, as the two equations above imply. Therefore, defect con-

centration around each crystal is size-dependent. This is reflected in Eq. 2.45 in the present model, where defect annihilation rate depends on the forward and backward defect jump frequencies, which depend on crystal radius r, as given by Eqs. 2.60 and 2.61. As a result, N'_{av} in Eq. 2.86 is a function of crystal size. In Spinella's model this size dependence is ignored, and Eq. 2.25 from Jackson's model is still used to calculate the average defect concentration. Because of this neglect, Spinella's model does not agree with Jackson's model when $r \to \infty$.

2.6.2 Nucleation under ion irradiation

Figure 2.18 shows that critical radius under ion irradiation r_{ic} increases with decreasing temperature. Below 500 °C r_{ic} is more than double that of the critical size for nucleation, r_{tc}, which implies that even a crystal twice as large as r_{tc} will gradually shrink under ion irradiation. Thus, ion irradiation tend to decrease nucleation rate at temperatures below 500 °C. At temperatures above 550 °C, the number of thermally generated defects becomes comparable to that of irradiation generated defects [8], which, together with the reduced critical size at higher temperatures, is consistent with the observation that ion irradiation at high temperatures enhances both crystal nucleation and growth rate, but at intermediate temperatures only enhances crystal growth rate. (Thermal generation of defects was included in an extended version of Jackson's model [8] but is not included in the present model because it adds an enormous complexity, and because it is important only at temperatures above 550 °C.)

2.6.3 Activation energy for defect migration

The activation energy E obtained by plotting transition temperature vs. ion flux in irradiation-induced SPE experiments, 1.2 eV, is the free energy barrier for defect migration, according to Jackson's model. In his model the activation energy is the same for all defect. In the present model this energy barrier is not constant but depends on the size of the crystal near which the defects are hopping, e.g., $E =$

$E_m + \Delta E_i/2$, where ΔE_i depends on the size of the crystal. However, the present model can be modified for constant energy barrier, e.g., $E = E_m$. In the absence of a detailed understanding of the atomic mechanism of SPE and an *ab-initio* calculation of its activation process, it is not possible to determine which form of energy barrier is more appropriate. Variable energy barrier is commonly used in calculations of nucleation and growth rate in condensed systems [29, 40], whereas constant energy barrier is commonly used in calculations of SPE rate [15, 23]. In any case, changing the form of the energy barrier, as it will be shown below, has a negligible effect on the results of the present model.

According to transition-state theory, the forward and reverse jump rate between state i and $(i+1)$ is related by

$$\frac{\nu_f}{\nu_b} = e^{-\Delta E_i/kT}, \tag{2.87}$$

which is satisfied by the jump rates in Eqs. 2.42 and 2.43. However, the above equation can also be satisfied by writing the forward and reverse rate as

$$\nu_f = \nu_0 e^{-E_m/kT} \tag{2.88}$$

$$\nu_b = \nu_0 e^{-(E_m - \Delta E_i)/kT}, \tag{2.89}$$

so that the activation barrier for the forward defect jump is independent of the free energy difference between the initial and final state. In this formulation, E_m is equal to the defect migration energy E in Jackson's model. Putting these equations into Eq. 2.47, the ratio ν_1/ν_2 is unaffected, but γ_r becomes

$$\gamma_r^{new} = \gamma_r e^{\Delta E_i/2kT}, \tag{2.90}$$

so that

$$\frac{dr}{dt} = \frac{\Lambda l_0^2 \phi}{\sigma^2}\left(\frac{\nu_1}{\nu_2}\right) \ln\left[1 + \frac{\gamma_r^{new}}{2}\left(1 + \sqrt{1 + \frac{4}{\gamma_r^{new}}}\right)\right] - V_a \phi. \tag{2.91}$$

For $\gamma_r \gg 1$ (true for all the experiments analyzed in this chapter), the rate equation

for the two forms of activation barrier can be written as

$$\frac{dr}{dt} = \frac{\Lambda l_0^2 \phi}{\sigma^2} \left(\frac{\nu_1}{\nu_2}\right) \ln(\gamma_r) - V_a \phi \tag{2.92}$$

for $E = E_m + \Delta E_i/2$, and

$$\frac{dr}{dt} = \frac{\Lambda l_0^2 \phi}{\sigma^2} \left(\frac{\nu_1}{\nu_2}\right) \ln\left(\gamma_r e^{\Delta E_i/2kT}\right) - V_a \phi \tag{2.93}$$

for $E = E_m$. The logarithm term in the above equation can be written as

$$\ln\left(\gamma_r e^{\Delta E_i/2kT}\right) = \ln(\gamma_r) + \Delta E_i/2kT. \tag{2.94}$$

According to Fig. 2.17, x $(= -\Delta E_i/2kT) \approx 0.5$ for $r > r_{tc}$. Since $\gamma_r \gg 1$, $\ln(\gamma_r) \gg \Delta E_i/2kT$. Therefore Eq. 2.92 and Eq. 2.93 produce approximately the same results.

2.7 Summary

The amorphization rates of 4–50 nm crystals under ion irradiation has been obtained from experiment. The results indicate that crystals less than 10 nm shrink substantially faster under ion irradiation than larger crystals. A model for size-dependent crystal growth and amorphization under ion irradiation has been developed and shows good quantitative agreement with the present and other experimental data. In this model, as in classical nucleation theory, smaller crystals grow slower because they have higher surface-to-volume ratio. Hence, irradiation-induced crystal growth will result in increased size dispersion. It has been shown that by using the rate equation from this model and a continuity equation the evolution of the size distribution under ion irradiation can be calculated. Also, an analytic equation for the critical radius under ion irradiation has been obtained. This critical radius, r_{ic}, is always larger than the critical radius for thermal nucleation, r_{tc}. As a result, nucleation under ion irradiation is inhibited until higher temperatures, when r_{ic} approaches r_{tc}.

Bibliography

[1] J. S. Im and Harry A. Atwater, Appl. Phys. Lett. **57**, 1766 (1990).

[2] C. Spinella, A. Battaglia, F. Priolo, and S. Campisano, Europhys. Lett. **16**, 313 (1991).

[3] C. Spinella and S. Lombardo, Phy. Rev. Lett. **66**, 1102 (1991).

[4] K. Oyoshi, T. Yamaoka, T. Tagami, and Y. Arima, J. Appl. Phys. **71**, 648 (1992).

[5] J. Linnros, R. Elliman and W. Brown, J. Mater. Res. **3**, 1208 (1988).

[6] J. Linnros and G. Holmen, J. Appl. Phys. **62**, 4737 (1987).

[7] Sukirno, B. Zeroual, G. Carter and G. Stephens, Nucl. Instr. and Meth. B **67**, 470 (1992).

[8] K. Jackson, J. Mater. Res. **3**, 1218 (1988).

[9] F. Priolo, C. Spinella and E. Rimini, Phys. Rev. B **41**, 5235 (1990).

[10] J. Custer, A. Battaglia, M. Saggio and F. Priolo, Phy. Rev. Lett. **69**, 780 (1992).

[11] C. M. Yang and H. A. Atwater, Mater. Res. Soc. Symp. Procs. **311**, 185 (1993).

[12] H. Atwater and W. Brown, Appl. Phys. Lett. **56**, 1 (1990).

[13] J. Narayan, J. Appl. Phys. **53**, 8607 (1982).

[14] L. Lohmeier, S. de Vries, J. Custer, E. Vlieg, M. Finnery, F. Priolo and A. Battaglia, Appl. Phys. Lett. **64**, 1803 (1994).

[15] G. Olson and J. Roth, Mat. Sci. Rep. **3**, 1 (1988).

[16] L. Csepregi, E. Kennedy, J. Mayer and T. Sigmon, J. Appl. Phys. **49**, 3906 (1978).

[17] F. Spaepen, Acta Meta. **26**, 1167 (1978).

[18] F. Spaepen and D. Turnbull, AIP Conf. Proc. **50**, 73 (1979).

[19] J. Williams and R. Elliman, Phys. Rev. Lett. bf 51, 1069 (1983).

[20] R. Drosd and J. Washburn **53**, 397 (1982).

[21] T. Noma, T. Yonehara and H. Kumomi, Appl. Phys. Lett. **59**, 653 (1991).

[22] R. Iverson and R. Reif, J. Appl. Phys. **62**, 1675 (1987).

[23] Q. Lu, E. Nygren and M. Aziz, J. Appl. Phys. **70**, 5323 (1991).

[24] M. Aziz, P. Sabin and Q. Lu, Phys. Rev. B **44**, 9812 (1991).

[25] W. Brown, R. Elliman, R. Knoell, A. Leiberich, J. Linnros, D. Maher, and J. Williams, in *Microscopy of Semiconductor Materials*, edited by A. Cullis (Institute of Physics, Lindon, 1987), p. 61.

[26] J. Ziegler, J. Biersack and U. Littmark, *The Stopping and Range of Ions in Solids* (Pergamon, New York, 1985).

[27] A. Battaglia, F. Priolo and E. Rimini, Appl. Surf. Sci. **56**, 577 (1991).

[28] S. Roorda, D. Kammann and W. Sinke, Mater. Lett. **9**, 259 (1990).

[29] D. Turnbull and J. Fisher, J. Chem. Phys. **17**, 71 (1949).

[30] R. Iverson and R. Reif, Appl. Phys. Lett. **52**, 645 (1987).

[31] T. Saito and Iwao Ohdomari, Phil. Mag. B **49**, 471 (1983).

[32] C. Spinella, S. Lombardo, and S. Campisano, Appl. Phys. Lett. **55**, 109 (1989).

[33] C. Jayanth and P. Nash, Mater. Sci. and Tech. **6**, 405 (1990).

[34] W. Press, B. Flannery, S. Teukolsky and W. Vetterling, *Numerical Recipes in C* (Cambridge University Press, New York, 1988).

[35] E. Donovan, F. Spaepen and D. Turnbull, J. Appl. Phys. **57**, 1795 (1985).

[36] K. Tu, Appl. Phys. A **53**, 32 (1991).

[37] C. Spinella, S. Lombardo and S. Campisano, Appl. Phys. Lett. **57**, 554 (1990).

[38] C. Yang and H. Atwater, J. Appl. Phys. **67**, 6202 (1990).

[39] A. Battaglia and S. Campisano, J. Appl. Phys. **74**, 6058 (1993).

[40] K. Kelton, A. Greer and C. Thompson, J. Chem. Phys. **79**, 6261 (1983).

Chapter 3 Synthesis of Ge and Si Nanocrystals in SiO_2 via Ion Implantation and Precipitation

3.1 Introduction

The synthesis of luminescent group IV semiconductor nanocrystals has received much attention recently due to potential applications in optoelectronic [1, 2] as well as microelectronic [3] devices. In particular, theoretical works have suggested that sufficiently small group IV semiconductor crystals, of the order of a few nanometers, would exhibit a direct bandgap behavior, allowing efficient radiative recombination of electrons and holes [4, 5, 6]. Experimental verification of the predicted red-shift of the photoluminescence (PL) wavelength with increasing nanocrystal size has been complicated by the presence of defected related luminescence [7, 8]. Nevertheless, PL attributable to Si nanocrystals, obtained after defect-related luminescence was quenched by hydrogen passivation, has been shown recently [9]. For example, Figure 3.1 shows PL spectra of 1–2 nm Si nanocrystals in 100 nm silicon dioxides, synthesized by ion implantation followed by precipitation.

Precipitation of silicon or germanium nanocrystals in silica thin films has been accomplished using many different methods, including rf-magnetron cosputtering of Ge (or Si) and SiO_2 [11]–[14], ion implantation of Ge or Si atoms into SiO_2 [15, 16, 17], or oxidation of $Si_{1-x}Ge_x$ alloys [18, 19], followed by thermal annealing. Silicon dioxide was used as a matrix for embedding the nanocrystals in part because it's a well-characterized dielectric widely used in Si microelectronic devices. Furthermore, it is mechanically robust, has a very high softening temperature, and helps to prevent oxidation or agglomeration of the nanocrystals. Silica containing Ge or Si nanocrys-

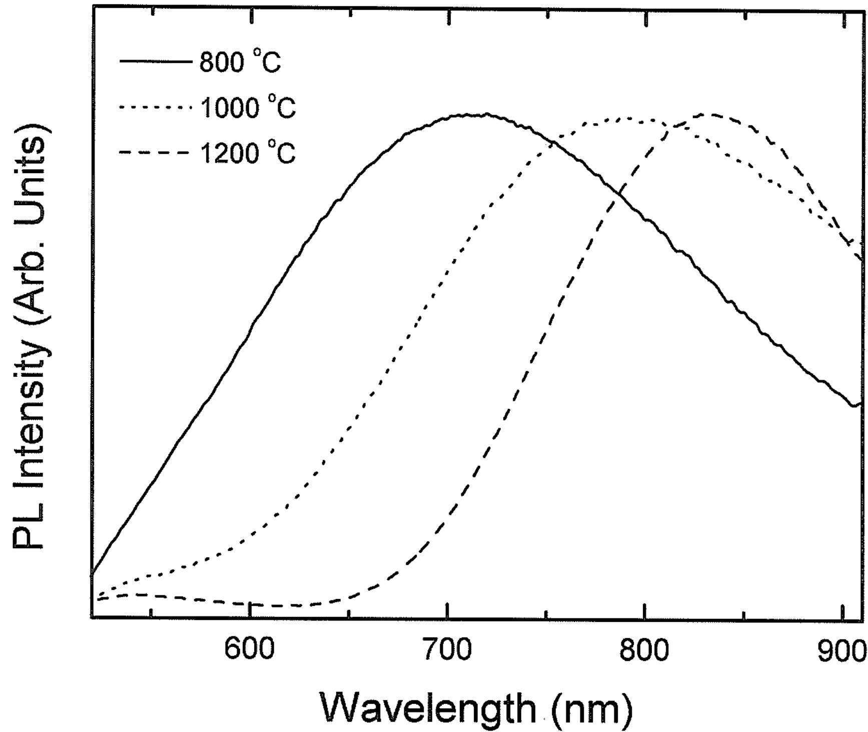

Figure 3.1: Room temperature visible photoluminescence spectra of 100 nm SiO_2 films implanted with 5×10^{16} /cm^2 50 keV $^{28}Si^+$ ions, and annealed at 800 °C, 1000 °C, or 1200 °C for 10 min. Transmission electron microscopy revealed the presence of 1–2 nm Si nanocrystals after the anneal. The luminescence wavelength increased with increasing annealing temperature, which was attributed to increasing average nanocrystal size. Photoluminescence due to defects in SiO_2 were quenched by means of a 600 eV deuterium implantation. After Ref. [9].

tals have been used in electroluminescent and photoluminescent structures [1, 2], as well as in nonvolatile memory devices (as a charge storage layer [3]). Among the synthesis methods described above, ion implantation has the advantage that it allows the precipitation of nanocrystals at selected areas and depth (which is vital for the memory device discussed in Ref. [3]). Although there are other methods of Si or Ge nanocrystal synthesis that does not involve precipitation in silica, such as oxidation of porous silicon [10, 20, 21], electric spark ablation of Si [22], and chemical reduction of chlorogermanes or organochlorosilanes [6], they are deemed less readily applicable to device fabrication.

In this chapter synthesis of Ge and Si nanocrystals in silicon dioxide using ion implantation followed by thermal annealing is described. The purpose of the present

work is to study the nucleation and growth kinetics of the nanocrystals, the knowledge of which might lead to the ability to control nanocrystal size and concentration. Control of size is important because the optical properties of a nanocrystal depend on its size [4, 5, 6], while control of concentration is important because carrier tunneling between nanocrystals increases significantly when they are in close proximity (< 5 nm) [3, 10]. It was found that crystal concentration and size are strongly influenced by implantation dose and post-implantation annealing temperature, respectively. Furthermore, good size uniformity was achieved, with standard deviation σ between 0.5 and 1.8 nm for Ge nanocrystals, about 0.5 nm for Si nanocrystals.

In the current experiment, the evolution of the nanocrystals was characterized using transmission electron microscopy (TEM), and the diffusion of Ge atoms were analyzed by Rutherford backscattering spectrometry (RBS). Observation of Ge nanocrystals was significantly easier than that of Si nanocrystals under TEM, due to higher Z-contrast (electron density contrast) between Ge nanocrystals and the SiO_2 matrix. No Si nanocrystals were found in as-implanted samples or samples annealed at less than 1000 °C. However, Si nanocrystals about 1–2 nm in diameter were visible under high resolution TEM after the Si-implanted samples were annealed at 1000 °C for 40 min. In contrast, nucleation of the Ge nanocrystals took place during implantation, producing 1–2 nm nanocrystals. During subsequent annealing at temperatures higher than 600 °C coarsening, or Ostwald ripening, occurred, increasing the average size to 3.3 nm at 800 °C, 6.9 nm at 1000 °C, and 8.2 nm at 1200 °C. At temperatures lower than 600 °C there was no discernible nucleation or growth. Finally, increasing the Ge implantation dose increased the concentration but did not increase the average size.

3.2 Background

3.2.1 Ge and Si nanocrystal precipitation in SiO_2

Precipitation of Ge or Si nanocrystals in silica supersaturated with Ge or Si atoms lowers the free energy of the system. The structure of silica is composed of a network

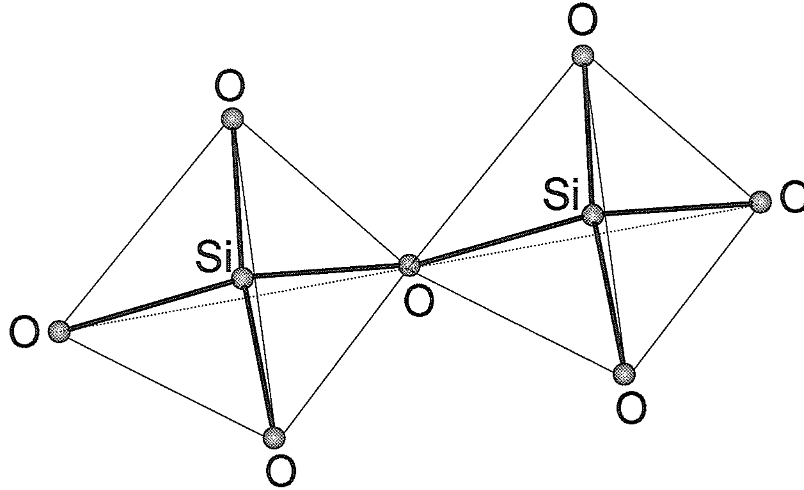

Figure 3.2: An illustration of the structure of silica, which consists of a network of tetrahedrons joined at their corners. Each tetrahedron contains a Si atom at the center bonded to four oxygen atoms at the corners.

of tetrahedrons joined at their corners. Each tetrahedron contains a Si atom at the center bonded to the four oxygen atoms at the corners (see Fig. 3.2). For SiO_2 implanted with Si atoms, thermal annealing causes the precipitation of Si crystals and the return of the matrix to stoichiometric SiO_2. After the phase separation Si atoms in both the matrix and the precipitates satisfy their tetrahedral coordination (except for the atoms at the precipitate/matrix interfaces), lowering the free energy of the system. For SiO_2 implanted with Ge atoms, there are two possible ways to lower the free energy of the system: (1) precipitation of Ge nanocrystals and the return of the SiO_2 matrix to stoichiometry; (2) precipitation of Si nanocrystals and the formation of $Si_{1-x}Ge_xO_2$ (the Ge atoms displaces Si atoms in the some of the tetrahedrons of the silica). As it turns out, (1) occurs because silicon oxide is more stable than germanium oxide, as discussed below.

Paine *et al.* [18] and Liu *et al.* [19] have shown that, during thermal annealing, Ge nanocrystals precipitate in $Si_{1-x}Ge_xO_2$ (formed by oxidation of $Si_{1-x}Ge_x$ alloy). Nucleation of Ge crystals can occur in the vicinity of the Si substrate, at about 800 °C, by

$$GeO_2 + Si = SiO_2 + Ge, \tag{3.1}$$

with a free energy of reaction $\Delta G = -82$ kcal/mol [18], or in a hydrogen ambient, at 700 °C, by

$$GeO_2 + 2H_2 = Ge + 2H_2O, \quad (3.2)$$

with a free energy of reaction $\Delta G = -2.3$ kcal/mol [19]. Even though the reaction in Eq. 3.1 has a lower energy of formation than the reaction in Eq. 3.2, its rate is limited by the slow diffusion rate of Si atoms in silica. It should be noted that, unlike the two reactions described above, in which addition of either Si or H_2 is required for Ge precipitation, in the current experiment neither is required because the samples contained SiO_2 rather than $Si_{1-x}Ge_xO_2$.

3.2.2 Ostwald ripening

In the current experiment, even after most of the excess Si or Ge atoms have precipitated out of the SiO_2 matrices, there is still a considerable amount of energy stored in the nanocrystal/matrix interface. As a result, annealing of samples containing Ge nanocrystals at higher than 600 °C produced Ostwald ripening—coarsening—of the nanocrystals, in which larger crystals grew at the expense of smaller crystals. During coarsening the number of particles decreases while the average particle size increases, reducing the total surface area of the particles. The classical mean-field treatments of coarsening by Lifshitz and Slyozov [23] and Wagner [24] (LSW) predict that $\bar{r} \propto t^{1/3}$ for diffusion-controlled coarsening, while the treatment by Wagner [24] also predict that $\bar{r} \propto t^{1/2}$ for interface-controlled coarsening, where $\bar{r}$ is the average particle radius. As will be shown in the next section, the results of current experiment differ from both predictions. Possibile causes for the discrepancy are discussed in Sec. 3.4.

3.3 Experiment and results

Thermally-grown silicon dioxide films 90 nm thick, on top of Si wafer, were implanted with 70 keV $^{74}Ge^+$ ions or 50 keV $^{28}Si^+$ ions at a dose of 0.6, 1.6, or 3.7 $\times 10^{16}$ /cm^2. The ion energies were chosen to place the peak of the concentration profiles approx-

imately in the center of the films. The SiO_2 film thickness and the implantation doses stated above were obtained from the Rutherford backscattering spectra of the Ge-implanted samples. The implanted samples were annealed for 2.5–80 min at 400–1200 °C. The annealings were performed under high vacuum, at pressure of 1–3 $\times 10^{-6}$ Torr. Plan-view and cross-sectional TEM were performed to obtain nanocrystal concentration and size distribution, as well as nanocrystal structure. The TEM samples were prepared by cutting the wafers into 2 mm by 2 mm squares and then chemically etching a selected area (by covering other areas with wax) of the Si substrate using HF:HNO_3 at ratios of 1:1 to 1:40. The electron microscope was a 300 keV Phillips 430 with a point-to-point resolution of 2.4 Å. Both bright field and high-resolution TEM images were acquired. Rutherford backscattering spectrometry using 2.0 MeV $^4He^{++}$ was performed on Ge-implanted samples before and after anneal to study the diffusion of Ge atoms inside the SiO_2 matrix. The surface normal of the sample was tilted 60° with respect to the direction of the ion beam in order to increase the depth resolution of the Ge atoms.

3.3.1 Ge-implanted samples

For the mid-dose and high-dose Ge-implanted samples, nucleation of nanocrystals occurred during implantation. Figure 3.3(a) shows a high resolution transmission electron micrograph of a sample after it was implanted with 1.6×10^{16} Ge/cm^2. Germanium nanocrystals 1 to 2 nm in size, easily identifiable as the dark spots (due to a higher electron density than the SiO_2 matrix), are visible in the micrograph. This is somewhat unexpected since reports of Ge nanocrystal syntheses via cosputtering of Ge and SiO_2 [11]–[14] or oxidation of $Si_{1-x}Ge_x$ alloys [18, 19] indicate that thermal annealing was required for nanocrystal precipitation. However, formation of Ge nanocrystals without annealing has been reported for SiO_2-GeO_2 glass implanted with 1.5 MeV protons to a dose of 1×10^{18} /cm^2 [25]. For the low-dose Ge-implanted samples, no crystals were found after implantation or even after a 1000 °C anneal for 40 min.

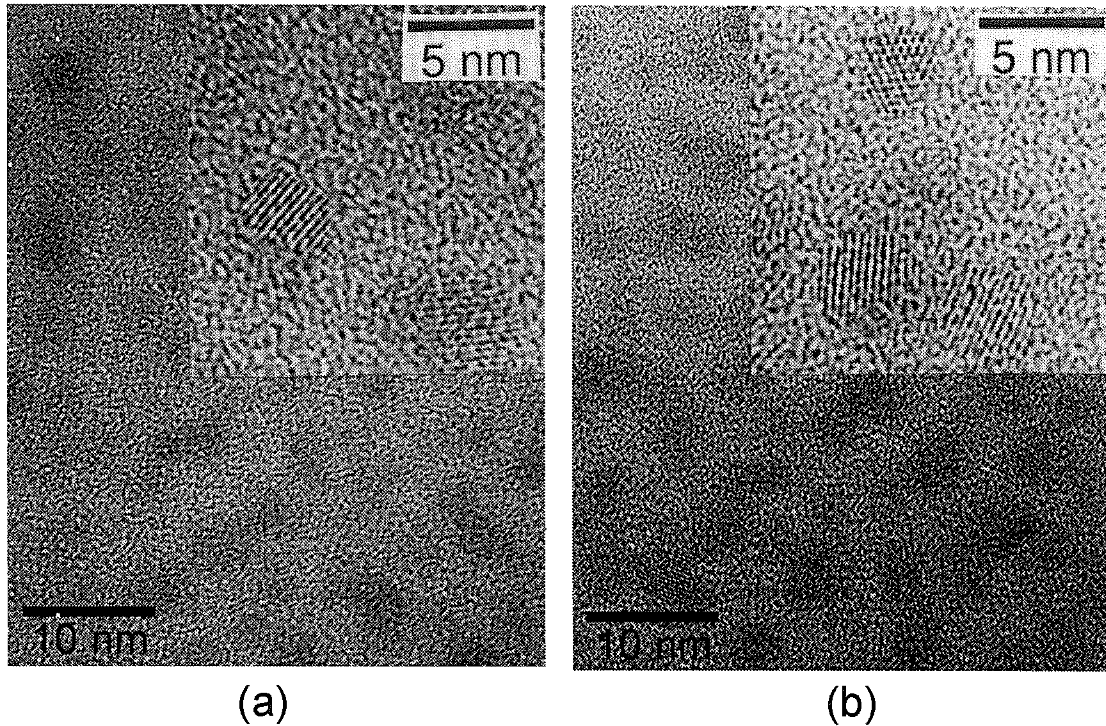

Figure 3.3: High-resolution transmission electron micrographs of Ge nanocrystals in 90 nm-thick SiO_2 implanted with 1.6×10^{16} /cm^2 70 keV $^{74}Ge^+$: (a) as-implanted, and (b) after a 40 min anneal at 600 °C. The dark spots (due to the higher electron density of Ge nanocrystals relative to the SiO_2 matrices) are the Ge nanocrystals; their lattice fringes can be seen in the insets. These images show that nucleation of nanocrystals occurred during implantation and that nanocrystal concentration and size were unchanged by the 600 °C anneal.

For the mid-dose or high-dose Ge-implanted samples, anneals at temperatures lower than 600 °C produced no change in nanocrystal size or concentration, while anneals at temperatures higher than 600 °C resulted in increased size but decreased concentration—a sign of ripening. Figure 3.3(b) shows a high resolution transmission electron micrograph of a 1.6×10^{16} Ge/cm^2-implanted sample after a 600 °C, 40 min anneal. It shows that this sample exhibited the same nanocrystal concentration and size as the sample shown in Fig. 3.3(a), which was implanted with the same Ge dose but was unannealed. Thus, no additional nucleation or growth took place during the 600 °C anneal. Figures 3.4(a)–(d) show bright field transmission electron micrographs of 1.6×10^{16} Ge/cm^2-implanted samples annealed for 40 min at 600 °C, 800 °C, 1000 °C or 1200 °C. The micrographs were acquired at 122,000X magnification, and

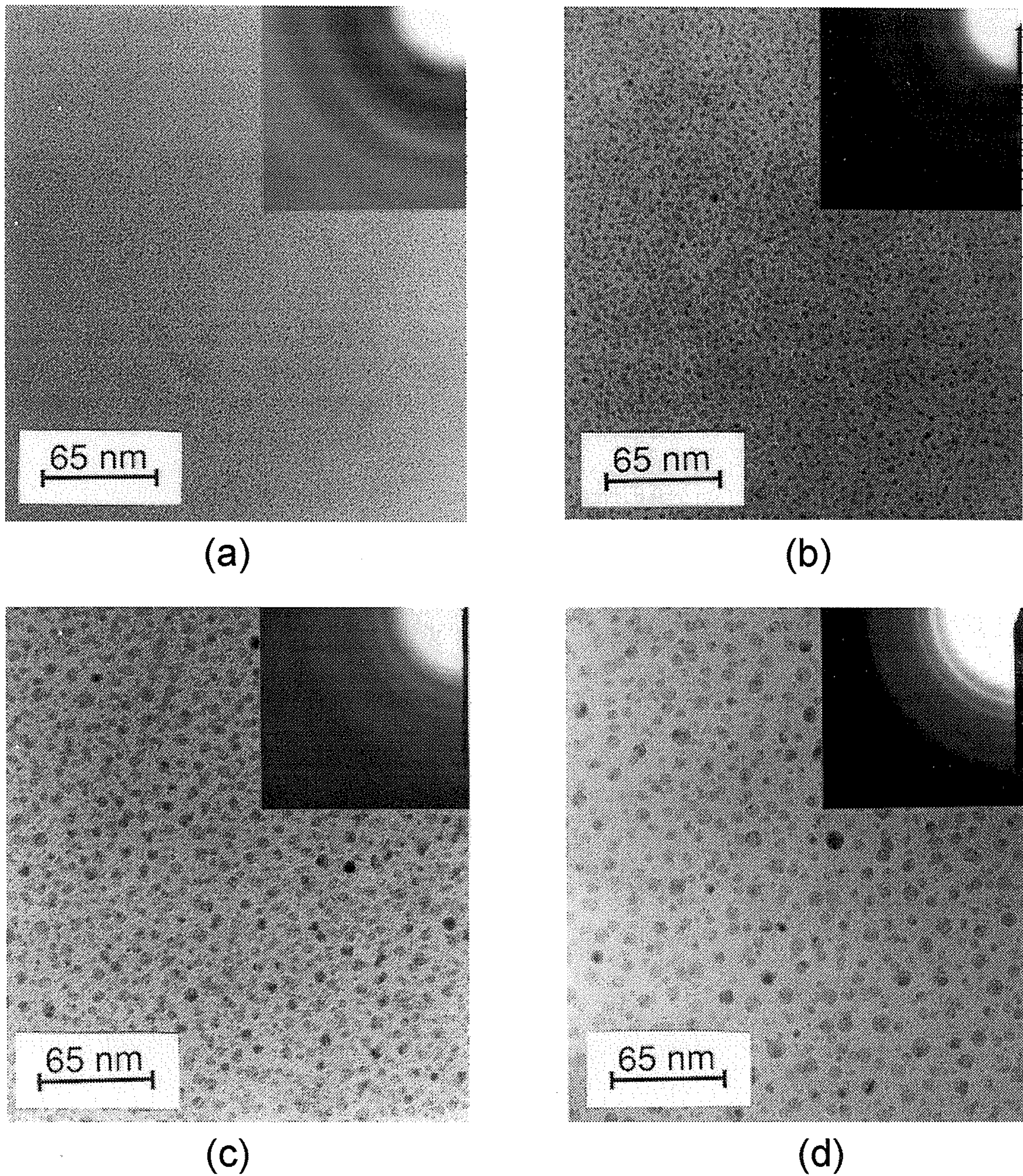

Figure 3.4: Bright field transmission electron micrographs of Ge nanocrystals in SiO_2 thin films implanted with 1.6×10^{16} Ge/cm^2, and then annealed for 40 min at: (a) 600 °C, (b) 800 °C, (c) 1000 °C, and (d) 1200 °C. The average size increased—while the concentration decreased—with increasing annealing temperature.

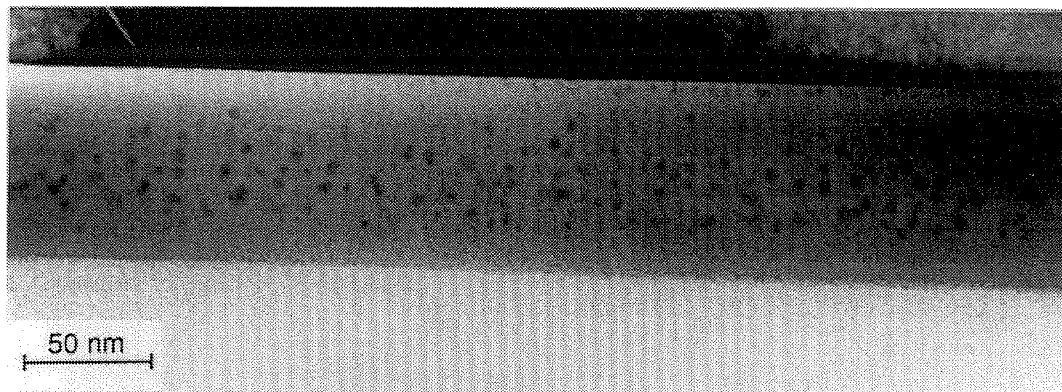

Figure 3.5: Cross-sectional electron micrograph of a sample implanted with 1.6×10^{16} Ge/cm^2 and then annealed at 800 °C for 40 min. The existence of the nanocrystals was confined to the middle region of the silica film, due to the fact that the implantation profile peaked at the middle of the film, as evidenced by the RBS data shown later in this section.

the minimum resolvable crystal size at this magnification is about 1 nm. It has been reported that for Ge crystals smaller than 4 nm the favored crystal structure is no longer diamond cubic [26]. In the present work however, transmission electron diffraction and high resolution TEM of samples annealed at 600 °C, in which all of the nanocrystals were less than 4 nm in size, revealed only diamond-cubic structure. In addition, cross-sectional electron microscopy revealed that the existence of the nanocrystals was confined to the middle region of the silica films, and that the top and bottom 20 nm of the films contained virtually no nanocrystals, as shown in Fig. 3.5.

Figure 3.6 shows the nanocrystal size distributions counted from the bright field transmission electron micrographs of the mid-dose implanted samples. Each size distribution was obtained from about 1000 nanocrystals. Based on these data, the average diameter, $\bar{d}$, the standard deviation of the diameter, σ, the concentration, c_0, the inter-particle distance, l, and the total number of Ge atoms contained in the nanocrystals, c_1, at various annealing temperatures were calculated and are listed in Table 3.1. The values of c_1 were calculated from the size distributions by assuming that the nanocrystals were perfect spheres with the same atomic concentration as bulk Ge. These values show that even after the 600 °C or the 800 °C anneal, only a

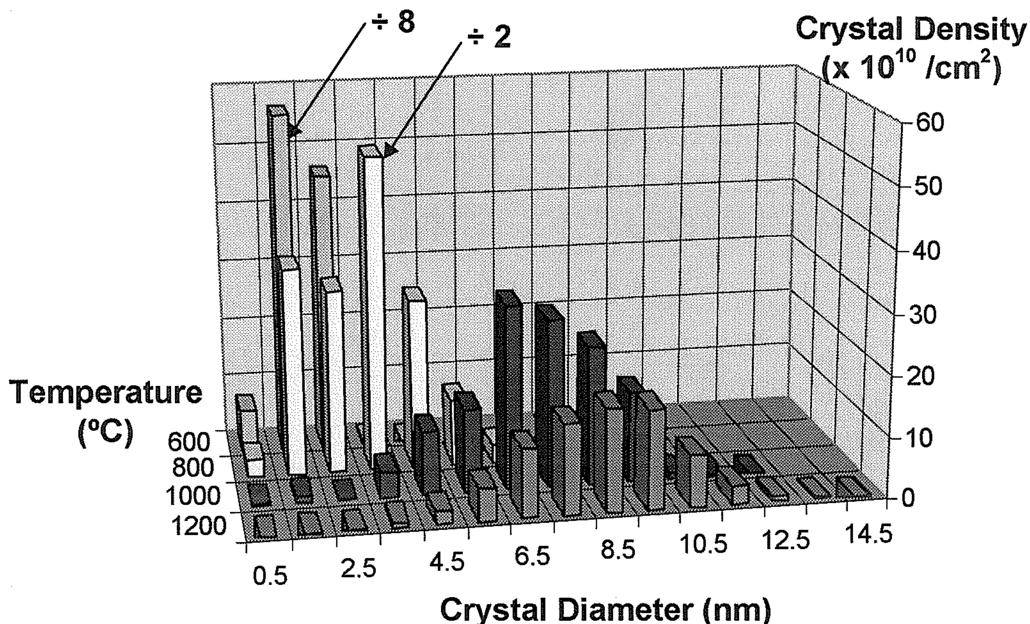

Figure 3.6: Germanium nanocrystal size distributions in SiO_2 films implanted with 1.6×10^{16} Ge/cm^2 and then annealed for 40 min at various temperatures. Data is based on bright field transmission electron micrographs.

small fraction of the 1.6×10^{16} /cm^2 implanted atoms had precipitated into nanocrystals. In addition, Table 3.1 shows that the average crystal size increased while the crystal concentration decreased with increasing annealing temperature. Since unannealed samples contained nanocrystals of similar size and concentration as the 600 °C annealed samples, this shows that coarsening had taken place during anneals at temperatures higher than 600 °C.

Temp. (°C)	$\bar{d}$ (nm)	σ (nm)	c_0 ($\times 10^{11}$/cm^2)	l (nm)	c_1 ($\times 10^{16}$ at./cm^2)
600	1.9	0.5	87.9	8.29	0.17
800	3.3	1.3	32.5	11.5	0.39
1000	6.9	1.6	12.6	15.8	1.2
1200	8.2	1.8	7.99	18.4	1.2

Table 3.1: Table of the average nanocrystal diameter, $\bar{d}$, the standard deviation of nanocrystal diameter, σ, the nanocrystal concentration, c_0, the inter-crystal distance, l, and the concentration of Ge atoms contained in the nanocrystals, c_1, for the size distributions shown in Fig. 3.6. The values of c_1 were calculated from the size distributions by assuming that the nanocrystals were perfect spheres with the same atomic concentration as bulk Ge.

In order to study the coarsening kinetics of the nanocrystals and compare them to those predicted by LSW [23] and Wagner [24], isothermal anneal of mid-dose Ge-implanted samples were performed at 1000 °C for various durations. Figures 3.7(a)–(d) show bright field electron micrographs of 1.6×10^{16} Ge/cm^2-implanted samples annealed at 1000 °C for 2.5 min, 10 min, 40 min, or 80 min. It is evident that neither the average size nor the concentration changed with increasing annealing time. Results were same for isothermal anneals at 800 °C and 1200 °C. Anneals shorter than 2.5 min were not attempted because the samples required about 1 or 2 min to reach the furnace temperature. Figure 3.8 shows a plot of the calculated average radius, $\bar{r}$, at various annealing times, as well the time dependence of $\bar{r}$ predicted by LSW and by Wagner. It shows that data does not agree with that predicted for either diffusion-controlled ripening or interface-controlled ripening, and that the disagreement is much larger than the experimental uncertainty. In addition, it was observed that samples subjected to a two-step annealing, first at a lower temperature and then at a higher temperature, showed the same nanocrystal size and concentration as a sample annealed only at the higher temperature. For example, a sample first annealed at 800 °C for 40 min then at 1000 °C for 10 min was virtually indistinguishable from a sample annealed only at 1000 °C for 10 min. Same result was obtained for a sample annealed for 40 min at 600 °C and then for 10 min at 1000 °C. Taken together, the above data suggest that some factor(s), not considered by LSW or Wagner, made the system stable against coarsening after the precipitates reached a certain temperature-dependent size. This is not entirely unexpected: evidence of resistance against coarsening has also been found in precipitation of CdS nanocrystals in glass [27]. However, this is the first report of the time dependence—not merely the temperature dependence—of Ge nanocrystal precipitation in silica.

The diffusion coefficient of Ge atoms in amorphous silica at various temperatures was estimated from the data in Table 3.1, and support the notion that the coarsening was not diffusion-limited. They were calculated by assuming that (a) the nanocrystal size distribution of unannealed samples was the same as that of the 600 °C-annealed samples (as Figs. 3.3(a) and (b) suggest), and (b) nanocrystals in the 800 °C, 1000

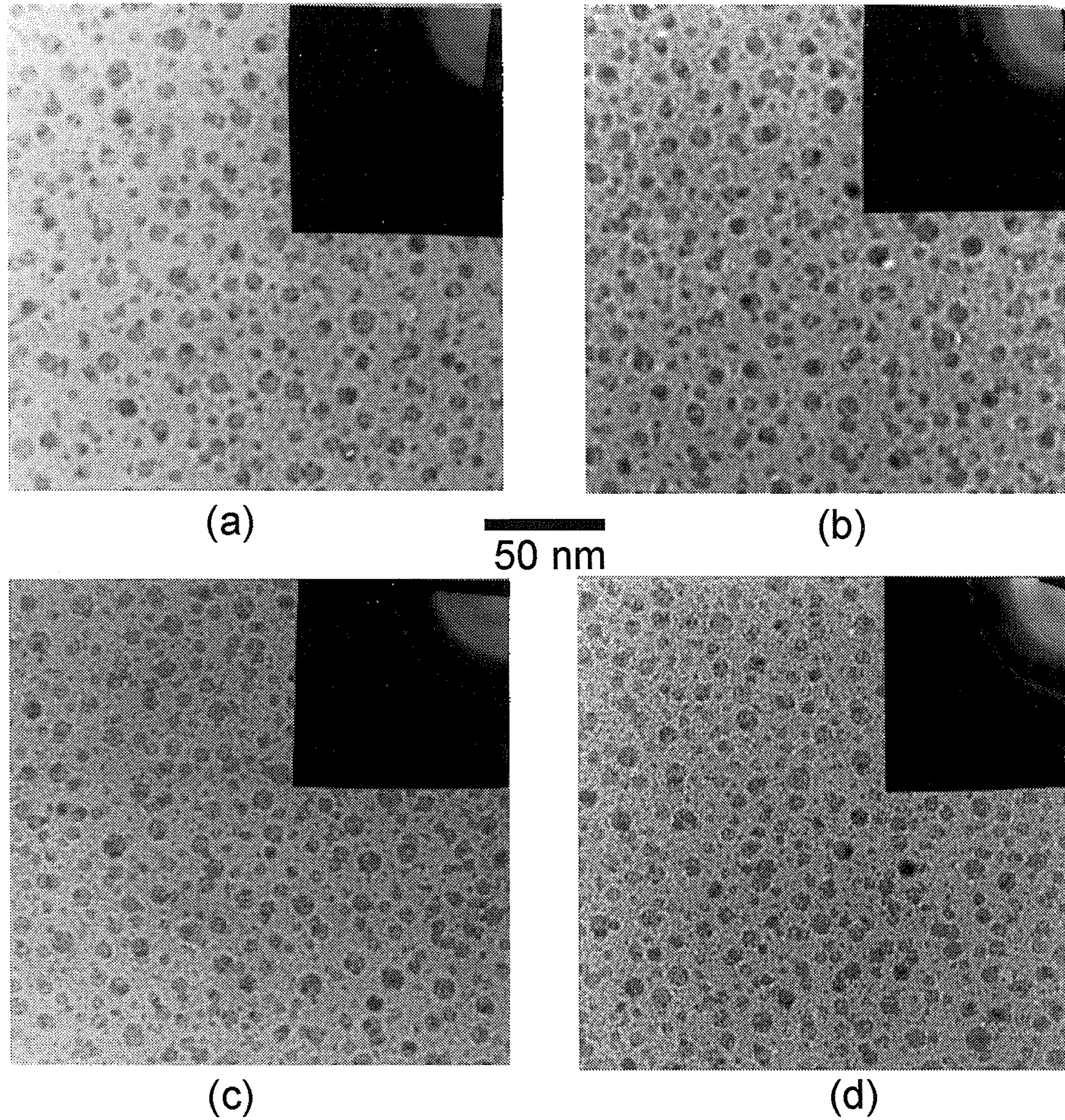

Figure 3.7: Bright field transmission electron micrographs of 1.6×10^{16} Ge/cm^2-implanted samples annealed at 1000 °C for: (a) 2.5 min, (b) 10 min, (c) 40 min, and (d) 80 min. The nanocrystal size and concentration did not change with increasing annealing time.

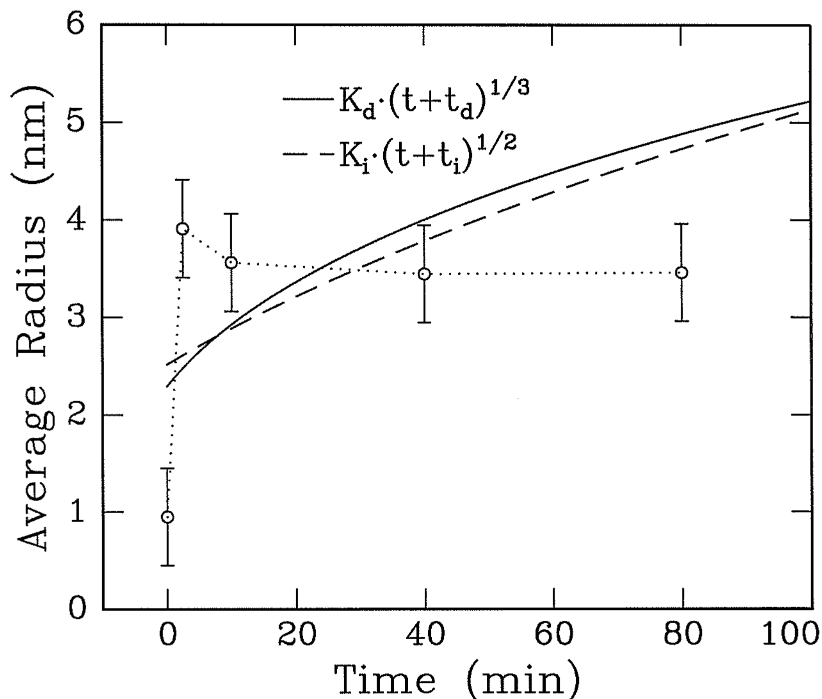

Figure 3.8: A plot of the average nanocrystal radius $\bar{r}$ vs. isothermal annealing time for 1.6×10^{16} Ge/cm^2-implanted samples annealed at 1000 °C. The solid line is a fit of the time dependence of $\bar{r}$ for diffusion-controlled coarsening predicted by LSW [23], and the dashed line is a fit of the time dependence of $\bar{r}$ for interface-controlled coarsening predicted by Wagner [24]. The fitting parameters are $K_d, t_d, K_i,$ and t_i.

°C, and 1200 °C annealed samples grew by adsorbing all of the Ge atoms within the diffusion length $\sqrt{Dt}$, where D is the diffusion coefficient and t is the annealing time. The total number of Ge atoms contained in the nanocrystals in the 600 °C annealed samples was 0.17×10^{16} at./cm^2, so the average concentration of Ge atoms in the SiO_2 matrices, c_m, was 1.6×10^{16} at./cm^2 minus 0.17×10^{16} at./cm^2, divided by the SiO_2 film thickness (90 nm), or 1.59×10^{21} at./cm^3. The number of atoms adsorbed

Temp (°C)	D (cm^2/sec)	$\sqrt{Dt}$
800	1×10^{-15}	19 nm
1000	7×10^{-15}	42 nm
1200	1×10^{-14}	49 nm

Table 3.2: Table of the minimum diffusion coefficient of Ge atoms in amorphous silica at various temperatures. The diffusion length, $\sqrt{Dt}$, was calculated for $t = 40$ min.

by an average-sized nanocrystal during an anneal is given by

$$\frac{4}{3}\pi\bar{r}_T^3 c_{Ge} - \frac{4}{3}\pi\bar{r}_{600}^3 c_{Ge} = \frac{4}{3}\pi\left(\sqrt{Dt}\right)^3 c_m, \tag{3.3}$$

where $\bar{r}_{600}$ (0.85 nm) and $\bar{r}_T$ are the average nanocrystal radius in samples annealed at 600 °C and temperature T, respectively, and c_{Ge} is the atomic concentration of bulk Ge (4.42×10^{22} at./cm^3). From the above equation a diffusion length of 4.66 nm, 10.4 nm, and 12.4 nm was obtained for samples annealed at 800 °C, 1000 °C, and 1200 °C, respectively. Since the shortest annealing time of 2.5 min produced the same nanocrystal size and concentration as an annealing time of 40 min, at temperatures of 800 °C, 1000 °C, and 1200 °C, t in Eq. 3.3 was taken to be 2.5 min. The resulting estimated minimum diffusion coefficients are shown in Table 3.2. To the author's knowledge, these are the first calculated values of D for Ge in vitreous SiO_2. This table shows that the diffusion length of a 40 min, 1000 °C anneal is at least 42 nm, which is much larger than the distance between the nanocrystals, 12.6 nm, as shown in Table 3.1. Thus, the coarsening of nanocrystals at 1000 °C could not have been diffusion-limited, unless D was time-dependent and decreased considerably after 2.5 min. This is unlikely, since a minimum diffusion length of 45 nm for a 1000 °C, 40 min anneal was independently obtained from Rutherford backscattering spectrometry, as shown later in this section.

High-dose Ge-implanted samples annealed at the same temperatures as mid-dose Ge-implanted samples showed further evidence that Ge nanocrystal precipitation was not diffusion-controlled. Figures 3.9(a) and (b) show bright field transmission electron micrographs of samples implanted with 1.6×10^{16} Ge/cm^2 and 3.6×10^{16} Ge/cm^2, respectively, and then annealed at 1000 °C for 40 min. These figures show that the increase in the implantation dose increased nanocrystal concentration by a factor two but did not increase the nanocrystal size. If the coarsening had been diffusion-controlled, then the distance between the nanocrystals in the high-dose and mid-dose implanted samples would have been about the same; that is, Fig. 3.9(a) and (b) would have shown approximately the same nanocrystal concentration. Again, the

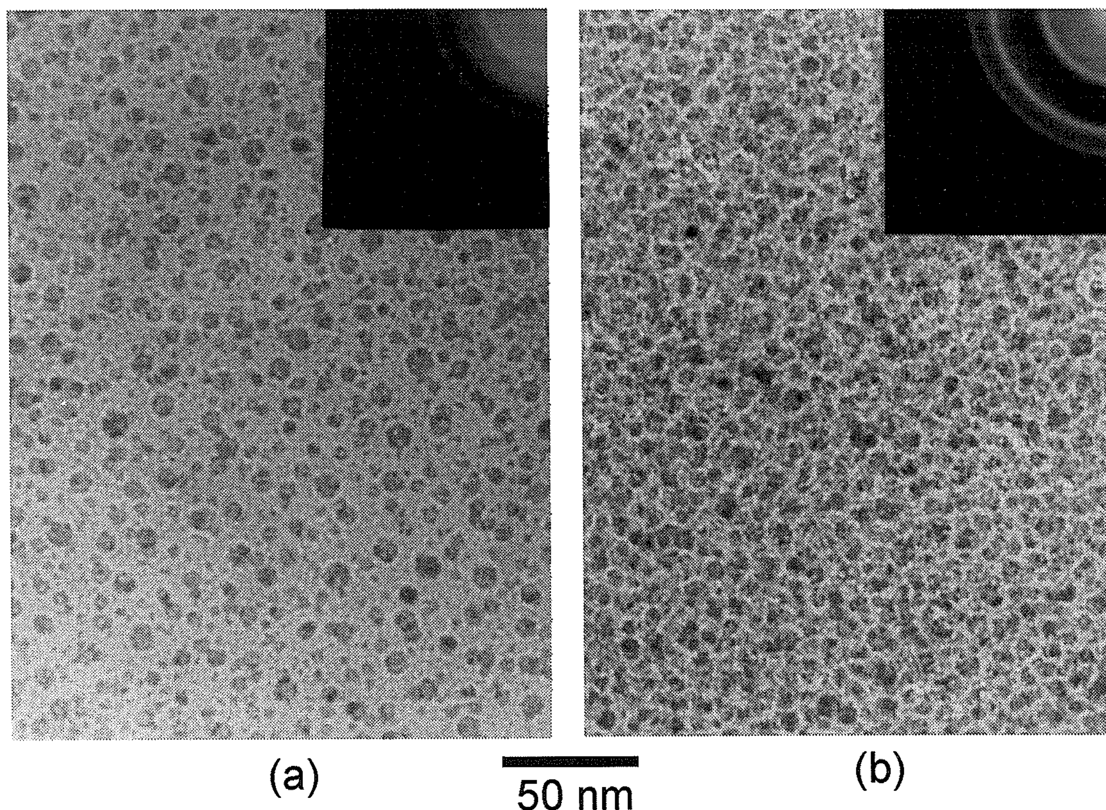

Figure 3.9: In (a), bright field transmission electron micrograph of samples implanted with 1.6×10^{16} Ge/cm^2, then annealed at 1000 °C for 40 min. In (b), same preparation as (a) except the sample was implanted with 3.6×10^{16} Ge/cm^2.

above data suggest that some factor(s) made the system stable against ripening after the precipitates had reached a certain temperature-dependent size.

In order to gain further insight into the diffusion kinetics of Ge atoms, their concentration profile in the silica matrices at various temperatures were obtained by RBS. Figure 3.10 shows Rutherford backscattering spectrum of a sample after it was implanted with 1.6×10^{16} Ge/cm^2. The Ge peak appears quite symmetrical and is well separated from the Si peak of the SiO_2 film, unlike the O peak. Figures 3.11(a)–(d) show Rutherford backscattering spectra of samples implanted with either 1.6×10^{16} Ge/cm^2 or 3.6×10^{16} Ge/cm^2, and then annealed at either 800 °C for 50 min or 1000 °C for 40 min. Unlike the as-implanted samples, which had a single Ge peak, the annealed mid-dose implanted samples showed two overlapping Ge peaks. On the other hand, in the annealed high-dose implanted samples, there was only one

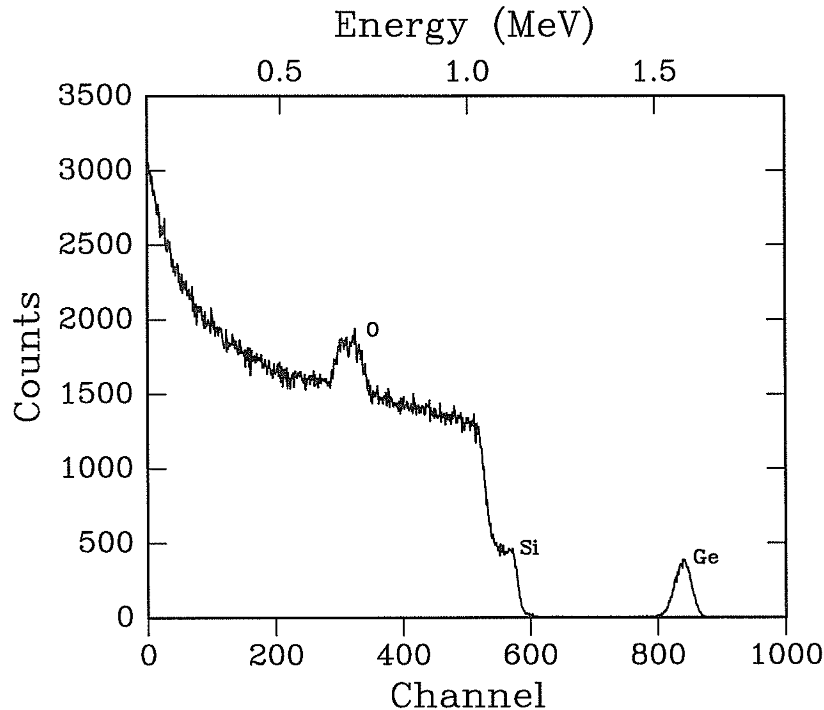

Figure 3.10: Rutherford backscattering spectrum of a sample implanted with 2×10^{16} Ge/cm^2.

asymmetrical Ge peak with a small tail. The reason for the appearance of the second peak in the mid-dose implanted samples and of the tail in the high-dose implanted samples was the diffusion of Ge atoms into the Si substrate, as discussed below.

From the Rutherford backscattering spectra, Ge atom concentrations as a function of film depth were obtained for various implantation doses and annealing temperatures. Figure 3.12 shows concentration vs. depth for the mid-dose implanted samples, before anneal and after a 800 °C or 1000 °C anneal. This figure shows that the unannealed sample exhibited a single peak at 45 nm depth—the center of the silica film, whereas the samples annealed at 800 °C or 1000 °C exhibited two peaks, one at 45 nm depth and the other at 90 nm depth. Since the thickness of the silica films was 90 nm, the areas of the peaks at 90 nm depth correspond to the amount of Ge atoms which had diffused into the Si substrate. Figure 3.12 shows that the concentration of Ge atoms in the top and bottom 20 nm of the film was less than half of the concentration at the center of the film, which is consistent with the cross-sectional

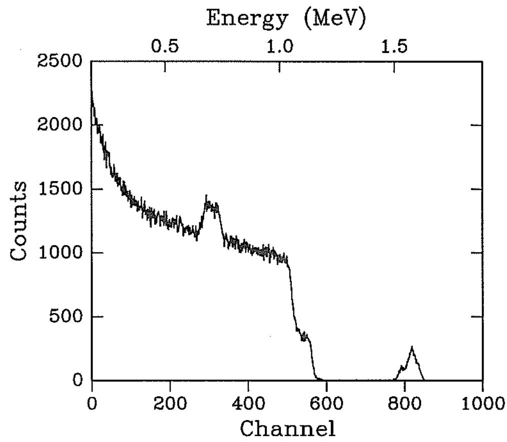

(a)

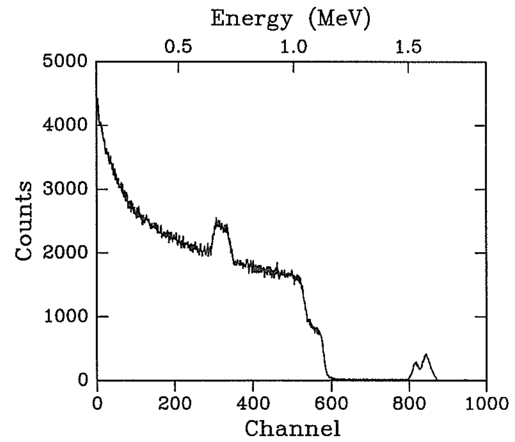

(b)

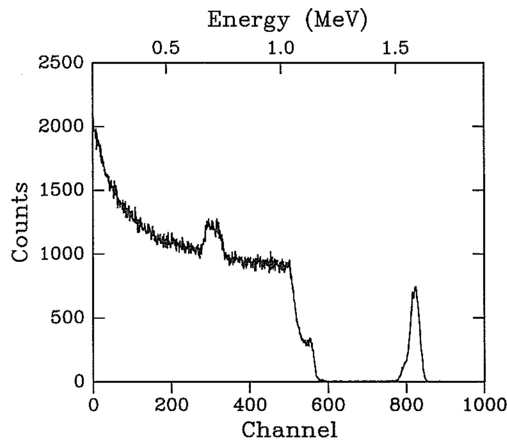

(c)

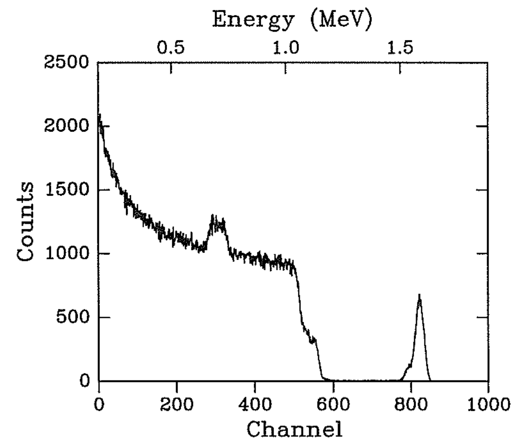

(d)

Figure 3.11: In (a) and (b), Rutherford backscattering spectra of samples implanted with 1.6×10^{16} Ge/cm^2, then annealed at 800 °C for 50 min and 1000 °C for 40 min, respectively. In (c) and (d), the same annealing treatment as in (a) and (b), respectively, but implanted with 3.6×10^{16} Ge/cm^2.

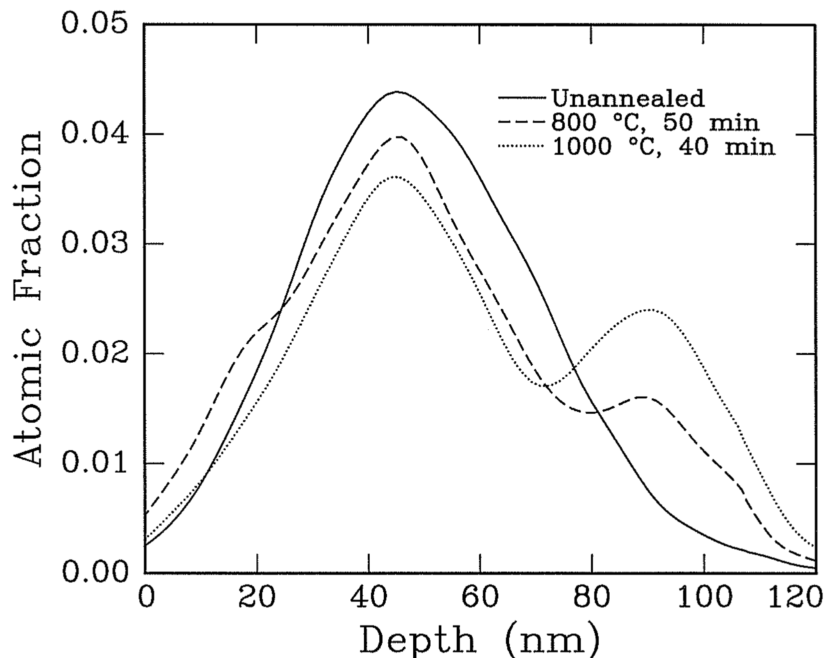

Figure 3.12: Concentration of Ge atoms as a function of film depth at various annealing temperatures for 1.6×10^{16} Ge/cm^2-implanted samples. Instrumental broadening of the spectra due to the detector resolution was approximately 20 nm.

transmission electron micrograph shown in Fig. 3.5, where the top and bottom 20 nm of the silica film contained no nanocrystals. Since the concentration of Ge atoms at 20 nm depth was 40% of the peak concentration (at 45 nm depth) for unannealed samples, the above statement implies that a dose of 40% of 1.6×10^{16} at./cm^2, or 0.64×10^{16} at./cm^2, was required for nucleation at the center of the silica films during implantation, in agreement with the observation that no nanocrystals were found in the 0.6×10^{16} /cm^2-implanted samples. It is worth noting that the area under curve equals the implantation dose, 1.6×10^{16} Ge/cm^2, for all three curves shown in Fig. 3.12. This indicates that there was no loss of Ge atoms due to out-diffusion during the 800 °C and 1000 °C anneals. In addition, Fig. 3.12 reveals that the total number of Ge atoms remained in the silica film (the area of the peak at 45 nm depth) after the 1000 °C, 40 min anneal was $(1.2 \pm 0.2) \times 10^{16}$ /cm^2, which is the same as the number of Ge atoms contained in the nanocrystals, as shown in Table 3.1. This implies that after the 1000 °C anneal, all of the Ge atoms had diffused into either

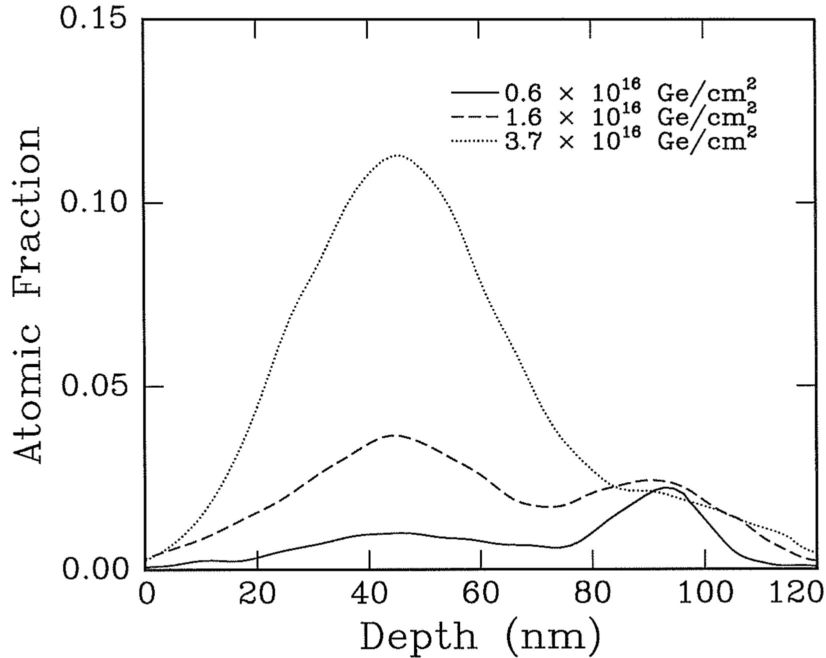

Figure 3.13: Concentration of Ge atoms as a function of film depth for samples implanted with various doses and then annealed for 40 min at 1000 °C.

the substrate or the nanocrystals. The same conclusion holds for the 1200 °C anneal. In contrast, Fig. 3.12 shows that the number of Ge atoms remained in the silica film after the 800 °C, 50 min anneal was $(1.3 \pm 0.2) \times 10^{16}$ /cm^2, which is larger than the 0.39×10^{16} /cm^2 contained in the nanocrystals, as shown in Table 3.1. Therefore, the number of Ge atoms dispersed in the matrix was $(0.91 \pm 0.2) \times 10^{16}$ /cm^2. The same analysis yields $(1.4 \pm 0.2) \times 10^{16}$ /cm^2 for the sample annealed at 600 °C for 40 min.

Figure 3.13 shows Ge concentration vs. depth for low-dose, mid-dose, and high-dose implanted samples annealed for 40 min at 1000 °C. It shows that the fraction of Ge atoms diffused into the substrate decreased with increasing implantation dose; for the low-dose implanted sample, about half of the Ge atoms diffused into the substrate during the anneal, whereas for the high-dose implanted sample, only about one-tenth of the Ge atoms diffused into the substrate during the anneal. Assuming that the fraction of implanted atoms diffused into the substrate equal those within the diffusion length, $\sqrt{Dt}$, of the substrate, a minimum diffusion length of 45 nm is calculated for the low-dose implanted sample, which is in agreement with the 42 nm listed in Table

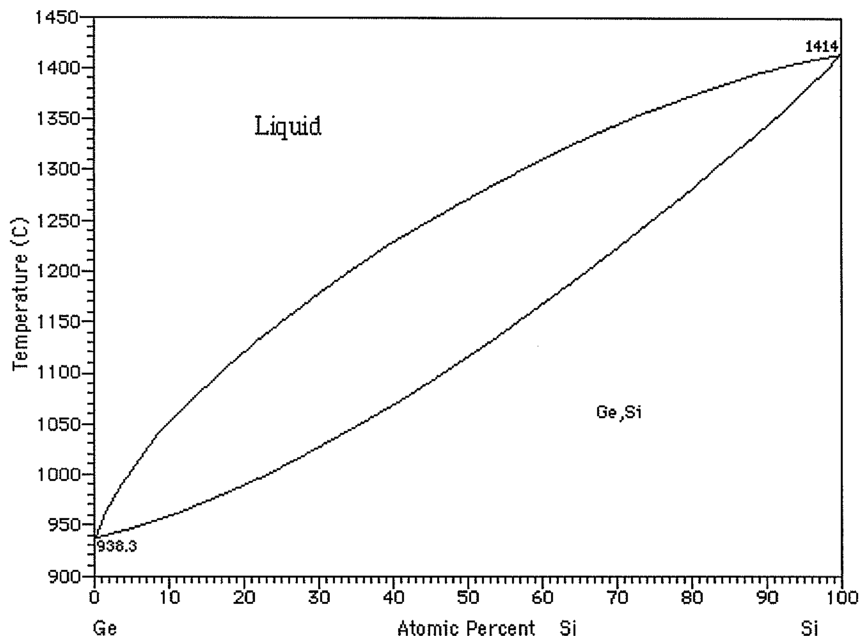

Figure 3.14: Germanium-silicon binary phase diagram.

3.2, calculated for mid-dose implanted samples using the nanocrystal concentration and sizes obtained with TEM. The close agreement between the two numbers is perhaps fortuitous, considering the widely different experimental techniques used to obtain them. Note that the calculation of a minimum diffusion length from Fig. 3.13 is valid only for samples which contained no nanocrystals (e.g., the low-dose implanted samples), because they acted as sinks for the Ge atoms, preventing those atoms from diffusing into the substrate, as explained below.

Since precipitation of Ge nanocrystals reduces the free energy of the system, the nanocrystals are sites of lower chemical potential—relative to the matrix—for the Ge atoms. However, these sites are metastable: during coarsening a nanocrystal might grow initially but later dissolve. On the other hand, Ge-Si phase diagram (shown in Fig. 3.14) indicates that, at temperatures less than 1200 °C, $Si_{1-x}Ge_x$ alloy is solid and stable with respect to phase transition and phase separation for $x \leq 0.35$. As Figure 3.13 shows, $x < 0.05$ for the low-dose, mid-dose, and high-dose implanted samples annealed at 1000 °C. (Note that the actual concentrations of Ge atoms in the Si substrates were slightly higher than indicated in Figs. 3.12 and 3.13, because they

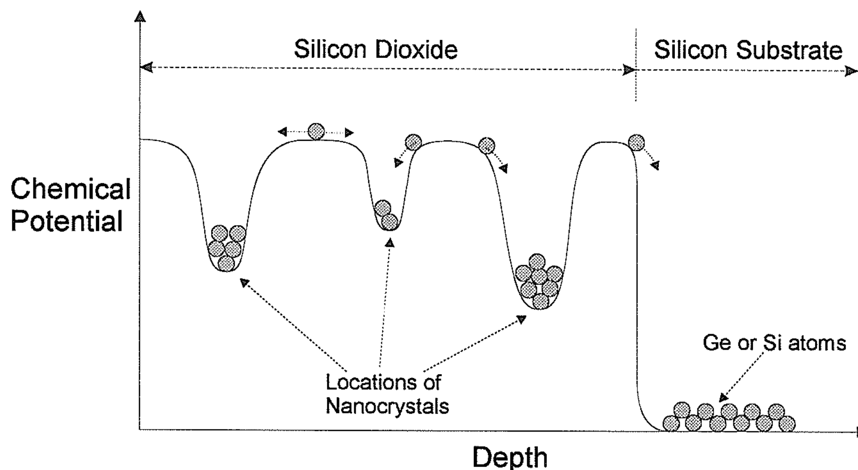

Figure 3.15: Schematic of the chemical potential of Ge and Si atoms as a function of depth.

do not take into account the fact that the atomic concentration of silica—6.6×10^{22} at./cm^2, is higher than that of Si—5.0×10^{22} at./cm^2.) Consequently, the Si substrate is a stable sink for the Ge atoms. A schematic of the chemical potential of Ge atoms as a function of depth, summarizing the above discussion, is shown in Fig. 3.15. As noted in the figure, the Ge nanocrystals act as local sinks for the Ge atoms; consequently, the more nanocrystals a sample contains, the larger the fraction of Ge atoms will be retained in the silica film, in agreement with the results shown in Fig. 3.13. This picture of chemical potential is also valid for Si atoms in the Si-implanted samples.

3.3.2 Si-implanted samples

Unlike the Ge-implanted samples, the Si-implanted samples contained no nanocrystals prior to thermal annealing. In fact, Si nanocrystals were observed only in mid-dose and high-dose implanted samples after they were annealed at 1000 °C. Figures 3.16(c) and (d) show high resolution transmission electron micrographs of mid-dose and high-dose Si-implanted samples after a 40 min, 1000 °C anneal. For comparison, samples implanted with the same doses of Ge and then annealed at the same temperature are shown in Figs. 3.16(a) and (b). Silicon nanocrystals about 1 nm and 2 nm in size can be seen in the mid-dose and high-dose Si-implanted sample, respectively. In contrast,

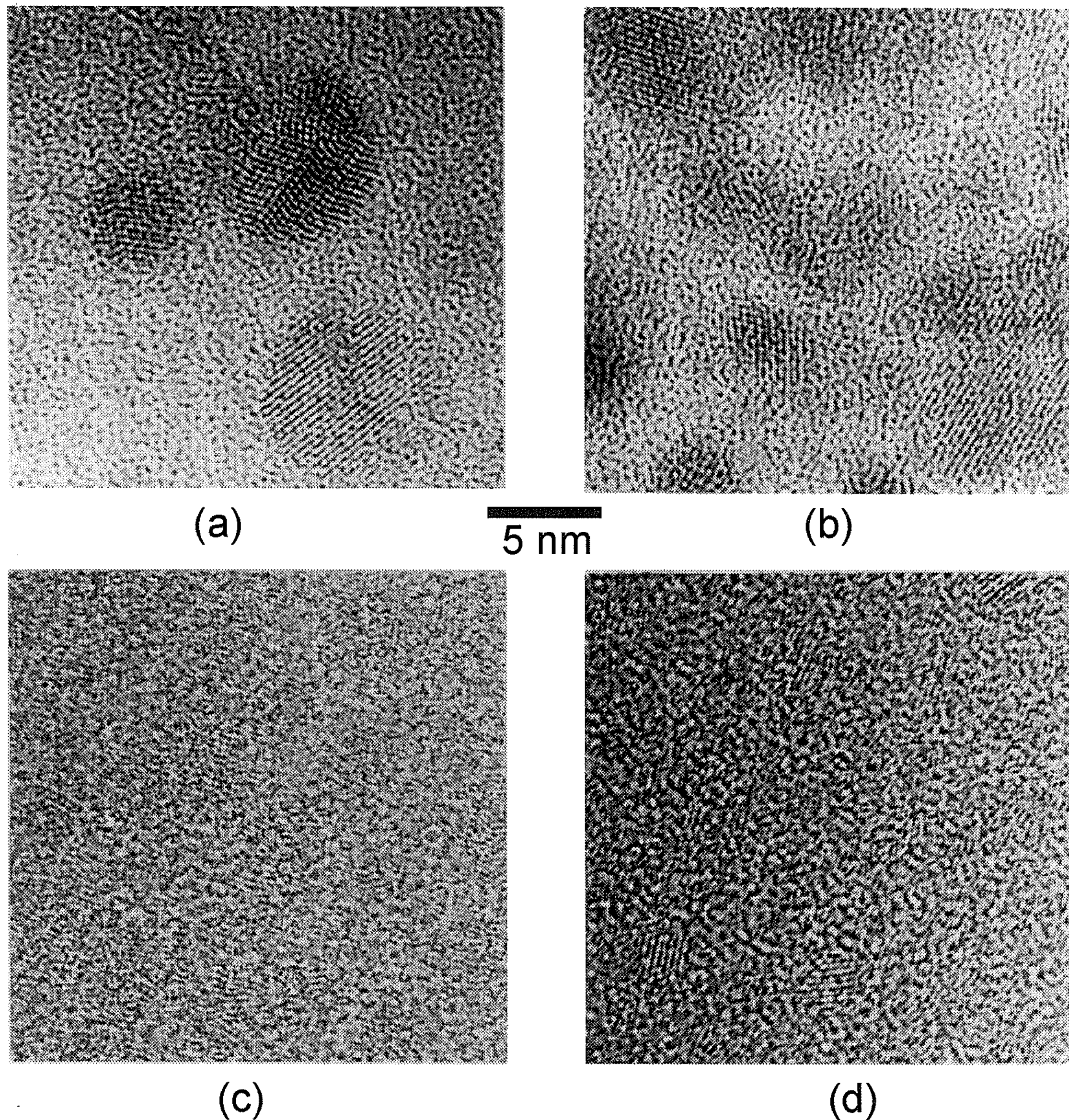

Figure 3.16: In (a) and (b), high resolution transmission electron micrographs of samples implanted with 1.6×10^{16} Ge/cm^2 and 3.6×10^{16} Ge/cm^2, respectively, then annealed at 1000 °C for 40 min. In (c) and (d), same treatment as (a) and (b) except the samples were implanted with Si instead of Ge.

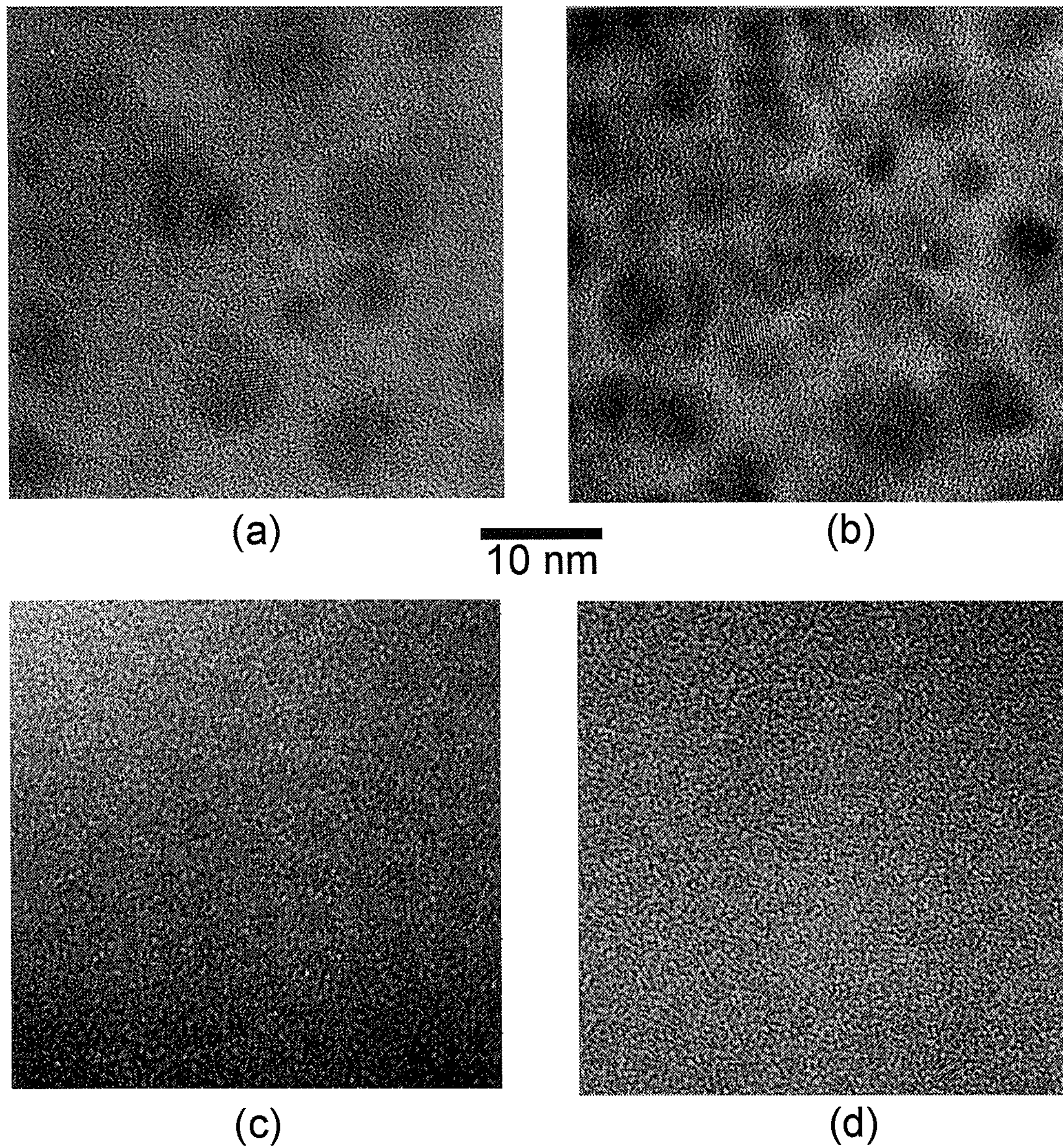

Figure 3.17: High resolution transmission electron micrographs of samples shown in the Fig. 3.16, except at a lower magnification. At this magnification, the small Z-contrast between the Si nanocrystals and the SiO_2 matrix in (c) and (d) is much more apparent.

Ge-implanted samples contained much larger nanocrystals—about 7 nm. Using an equation similar to Eq. 3.3, e.g.,

$$\frac{4}{3}\pi\bar{r}_T^3 c_{Si} = \frac{4}{3}\pi\left(\sqrt{Dt}\right)^3 c_m, \tag{3.4}$$

a diffusion length and diffusion coefficient of 2.9 nm and 3.5×10^{-17} cm^2/sec, respectively, were obtained for the high-dose Si-implanted sample annealed for 40 min at 1000 °C (with $\bar{r}_T$ = 1.2 nm). Note that lost of Si atoms to the substrate was not included in the above equation because the diffusion length turned out to very small. Twinning was observed in the Ge nanocrystals, as shown in Figs. 3.16(a) (and were quite common in dark field images) but was not observed in the Si nanocrystals. Figures 3.17(a)–(d) show the same micrographs as in Fig. 3.16(a)–(d), but at a lower magnification. They illustrate clearly that the Z-contrast between the nanocrystals and the silica matrix is much weaker for Si nanocrystals, which, coupled with the extremely small sizes of the Si nanocrystals, made observation of them very challenging; in fact, the thickness of the SiO_2 films had to be reduced to about 70 nm via dilute HF etching before the nanocrystals could be observed. Finally, Rutherford backscattering spectrometry was not performed on the Si-implanted samples because the implanted $^{28}Si^+$ would have been indistinguishable from Si atoms in the thermally-grown oxide.

3.4 Discussion

3.4.1 Ge nanocrystal nucleation

Nucleation of the Ge nanocrystals in the mid-dose and high-dose implanted samples occurred without thermal annealing, unlike other methods of nanocrystal synthesis such as rf-cosputtering [11]–[14], or reduction of $Si_{1-x}Ge_xO_2$ [18, 19], which required a 600-800 °C anneal. Ion implantation of Ge atoms differs from the aforementioned methods in that, during implantation, the ions can (a) enhance diffusion of Ge atoms, perhaps by creating defects in the SiO_2, and (b) reduce the viscosity of the silica matrix [28]. Since nucleation of the Ge nanocrystals requires the diffusion of Ge

atoms in addition to the strain of the matrix (as the crystals increase in size), both radiation-induced diffusion and softening of the silica matrix must have played a role in the nucleation, although the importance of the latter is unclear.

The lack of nucleation in the low-dose implanted samples was likely due to the insufficient supersaturation of Ge atoms. For nucleation the concentration of Ge atoms must be high enough such that a sufficient number of them are within a diffusion length of each other to form a crystal of the thermodynamically critical size, r^*. In addition, the concentration must be equal to or higher than the equilibrium concentration for a crystal of size r^*. Following Eq. 3.3, the diffusion distance of Ge atoms required to form a nanocrystal of radius r^* is

$$\sqrt{Dt} = r^* \left[\frac{c_{Ge}}{c_n}\right]^{1/3}, \tag{3.5}$$

where c_n is the minimum matrix concentration needed. Thus the critical radius is given by

$$r^* = \sqrt{Dt} \left[\frac{c_n}{c_{Ge}}\right]^{1/3}. \tag{3.6}$$

Using the value of c_n calculated in the previous section, the estimated value of r^* is $0.9 \pm .05$ nm, where $\sqrt{Dt} = 2.8$ nm was calculated by noting that 2 nm nanocrystals nucleated during the mid-dose implantations. The concentration of atoms required to maintain local equilibrium with a Ge crystal of size r^* is given by the Gibbs-Thomson equation:

$$c_r = c_e \exp\left[\frac{2\sigma_s}{c_{Ge} r^* kT}\right], \tag{3.7}$$

where σ_s is the surface energy of the crystal/matrix interface, and c_e is the concentration required to maintain equilibrium with a Ge crystal of infinite size.

3.4.2 Coarsening of Ge nanocrystals

The results of 2.5–80 min isothermal anneals at 800 °C, 1000 °C, or 1200 °C, such as those shown in Fig. 3.8, indicate that coarsening of the nanocrystals stopped in less than 2.5 min, which disagrees with the $\bar{r} \propto t^{1/3}$ prediction of LSW [23], or

the $\bar{r} \propto t^{1/2}$ prediction of Wagner [24]. The current experiment differs from the ideal system studied by the above authors in that: (a) precipitates can interact via their diffusion field because they are *not* separated by infinite distance (the volume fraction of the precipitates is not zero), (b) diffusion coefficient of the solute atoms might decrease precipitously after the irradiation-generated defects are annealed out (as in the case of transient enhanced diffusion of implanted dopant atoms in Si [39]), and (c) precipitates can interact via their elastic strain field because the matrix is solid instead of liquid. Of the three differences listed above, only (c) has been shown to lead to stability against coarsening [29] or even to inverse coarsening [30] (e.g., small particles grow at the expense of large particles) In contrast, theoretical [31]–[36] and experimental [37, 38] studies of systems with non-zero volume fraction of precipitates show that increasing diffusional interaction between precipitates result in altered rate constant K, but still retained the relation $\bar{r} \sim Kt^{1/3}$. Also, transient enhanced diffusion due to irradiation-generated defects cannot explain the resistance against coarsening, since Ge nanocrystal precipitation has been observed in silica not subjected to ion irradiation, such as those obtained by cosputtering of Ge and SiO_2. On the other, the observed increase in average size with annealing temperature is consistent with the idea of stress-affected coarsening, since the the elastic constants of the matrix—hence the strength of the elastic interaction between precipitates—decreases with increasing temperature; above 2000 °C, the viscosity of amorphous silica approaches that of a liquid. In particular, calculations by Johnson [29] have shown that two misfitting spherical precipitates in a matrix with isotropic elastic constants and interfacial energy can exhibit stability against coarsening, provided that the precipitates are *softer* than the matrix *and* they are *larger* than certain critical size; otherwise, the precipitates will coarsen. The first requirement was certainly satisfied in the current experiment, since Ge is liquid at 1000 °C and 1200 °C. In Johnson's treatment, precipitates are assumed have a fixed spherical shape; however, Su and Voorhees [30] have shown that relaxation of this morphological restriction results in non-spherical shapes, with the consequence that two precipitates are never stable with respect to coarsening—although interaction between three precipitates can lead

to inverse coarsening. Nevertheless, since nanocrystals in the current experiment remained almost perfectly spherical up to the largest size observed (see Fig. 3.4), Johnson's analysis is still applicable. It can be used to explain why the nanocrystals coarsened initially when heated to 1000 °C (because they were below the critical size), but stopped after 2.5 min (because they had reached the critical size), why the final nanocrystal size was independent of the annealing history of the sample at lower temperatures, and why increasing the implantation dose did not increase the nanocrystal size. The stability against coarsening of two precipitates shown in Johnson's analysis, which used linear elasticity theory, can be understood qualitatively as follows: the energy of the system can be written as $E = E^M_{int} + E_{el} + E_s$, where E^M_{int} is the elastic interaction energy, E_{el} is the total elastic self energy (energy required to form two isolated precipitates), and E_s is the total surface energy; the elastic self energy of a precipitate depends linearly on its volume; therefore, E_{el} does not play a role in determining whether one precipitate grows at the expense of the other, so long as the total volume of the two precipitates remains constant; precipitates harder than the matrix repel each other, like two positive charges (E^M_{int} is positive), so that dissolution of one of the precipitates would decrease both E^M_{int} (to zero) and E_s—coarsening would reduce E; on the other hand, precipitates softer than the matrix attract each other, like a positive charge and a negative charge (E^M_{int} is negative), so that dissolution of one of the precipitates would decrease E_s but increase E^M_{int} (to zero)—coarsening would *not* necessarily reduce E; finally, note that E^M_{int} increases linearly with the the total precipitate volume V, so that there is a critical value of V below which E_s dominates, leading to coarsening, above which E^M_{int} dominates, leading to stability against coarsening—much like nucleation, in which the surface free energy of a nucleus dominates below the critical size, but the volume free energy of a nucleus dominates above the critical size.

3.4.3 Si nanocrystal precipitation

Unlike the precipitation of Ge nanocrystals, the precipitation of Si nanocrystals was likely diffusion-limited, due to the slow diffusion rate of Si atoms in silica. The implantation doses were apparently high enough to support nucleation, but required a high temperature anneal in order for Si to diffuse the required distance. The calculated D of 3.5×10^{-17} cm^2/sec at 1000 °C is higher than that obtained for ^{30}Si diffusion in crystalline silica (e.g., quartz) by Jaoul *et al.* [40]. Still, the calculated diffusion coefficient of Si at 1000 °C is 30 times smaller than that of Ge at 800 °C. Because of the small diffusivity of Si in silica, it would have taken at least 5 hr at 1000 °C for Si nanocrystals to reach 7 nm diameter—the average size of Ge nanocrystals at the temperature—for the high-dose implanted samples, assuming diffusion was the only limiting factor in their growth.

3.5 Summary

Ge nanocrystals 1–10 nm in size and Si nanocrystals 1–2 nm in size were fabricated by ion implantation and precipitation. For Ge, nucleation occurred during implantation for the mid-dose and high-dose implanted samples, and annealing at temperatures higher than 600 °C induced coarsening. The average Ge nanocrystal size increased, but nanocrystal concentration decreased, with increasing annealing temperature. Increasing the Ge implantation dose resulted in increased nanocrystal concentration but the same nanocrystal size. For Si, no nanocrystals were observed in as-implanted samples or samples annealed at less than 1000 °C. Samples annealed at 1000 °C for 40 min contained 1–2 nm Si nanocrystals. Finally, diffusion coefficient of Ge at 800 °C, 1000 °C, and 1200 °C, and of Si at 1000 °C, in vitreous silica, were obtained.

Bibliography

[1] D. J. DiMaria, J. R. Kirtley, E. J. Pakulis, D. W. Dong, T. S. Kuan, F. L. Pesavento, T. N. Theis, D. J. Cutro, and S. D. Brorson, J. App. Phys. **56**, 401 (1984).

[2] K. V. Shcheglov, C. M. Yang, K. J. Vahala, and Harry A. Atwater, Appl. Phys. Lett. **66**, 745 (1995).

[3] H. I. Hanafi, S. Tiwari, and I. Khan, IEEE Trans. on Elec. Dev. **43**, 1553 (1996).

[4] T. Takagahara and K. Takeda, Phys. Rev., **B46**, 15578 (1992).

[5] B. Delley and E.F. Stegmeier, Phys. Rev., **B47**, 1397 (1993).

[6] J. Heath, J. J. Shiang, and A. P. Alivisatos, J. Chem. Phys. **101**, 1607 (1994).

[7] C. M. Yang, K. V. Shcheglov, K. J. Vahala, and H. A. Atwater, Nucl. Instr. and Method in Physics Research B **106**, 433 (1995).

[8] K. S. Min, K. V. Shcheglov, C. M. Yang, H. A. Atwater, M. L. Brongersma and A. Polman, Appl. Phys. Lett. **68**, 2511 (1996).

[9] K. S. Min, K. V. Shcheglov, C. M. Yang, and H. A. Atwater, Appl. Phys. Lett. **69**, 2033 (1996).

[10] J. C. Vial, A. Bsiesy, F. Gaspard, R. Herino, M. Ligeon, F Muller, R. Romestain, and R. M. Macfarlane, Phys. Rev. B **45**, 14171 (1991).

[11] Y. Maeda, N. Tsukamoto, Y. Yazawa, Y. Kanemitsu, and Y. Masumoto, Appl. Phys. Lett., **59**, 3168 (1991).

[12] Y. Kanemitsu, H. Uto, Y. Masumoto, and Y. Maeda, Appl. Phys. Lett. **61** 2187 (1992).

[13] S. Hayashi, Y. Kanzawa, M. Kataoka, T. Nagareda, and K. Yamamoto, Z. Phys. **D26**, 144 (1993).

[14] S. Hayashi, M. Fujii, K. Yamamoto, Jpn. J. Appl. Phys., **28**, 1464 (1989).

[15] H. A. Atwater, K. V. Shcheglov, S. S. Wong, K. J. Vahala, R. C. Flagan, M. L. Brongersma and A. Polman, Mat. Res. Soc. Symp. Proc. **316**, 409 (1994).

[16] T. S. Iwayama, S. Nakao, and K. Saitoh, Appl. Phys. Lett. **65**, 1814 (1994).

[17] J. G. Zhu, C. W. White, J. D. Budai, S. P. Withrow, and Y. Chen, J. Appl. Phys. **78**, 4386 (1995).

[18] D. C. Paine, C. Caragianis, and Y. Shigesato, Appl. Phys. Lett. **60**, 2886 (1992).

[19] W. S. Liu, J. S. Chen, M. A. Nicolet, V. A. Engels, and K. L. Wang, Appl. Phys. Lett. **62**, 3321 (1993).

[20] S. Schuppler, S. L. Friedman, M. A. Marcus, D. L. Adler, Y. H. Xie, F. M. Ross, T. D. Harris, W. L. Brown, Y. J. Chabal, L. E. Brus, and P. H. Citrin, Phys. Rev. Lett. **72**, 2648 (1994).

[21] A. J. Kontkiewicz, A. M. Kontkiewicz, J. Siejka, S. Sen, G. Nowak, A. M. Hoff, P. Sakthivel, K. Ahmed, P. Mukherjee, S. Witanachchi, and J. Lagowski, Appl. Phys. Lett. **65**, 1436 (1994).

[22] R. P. Camata, H. A. Atwater, K. J. Vahala, and R. C. Flagan, Appl. Phys. Lett. **68**, 3162 (1996).

[23] I. M. Lifshitz and V. V. Slyozov, J. Phys. Chem. Solids **19**, 35 (1961).

[24] C. Wagner, Z. Elektrochem. **65**, 581 (1961).

[25] H. Hosono, N. Matsunami, A. Kudo and T. Ohtsuka, Appl. Phys. Lett. **65**, 1632 (1994).

[26] Y. Saito, J. Cryst. Growth **47**, 61 (1979).

[27] L. C. Liu and S. H. Risbud, J. Appl. Phys. **76**, 4576 (1994).

[28] E. Snoeks, A. Polman, and C. A. Volkert, Appl. Phys. Lett. *65*, 2487 (1994).

[29] W. C. Johnson, Acta Metall. **32**, 465 (1983).

[30] C. H. Su and P. W. Voorhees, Acta Mater. **44**, 1987 (1995).

[31] P. W. Voorhees and M. E. Glicksman, Acta Metall. **32**, 2001 (1984).

[32] P. W. Voorhees and M. E. Glicksman, Acta Metall. **32**, 2013 (1984).

[33] P. W. Voorhees and M. E. Glicksman, Metall. Trans. A **15A**, 1081 (1984).

[34] A. D. Brailsford and P. Wynblatt, Acta Metall. **27**, 489 (1978).

[35] C. K. L. Davies, P. Nash, and R. N. Stevens, Acta Metall. **28**, 179 (1979).

[36] J. A. Marqusee and J. Ross, J. Chem. Phys. **80**, 536 (1983).

[37] A. J. Ardell and R. B. Nicholson, Acta Metall. **14**, 1295 (1966).

[38] C. S. Jayanth and P. Nash, Mater. Sci. and Tech. **6**, 405 (1990).

[39] M. Jaraiz, G. H. Gilmer, J. M. Poate, and T. D. de la Rubia, Appl. Phys. Lett. *68*, 409 (1995).

[40] O. Jaoul, F. Béjina, F. Élie, and F. Abel, Phys. Rev. Lett. **74**, 2038 (1994).

Chapter 4 Selective Solid Phase Crystallization with Controlled Grain Size and Location in Ge Thin Films on Silicon Dioxide

4.1 Introduction

In this chapter an approach for low-temperature fabrication of thin polycrystalline Ge films on amorphous substrates with potentially very large grain sizes and controlled grain boundary locations is described. Achievement of very large grain sizes in thin Ge and Si films on amorphous insulating substrates is of interest to future low-cost thin-film electronic device technologies such as flat panel displays [1] and thin-film polycrystalline solar cells [2, 3]. Particularly important for fabrication of low-cost thin-film solar cells and thin-film transistors (TFT's) in active matrix displays is the use of low-cost substrates, such as glass. Since grain size enhancement and film growth must be accomplished at temperatures below the softening point of the glass substrate, solid phase crystallization methods are of particular interest. While approaches that employ film melting and solidification can lead to large grain size [4], the high temperatures required are most likely incompatible with low-cost substrates. In this chapter, results of selective solid phase crystallization for producing large grained (up to 100 μm) polycrystalline Ge films at low temperatures (< 475 °C), which is the first step in a process for fabrication of low-cost polycrystalline GaAs solar cell on glass substrates, are described. In previous studies of selective solid phase crystallization, the grain sizes obtained were comparable to film thicknesses [1, 5, 7, 8, 9, 13]. The large grain sizes in the current experiment were obtained in

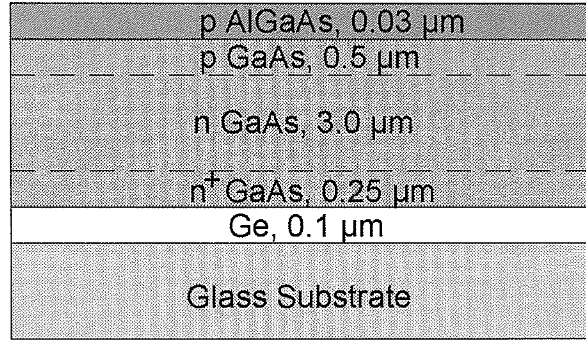

Figure 4.1: Schematic of a GaAs thin-film solar cell on top of a layer of Ge thin film, deposited on glass substrate. Since Ge has a very small lattice mismatch with GaAs, a crystalline Ge thin film can be used to seed epitaxial crystallization of GaAs.

films 20–100 nm thick, which represent an improvement of more than 2 orders of magnitude. For GaAs thin-film cells, achievement of large grain sizes is a concern as grain boundaries act as traps for minority carriers that lower cell efficiency [6]. Since GaAs is closely lattice-matched to Ge ($a = 5.653$ Å for GaAs and 5.657 Å for Ge), a Ge film with large grain size could be used to seed epitaxial growth of a GaAs overlayer to fabricate solar cells with large GaAs grain size [2]. A schematic of a GaAs solar cell with Ge thin-film seed layer, grown on glass substrate, is shown in Fig. 4.1. It should be noted that the present approach for selective Ge crystallization can also be applied to the production of large-grained polycrystalline Si thin-films with controlled grain boundaries.

The approach to selective solid phase crystallization taken here is based on metal-induced crystallization (MIC) of amorphous Ge (a-Ge). Thin-film metal islands deposited through a mechanical mask cause selective heterogeneous nucleation to occur at a much earlier time than random nucleation. Thus crystals which are selectively nucleated can grow to very large sizes via lateral solid phase epitaxy (SPE) before their growth is impeded by impingement with randomly nucleated crystal grains. This approach is illustrated in Fig. 4.2. Furthermore, implantation of B and P atoms (which have been shown to enhance SPE rate in Si but their effect on SPE rate in Ge was unknown) into some of the Ge films increased their crystal growth rate by up to a factor of 2 and 10, respectively. Thus, with the addition of B or P atoms even

larger grains were obtained. However, currently each nucleation site produces more than one crystal, resulting in a polycrystalline grain during growth. Possible ways of obtaining one crystal per nucleation site are discussed.

4.2 Methods of selective solid phase crystallization of Si and Ge

Many approaches for producing large-grained Si or Ge thin films on amorphous substrates have been demonstrated [7]–[20]. All of these methods require the selection of crystalline seeds from which lateral solid phase epitaxy proceeds. There are basically two types of seed selection: (1) those that can control both the density (thus the grain size) and the locations (thus the grain boundaries) of the crystals; (2) those that can only control the density of the crystals. The advantage of grain location and boundary control is the possibility of placing microelectronic devices such as thin-film transistors within one grain, away from the grain boundary, thus achieving single-crystal device quality and performance—without the use of higher cost single-crystal substrates. Some examples of both types of selective solid phase crystallization are discussed below. Although many of the techniques employed in Si crystallization could be used in Ge crystallization and vice versa, it should be noted that random nucleation in Si occurs at about 600 °C, whereas random nucleation in Ge occurs at about 500 °C, and solid phase epitaxy rate in Ge is higher than in Si at any temperature. Thus, in general selective crystallization of Ge can be performed at lower temperatures than Si.

4.2.1 Ion irradiation

One of the most widely used tools for manipulating crystal density and size in Si and Ge thin-films on amorphous substrates is ion irradiation [7]–[13]. For example, Reif and Knott [7] used Si ion irradiation to partially amorphize 240-nm-thick polycrystalline Si films (on SiO_2) containing 50 nm grains and obtained 175 nm grains

1. Create metal dots on top of amorphous Ge films by evaporating metals through a mask

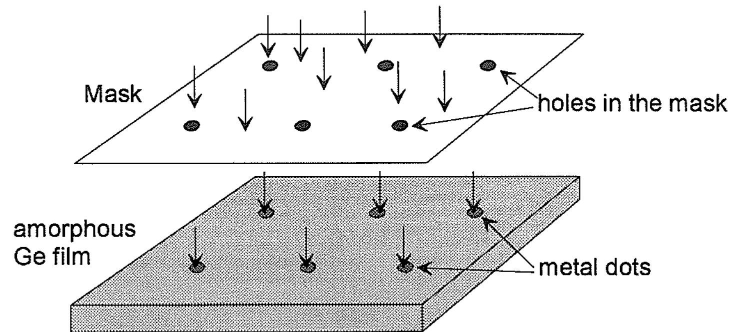

2. Upon annealing, Ge crystals nucleate selectively underneath the metal islands in amorphous Ge films.

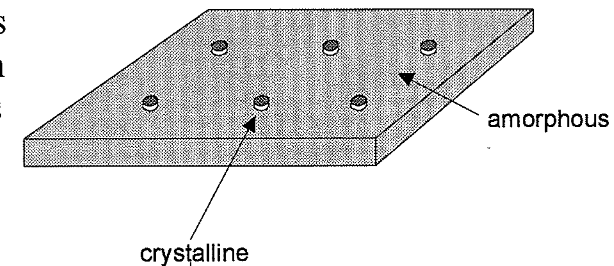

3. Annealing at higher temperature, crystals underneath the metal islands grow laterally.

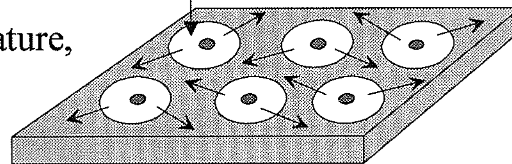

4. Crystals keep growing until they impinge on each other.

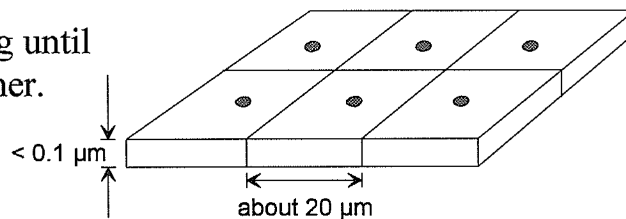

Figure 4.2: An illustration of the present approach for selective solid phase crystallization.

after a post-irradiation anneal at 525 °C for 81 hr. It was shown that only some of the grains survived the irradiation, possibly due to channelling of the ions (which would have minimize the collision of ions with atoms in properly oriented crystals), and grew during the subsequent anneal. The relatively low annealing temperature of 525 °C was chosen so that random nucleation would not occur but crystal growth would. Im *et al.* [9] performed ion irradiation on partially crystallized Si thin-films in order to suppress random nucleation. In their experiment irradiation and annealing were alternately performed several times, which resulted in growth of existing grains without additional nucleation. Specifically, after each annealing at 600 °C for 30 min to induce crystal growth, a Xe^{+} irradiation was performed in order to amorphize crystals which were about to reach thermodynamically-stable size. The authors showed that samples subjected to the same thermal treatment but without the intervening irradiation steps showed increased crystal density.

Besides amorphization of Si and Ge crystals, ion irradiation has also been used to induce growth of Si and Ge crystals, at temperatures low enough that crystal growth are negligible without ion irradiation. For example, Spinella and Lombardo [10] performed Xe^{+} irradiation on 90-nm-thick Si films containing 50 nm grains at 450 °C and increased the grain size to 150 nm. Oyoshi *et al.* [11] irradiated 160-nm-thick Si films at 350 °C with Si ions and increased the grain size from about 20 nm to about 100 nm. In both cases no nucleation was observed during crystal growth.

In addition to controlling Si crystal density, ion irradiation has also been used for controlling Si crystal location. For example, Kumomi and Yonehara [13] performed two irradiation steps to completely amorphize 100 nm Si films, except in areas of the films masked by photoresist. The resist pattern (0.66 μm in diameter, 3.0 μm in spacing) was laid down after the first Si irradiation step, which was performed to reduce crystal density so that on average only one crystal survived under each patch of resist. All of the crystals outside the resist were amorphized by the second irradiation, so that upon annealing at 600 °C crystals grew only from regions covered by the resist. However, in the first irradiation step the dose required to produce precisely one crystal per nucleation site needed to be fairly precise.

Aside from the aforementioned method of nucleation site selection, almost all other methods of site selection used some kind of catalyst, at chosen locations, to induce heterogeneous crystal nucleation. Among the artificial nucleation sites used were: SiN_x ($x < 4/3$) thin-films [14], regions of a-Si near steps (or ledges) in the underlying SiO_2 [15], and thin metal film-covered regions of a-Si [16, 18, 20]. For example, Kumomi and Yonehara [14] have shown that during chemical vapor deposition of Si at 950 °C, Si crystals preferentially nucleated on 4 μm × 4 μm squares of 100-nm-thick $SiN_{0.56}$, which were formed by Si ion implantation into Si_3N_4 (deposited on SiO_2) and subsequently patterned into isolated squares. During the Si deposition initially many small crystals (about 200 nm) appeared on each square, but did not grow with time. But one crystal finally grew to very large size (about 2 μm) and occupied the whole square. Each square of the $SiN_{0.56}$ produced one crystal; however, there was some uncertainty about the fate of the numerous small crystals that existed on each square.

4.2.2 Metal-induced crystallization

The formation of Si crystals by the above method requires relatively high temperature compared to the solid phase crystallization temperature of a-Si. In contrast, metals deposited on—or alloyed with—Si and Ge have been shown to lower the crystallization temperature of Si and Ge by more than 300 °C [17, 21]. For example, Liu and Fonash [16] have shown that crystallization of amorphous Si at selected areas could be accomplished at temperatures as low as 500 °C by covering those areas with 10 to 100 Å of Pd. Similarly, Lee *et al.* [18] evaporated 40 Å Pd films on a-Si and showed that crystallization of Pd-covered areas took place at 500 °C. In addition, they found that crystallization would spread laterally into areas not covered by Pd, as far as tens of microns at 500 °C for 10 hr. Later Pd was found in the crystallized areas that were initially Pd-free [19]. In contrast, they noted that a-Si films on which no Pd was deposited did not crystallize at 500 °C after 100 hr. Finally, Lee and Joo [20] demonstrated similar selective and lateral crystallization in a-Si at 500 °C using Ni. Although metal-induced crystallization in a-Si and a-Ge was discovered in the 1960's

[21], only recently has it been applied toward selective solid phase crystallization in Si and Ge. As discussed in the next section, the decrease in crystallization temperature of Si and Ge by MIC can be quite dramatic, making it a very useful tool for selective nucleation at low temperatures.

It has been shown that certain metals which form low-temperature eutectic phases or binary ordered compounds with crystalline Si or Ge can induce crystal nucleation in amorphous Si or Ge at temperatures much lower than those required for homogeneous nucleation. Figure 4.3 shows the In-Ge (eutectic) and Cu-Ge (binary compounds) phase diagrams; both metals lower the crystallization temperature by more than 250 °C, as shown in the next section. For Si, reductions in the crystallization temperature have been observed for reactions with Au, Al, Ag, Cu, Ni, In, and Pd [22]–[27]. Similarly, Al, Ag, Au, Cu, and Sn have been shown to induce Ge crystallization at substantially reduced temperatures [28]–[34]. Edelman *et al.* [30] reported a change of apparent activation energy for nucleation and growth from 2.0 eV for pure a-Ge to 0.9 eV for a-Ge in contact with Al or Au. Konno and Sinclair [33] performed *in-situ* cross-sectional transmission electron microscopy of a-Ge/Ag thin multilayer films at 270 °C and found that Ge crystallization started at the a-Ge/Ag interfaces, followed by the migration of Ag grains into the boundary between amorphous and crystalline Ge; as crystallization proceeded the Ag grains continually migrated into amorphous Ge, leaving crystalline Ge behind. This paralleled their findings for the a-Si/Al and a-Si/Ag layered thin films. Similarly, Lereah *et al.* [31] reported that codeposited $Ge_{0.5}Al_{0.5}$ alloy crystallized at 250 °C, that Ge crystals were surrounded by Al crystals, and that growth of Ge crystals occurred by diffusion of Ge atoms from amorphous Ge through the Al crystals to the Ge crystals.

4.3 Experiment and Results

In the present work, amorphous Ge films 20, 50, 80, or 100 nm thick were deposited by ultrahigh vacuum electron beam evaporation (base pressure 7×10^{-11} Torr; pressure during deposition typically 4–8 $\times 10^{-9}$ Torr) at 100 °C onto cleaned, thermally-grown

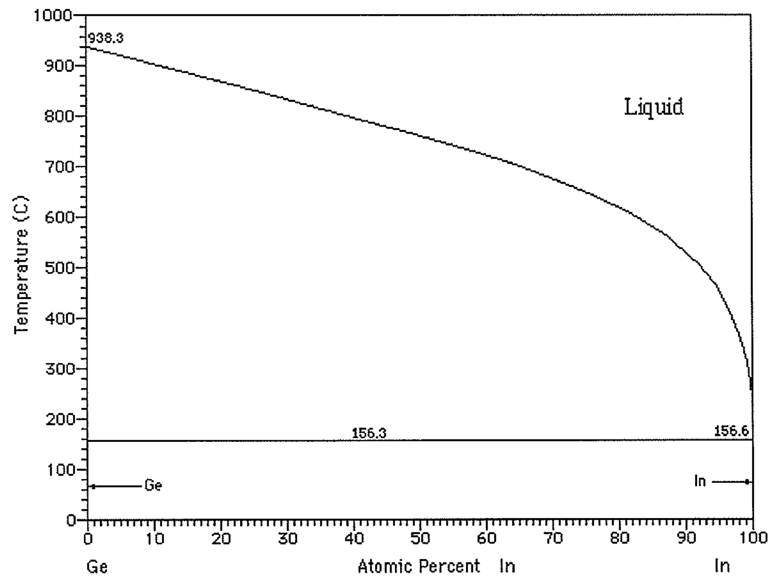

(a)

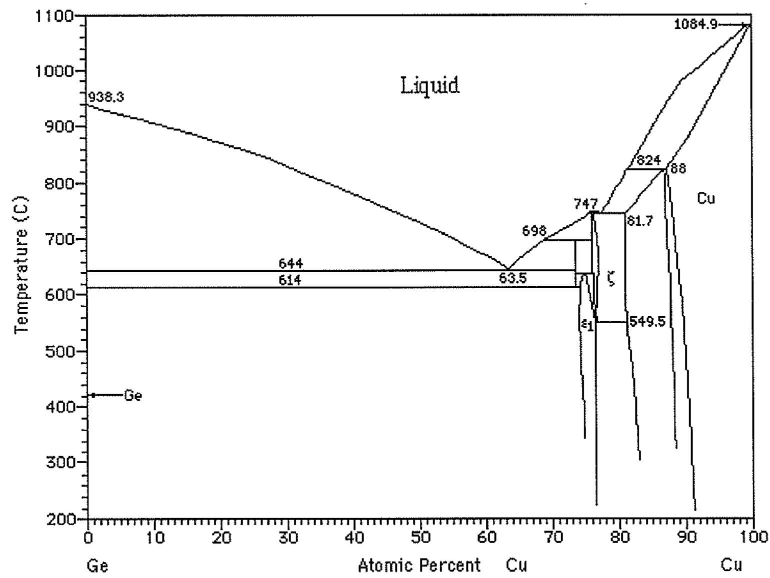

(b)

Figure 4.3: (a) In-Ge and (b) Cu-Ge binary phase diagram.

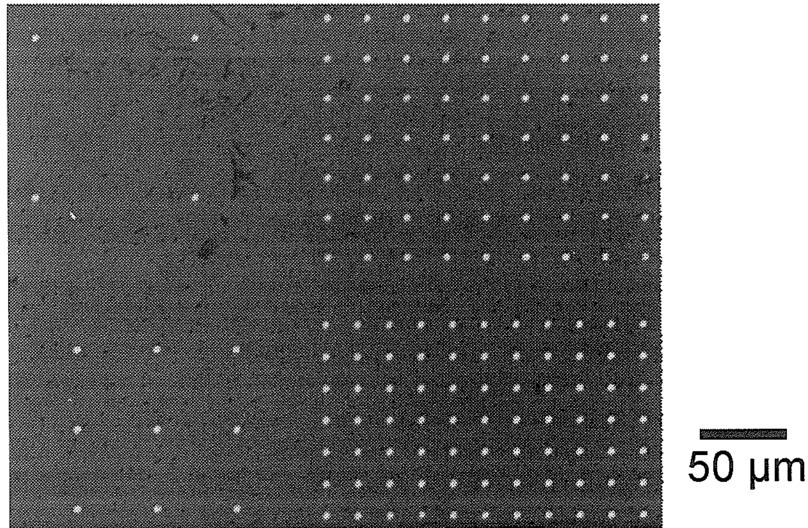

Figure 4.4: Optical micrograph of a glass slide with a 20-nm-thick In film on top, evaporated through a mechanical mask used in the current experiments. The bright spots are the 5-μm-diameter In islands produced by the mask pattern.

SiO_2 films on Si substrates. A patterned metal film was deposited in another high vacuum evaporator by mechanically masked lithography on top of the a-Ge film, with 5-μm-diameter metal islands spaced in periodic arrays of periods 20, 25, 50 or 100 μm. The mask pattern is shown in Fig. 4.4. Some of the metal films were deposited on the a-Ge film without the mask. The metals used included Au, Cu, In, Pd, Al, Sn, Co, and Ni, with thickness of either 10 or 20 nm. The metal-covered Ge films as well as films of pure amorphous Ge were annealed in a high vacuum furnace at temperatures ranging from 225 to 475 °C.

In order to increase the growth distance of selectively nucleated crystals before the onset of random nucleation, some of the Ge films were implanted with electronic dopants such as B and P. In particular, some of the 50-nm-thick Ge films were implanted with either 8 keV $^{10}B^+$ or 25 keV $^{31}P^+$, to a dose of 1×10^{15} at./cm^2, which corresponds to a peak concentration of 0.6 at. % at the center of the films. One of the films was doped with both the n-type dopant P and the p-type dopant B to study the compensation effect: in Si, doping with either B or P increases the SPE rate, but doping with both B and P results in the same SPE rate as undoped Si.

For 50-nm-thick pure amorphous Ge films, an incubation time before crystalliza-

Metal	ΔT_c (°C)
Au	≥ 250
Cu	≥ 250
In	≥ 250
Al	≤ 125
Pd	≤ 125
Ni	≥ 250
Co	≥ 250

Table 4.1: Table of the metal-induced lowering of the crystallization temperature of 20 nm Ge thin films. The result of Al might have been affected by the formation of aluminum oxide.

tion was observed, with crystal fraction of 0 at 475 °C after 5 min, 0.05 after 20 min, and 1 after 40 min, where crystal fractions were measured from bright field and dark field transmission electron micrographs. Figure 4.5 shows the bright field micrographs. Isochronal anneals for 60 min yielded crystal fractions of 0 at 425 °C, 0.05 at 450 °C, and 1 at 475 °C. The transmission electron diffraction patterns are shown in Fig. 4.6. These data are broadly consistent with previous studies of Ge crystallization (e.g., Ref. [30]; note that the films here were deposited under ultrahigh vacuum conditions, while the films described in Ref. [30] were deposited under ordinary high vacuum conditions, and no measurable differences in the Ge crystallization kinetics were found in these different experiments, suggesting that either significant levels of impurities are not incorporated into amorphous Ge or that their presence does not significantly affect crystallization.)

For 20-nm-thick Ge films with a blanket 10-nm-thick metal film on top, high vacuum annealing was carried out for 20 min at 225 °C, 350 °C, or 475 °C, and nucleation was found to occur in amorphous Ge films covered with In, Cu, Au, Co, Sn, and Ni at 225 °C, which is approximately 250 °C below the temperature at which crystallization of pure a-Ge occurs on a similar time scale. Films covered with Pd and Al crystallized only at 475 °C, close to the temperature of crystallization for pure a-Ge film. The findings are summarized in Table 4.1 Previous studies [28, 30, 31] have found that a-Ge crystallized at or below 250 °C when in contact with Al; the disagreement between those results and the present result is most likely due to the formation

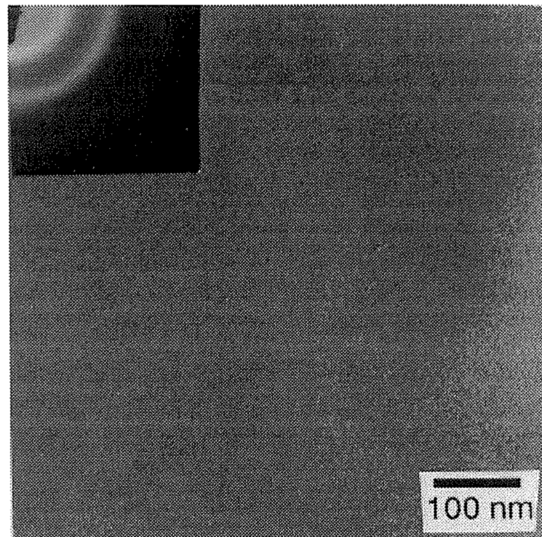

(a)

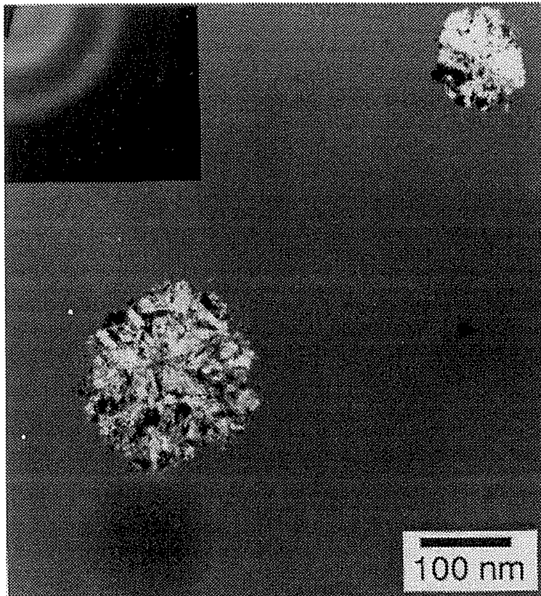

(b)

(c)

Figure 4.5: Bright field transmission electron micrograph of 50-nm-thick Ge film annealed at 475 °C for (a) 5 min, (b) 20 min, and (c) 40 min.

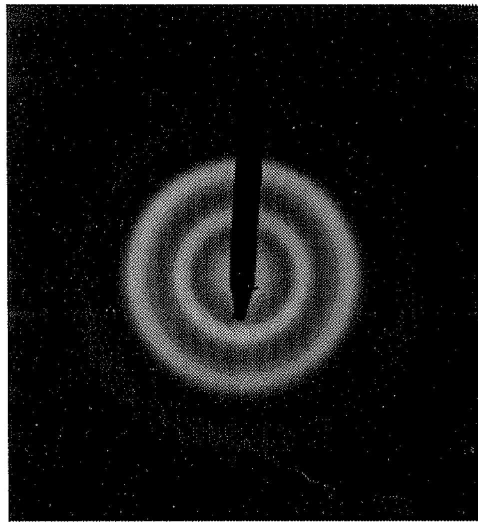

(a)

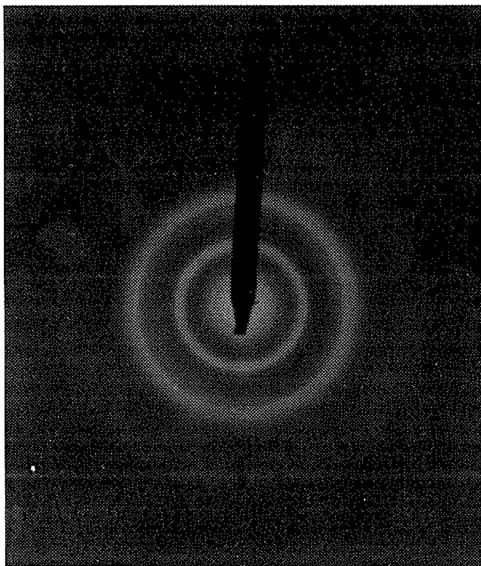

(b)

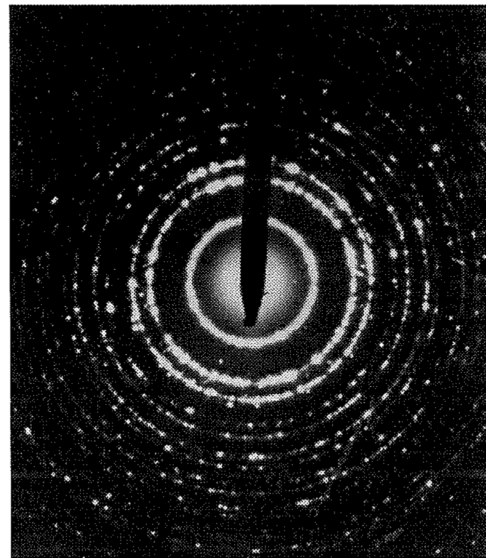

(c)

Figure 4.6: Transmission electron diffraction pattern of 50-nm-thick Ge film annealed for 60 min at (a) 425 °C, (b) 450 °C, and (c) 475 °C.

of aluminum oxide—which would have consumed the Al thin film—in the present experiment. Aside from this discrepancy, the present results are consistent with other experimental results. For example, Edelman *et al.* [35] found that hydrogenated amorphous Ge (a-Ge:H) under a Pd thin-film crystallizes at 400-500 °C; Tan *et al.* [34] found that Au/Ge bilayers crystallizes at 170 °C.

Further studies of metal-induced crystallization were conducted using Ge films covered with an Au, Cu, or In thin metal film. These metal films were patterned using the mechanical masks in order to distinguish between metals that crystallize only the a-Ge region underneath them and metals that diffuse into neighboring regions, causing crystallization of those regions as well (as in the case of Pd-Si system [18] and Ni-Si system [20]). This distinction is important because metal atoms present in large quantities in Ge or Si thin-film electronic devices can degrade device performance [20]. On the other hand, metals that do not diffuse into Ge or Si films can be removed by chemical etching. The results are shown in Fig. 4.7 and 4.8, which are bright field and dark field micrographs, respectively, of Au, Cu, or In island on 20-nm-thick Ge films, after a 20 min anneal at 350 °C. The bright field micrographs show that Cu, In, and Au films were discontinuous. The diffraction pattern in the inset of Fig. 4.7(a) shows that the Cu/Ge film consist of crystalline Ge as well as Cu_3Ge compound. This is consistent with the results of Smith *et al.*, who reported formation of Cu_3Ge at room temperature after Cu deposition on polycrystalline Ge. In contrast, the In/Ge and Au/Ge films contained only crystalline Ge and elemental metal phase. This is to be expected, since In (as Fig. 4.3 shows) and Au do not form binary compounds with Ge. The Au and Cu island in Fig. 4.7 are not perfectly circular like the In island. In the case of Cu it was due to the diffusion of Cu into Ge to form Cu_3Ge compound. In the case of Au the non-circular shape was likely due to the shifting or buckling of the mask during deposition; the shape of Au islands were found to be non-circular even before annealing. Figure 4.7(c) shows evidence of surface migration of Au atoms during annealing or deposition: some of the dark Au spots have a neck between them, which is a sign of agglomeration.

The dark field transmission electron micrographs in Fig. 4.8(b) and 4.8(c) show

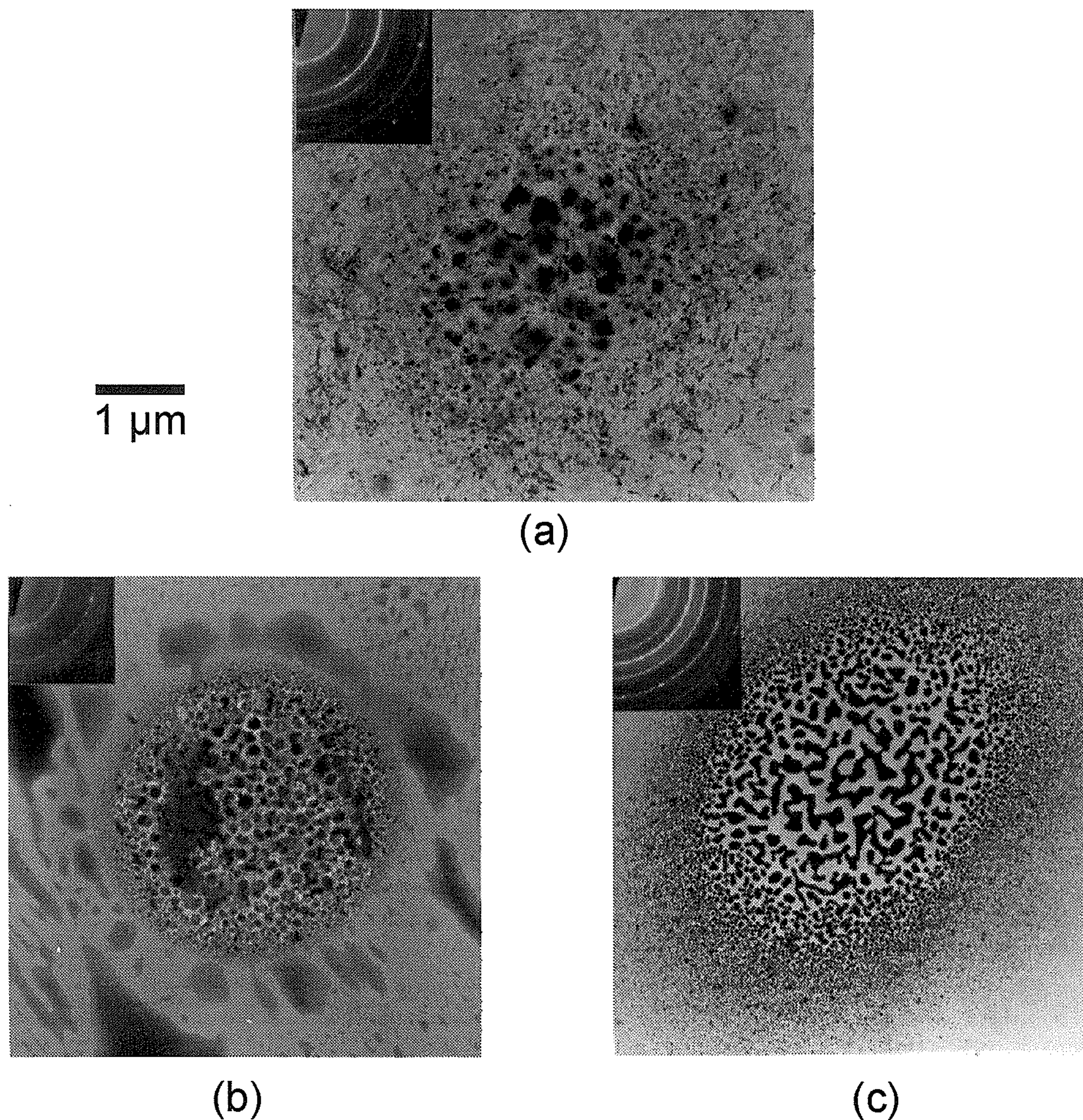

Figure 4.7: In (a), bright field transmission electron micrograph of 20-nm-thick Ge film with 20-nm-thick 5-μm-diameter Cu island on top, annealed at 350 °C for 20 min. In (b) and (c), same as in (a) except with In island and Au island, respectively, on top. The dark spots (due to thickness contrast) in (a), (b), and (c) are the Cu, In, and Au thin film, respectively.

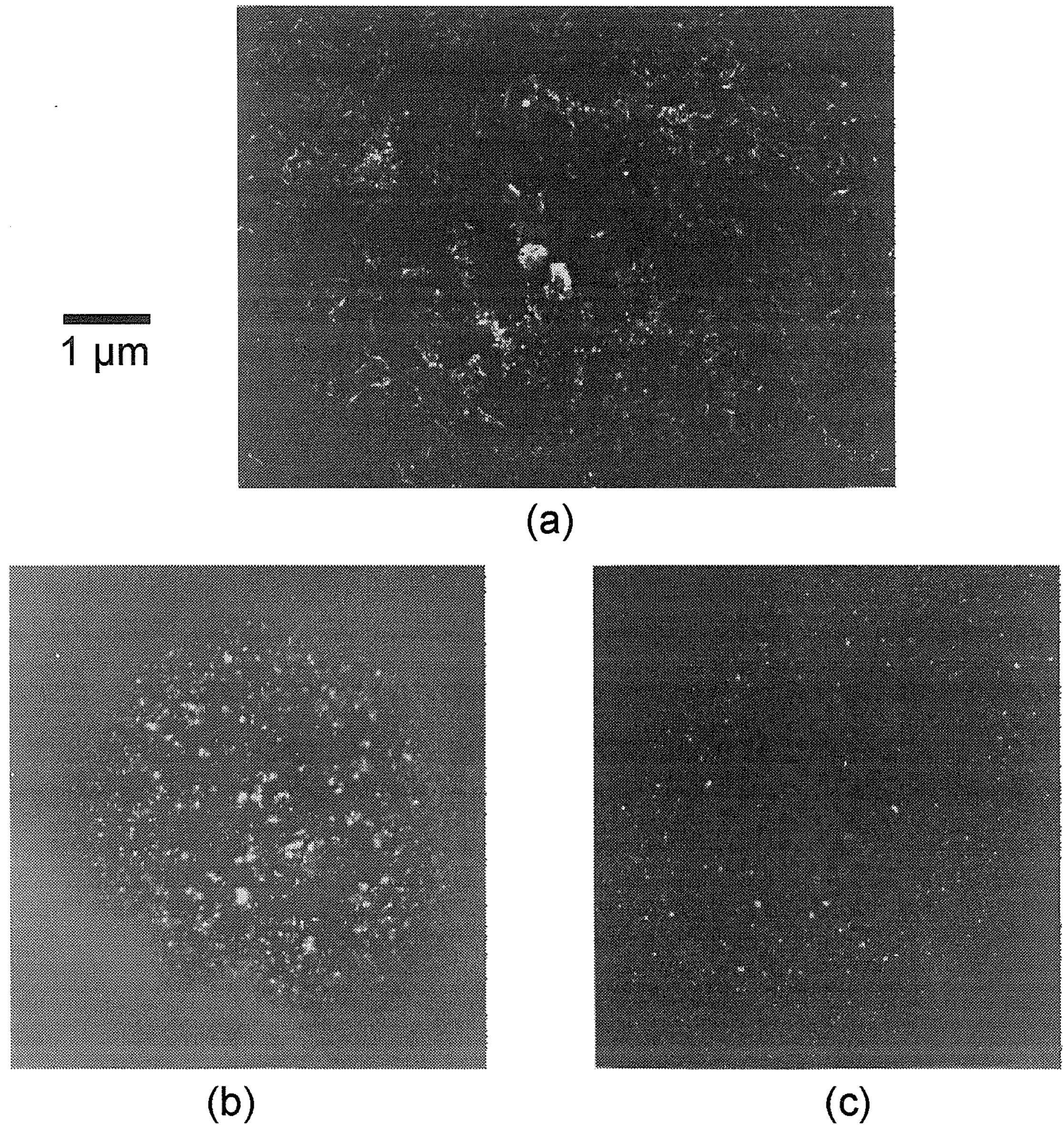

Figure 4.8: In (a), dark field transmission electron micrograph of 20-nm-thick Ge film with 20-nm-thick 5-μm-diameter Cu island on top, annealed at 350 °C for 20 min. In (b) and (c), same as in (a) except with In island and Au island, respectively, on top. The bright spots are the Ge crystals, selected using the (220) and (311) diffraction rings of crystalline Ge.

that at 350 °C crystallization only occurred underneath the In island and Au island. On the other hand, the dark field micrograph in Fig. 4.8(a) shows that crystallization of the Ge film had spread beyond the 5-μm-diameter Cu island after annealing at 350 °C for 20 min. The distance crystallized is about 10-15 μm. Since pure amorphous Ge does not crystallize at this temperature, the above result means that Cu diffused into amorphous Ge and continually migrated outward. This is similar to that observed for Ni-implanted amorphous Si [36]: *in-situ* TEM observation revealed that a thin region of epitaxial crystalline Si first formed on a (111) face of a $NiSi_2$ precipitate, then the $NiSi_2$ precipitate steadily migrated into amorphous Si, leaving a trail of epitaxial Si behind (the growth rate of c-Si was determined by the Si diffusion through the $NiSi_2$ precipitate.)

Since indium can be deposited at selected areas without surface migration or diffusing into Ge (due to its small solubility in crystalline Ge, as Fig. 4.3 shows), it was used as the metal of choice in all subsequent nucleation and growth studies. In addition, Ge film thickness was increased to 50 nm, due to the concern that film thickness too small might limit lateral solid phase epitaxy rate, as is the case for Si [37]. On the other hand, excessive film thickness (> 100 nm) would have prevented the ability to perform transmission electron microscopy on the films. Figure 4.9 shows bright field and dark field transmission electron micrographs of a selective nucleation site, near a 20-nm-thick In island, after a 350 °C, 20 min anneal. As these images show, selective nucleation resulted in not one but many grains under the 5-μm-diameter metal islands. The crystal density was found to be highest near the edges of metal islands where metal island thickness was smaller, possibly due to penumbral shadowing during the mechanically masked deposition. Since crystal grains at the edge of the metal islands act as seeds for lateral solid phase epitaxial growth, the microstructure after lateral solid phase epitaxy consists of many large elongated grains rather than a single large grain growing radially from under each metal island. The results of crystal growth after selective nucleation are shown in Fig. 4.10, which contains bright field micrographs of Ge grains in 50-nm-thick amorphous Ge films following a two-step anneal: 350 °C for 20 min to induce selective nucleation, followed

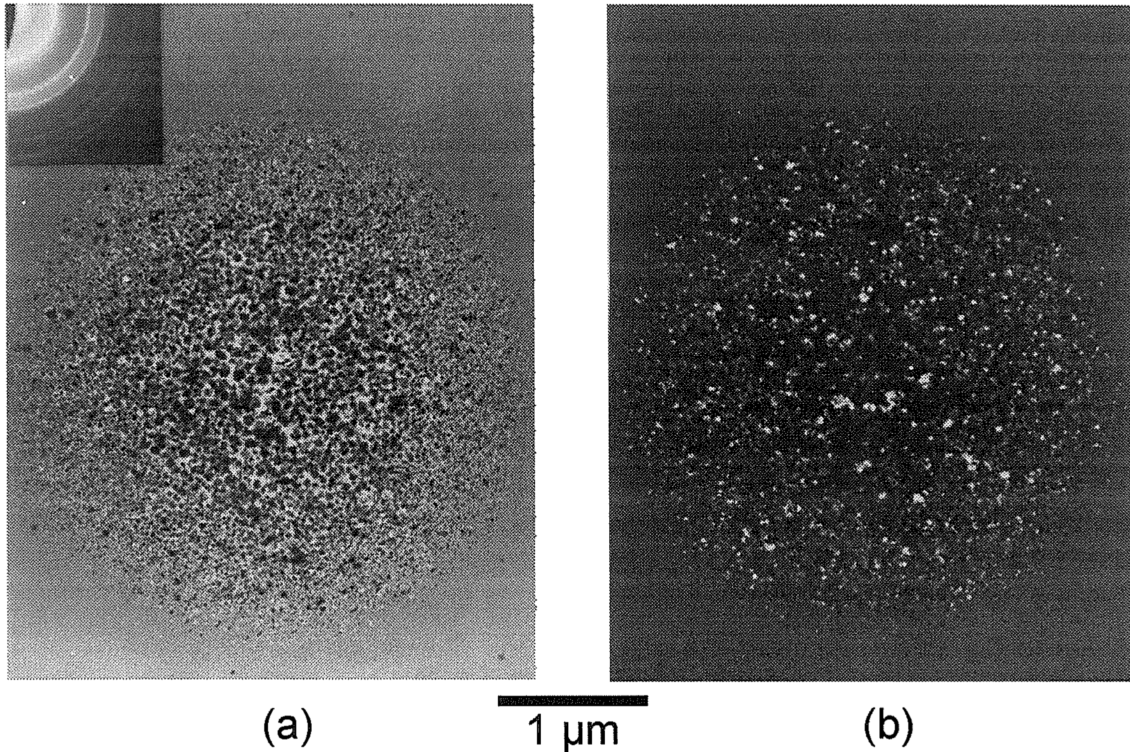

Figure 4.9: (a) bright field and (b) dark field electron micrograph of 50-nm-thick Ge film with 20-nm-thick In island on top, annealed for 20 min at 350 °C.

by a 425 °C, 450 °C, and 475 °C anneal for 2 hr, 50 min, and 10 min, respectively, to induce lateral solid phase epitaxy. It was found that anneals at higher temperatures that produced the same overall crystallized fraction as the 425 °C anneals (e.g., 450 °C for 50 min or 475 °C for 10 min) resulted in a greater extent of random nucleation relative to selective nucleation.

Some amorphous Ge films were doped by ion implantation with electronic dopants such as B and P prior to selective solid phase crystallization. Doping with B and P up to peak concentration of 0.6 at. % had no observable effect on the rate of random nucleation, as compared with undoped films. However B and P doping resulted in significant lateral solid phase epitaxial growth rate enhancements: a factor of 2 for 50 nm Ge films doped with 0.6 at. % B and a factor of 5 for 50 nm Ge films doped with 0.6 at. % P, in the temperature range from 400 to 475 °C. Figure 4.11 shows dark field micrographs of an undoped Ge film and a B-doped Ge film, annealed at 350 °C for 20 min and then at 425 °C for 2 hr. The B-doped film contained larger grains than

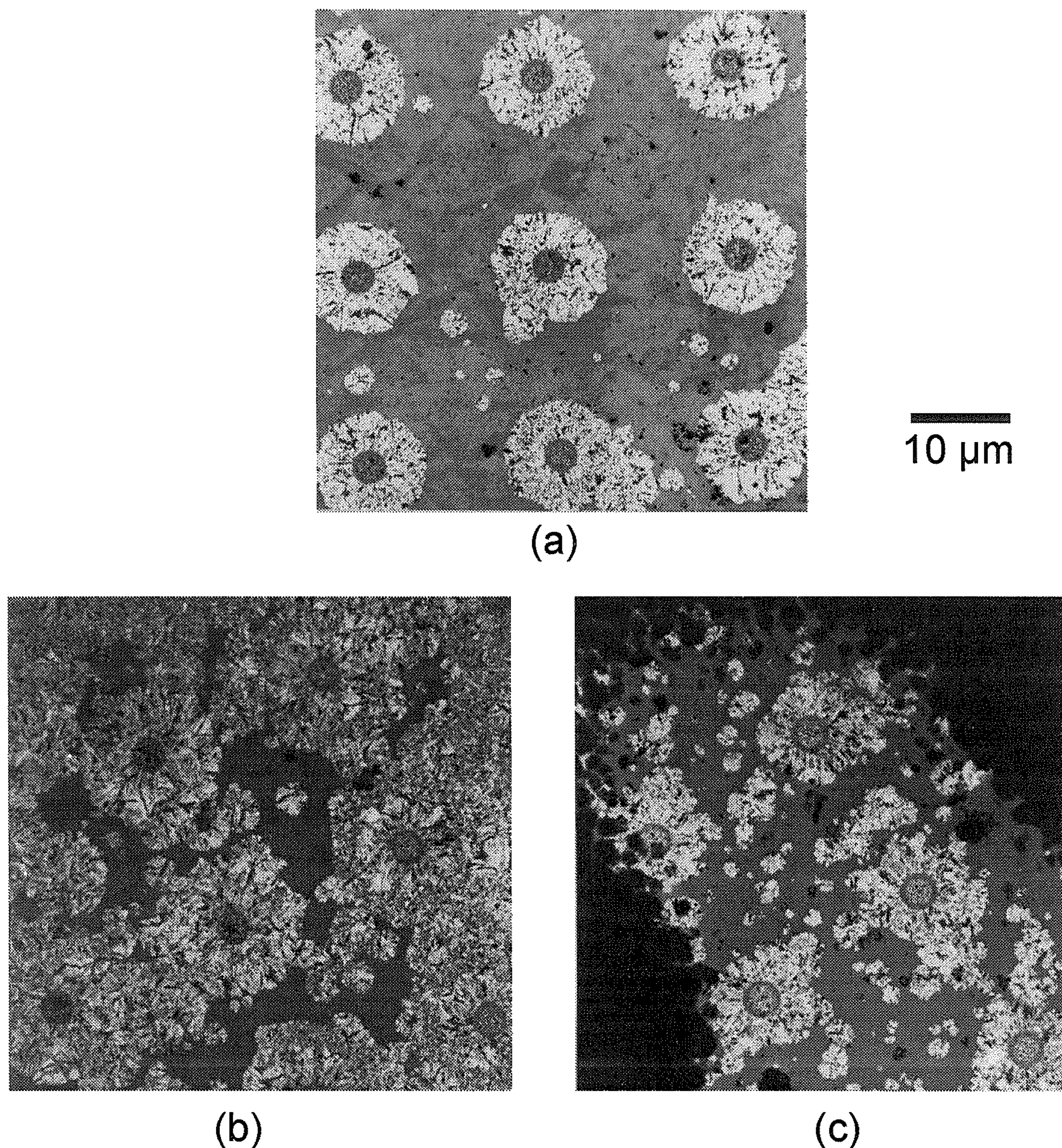

Figure 4.10: Bright field transmission electron micrograph illustrating selective nucleation and growth of Ge grains in a 50-nm-thick amorphous Ge film on SiO_2. The films where subjected to a two-step vacuum anneal of 350 °C for 20 min to induce selective nucleation, followed by a (a) 425 °C for 2 hr, (b) 450 °C for 50 min, and (c) 475 °C for 10 min anneal to induce lateral solid phase epitaxy.

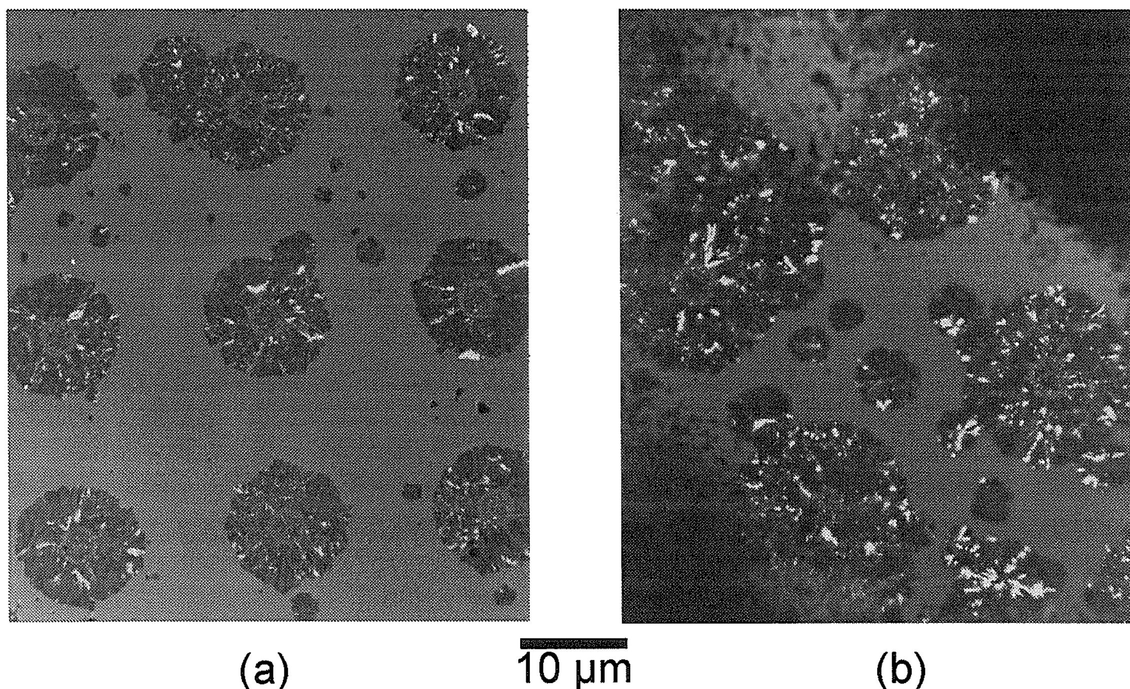

Figure 4.11: In (a), dark field micrograph of 50-nm-thick Ge film with 20-nm-thick In islands on top, annealed at 350 °C for 20 min and then 425 °C for 2 hr. In (b), same treatment as in (a) except the Ge film was doped with 0.6 at. % B.

the undoped film at the In island nucleation sites. Although the number of randomly nucleated crystals in both the undoped film and the B-doped film were the about same (proof that 0.6 at. % B doping did not enhance nucleation), those in the B-doped film were larger, as expected. Figure 4.12 shows dark field micrograph of an undoped Ge film and a P-doped Ge film, annealed at 350 °C for 20 min and then at 475 °C for 10 min. The P-doped film was completely crystallized, with Ge grain sizes as large as 10 μm, limited in size by the spacing between nucleation sites. Figures 4.13(a) and (b) are bright field and dark field transmission electron micrographs, respectively, near an In nucleation site in a 50-nm-thick P-doped amorphous Ge film after a two-step anneal of 350 °C for 20 min followed by 450 °C for 50 min. The selected-area diffraction patterns indicate very small grain sizes in the nucleation site region and large grains that grew radially outward outside of the nucleation site region.

Figure 4.14 demonstrates the improvement in selective crystallization that can be achieved via (a) annealing at lower temperatures to reduce random nucleation,

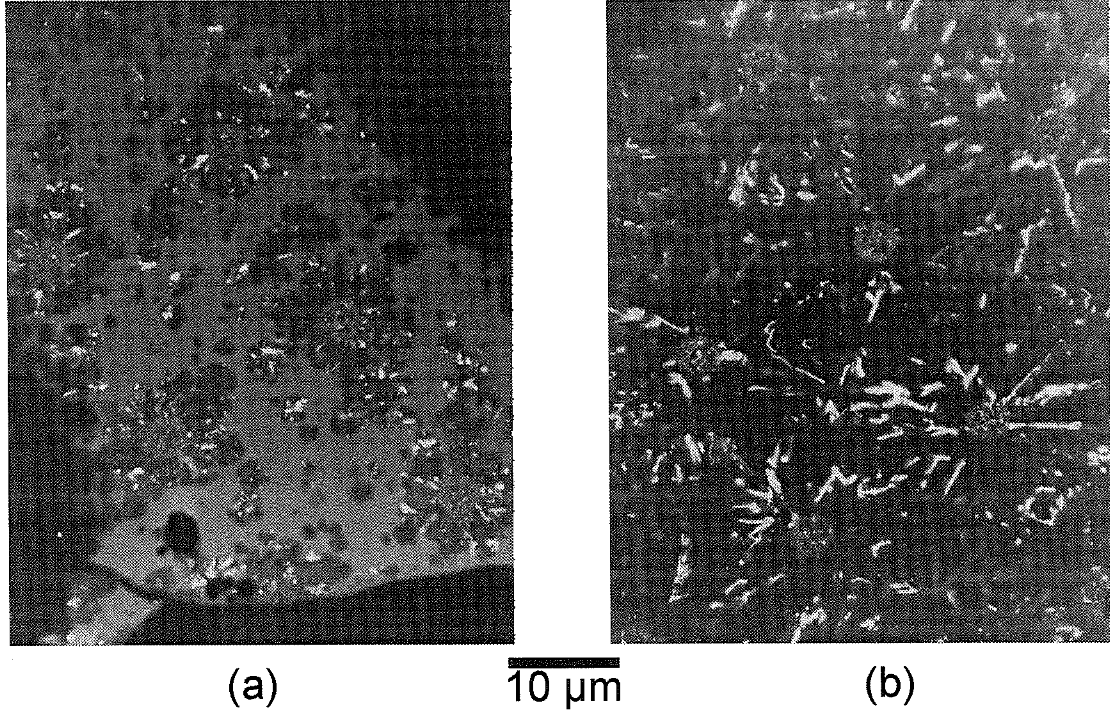

Figure 4.12: In (a), a dark field micrograph of 50-nm-thick Ge film with 20-nm-thick In islands on top, annealed at 350 °C for 20 min and then 425 °C for 2 hr. In (b), same treatment as in (a) except the Ge film was doped with 0.6 at. % P, which is fully crystallized with grain sizes as large as 15 μm.

and (b) increasing doping concentration to increase crystal growth rate. It shows an optical micrograph of 100-nm-thick Ge on SiO_2, implanted with 50 keV $^{31}P^+$ to a dose of 2×10^{15} at./cm^2, and then annealed at 400 °C for 100 min. The implantation dose and energy correspond to a peak concentration of 0.7 at. % at the center of the Ge film. Virtually no randomly nucleated crystals are visible between the 20 μm grains. The improvement in SPE rate over undoped samples is about a factor of 10.

Figure 4.15 shows the temperature dependence of the lateral solid phase epitaxy rate v for undoped 50-nm-thick Ge films. Also shown in Fig. 4.15 are data reported for [100] orientation planar solid phase epitaxy from single-crystal Ge seeds [38, 39]. The temperature dependence of v can be described by

$$v = v_0 \exp(-E_a/kT), \tag{4.1}$$

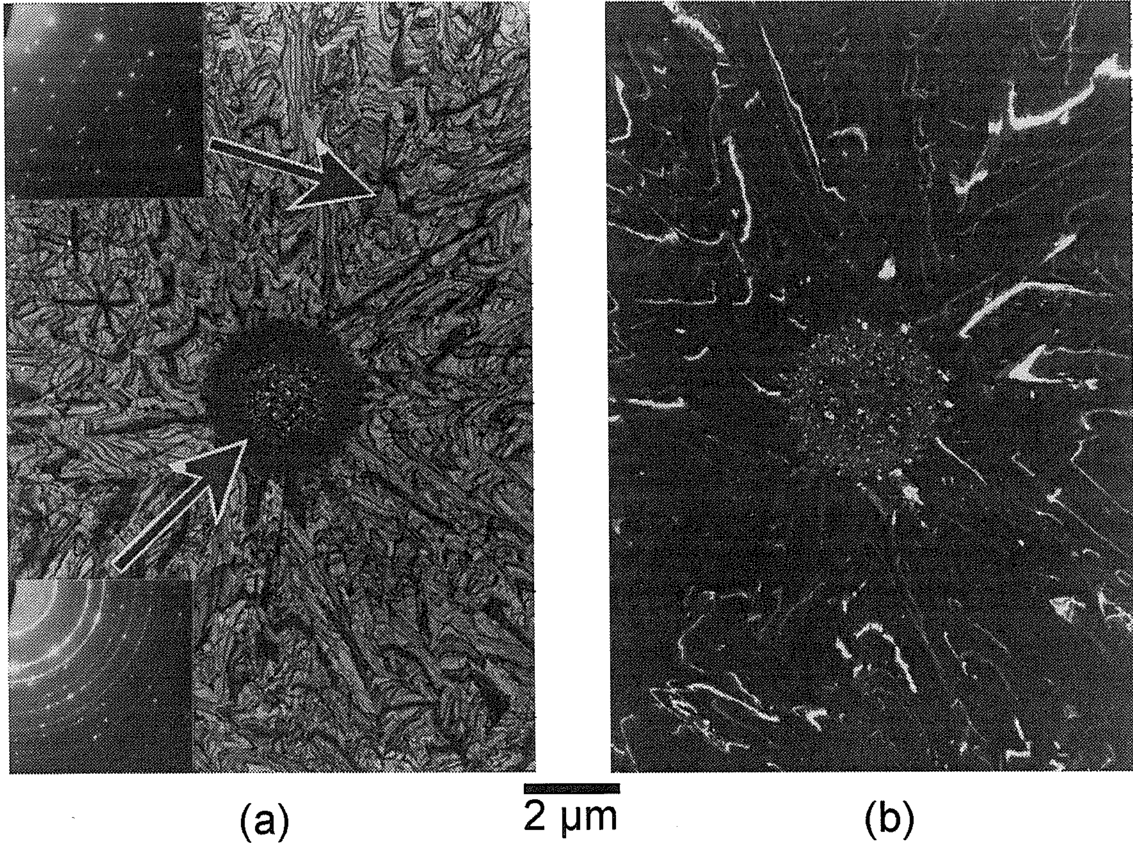

Figure 4.13: In (a), bright field micrograph of a nucleation site for selective nucleation and growth in a 50-nm-thick P-doped amorphous Ge film on SiO_2 after a two-step anneal of 350 °C for 20 min followed by 450 °C for 50 min. Selected area diffraction patterns indicate very small grain size in the nucleation site region and large grains that grew radially outward outside of the nucleation site region. In (b), the corresponding dark field micrograph.

with an activation energy E_a of 2.1 eV for the current experiment, close to the 2.2 eV and 2.3 eV reported for [100] planar SPE by Olson *et al.* [38] and Liu *et al.* [39], respectively. The close agreement in the activation energies indicates that the microscopic mechanism for lateral solid phase epitaxy is the same as that of the [100] planar SPE, which is thought to be bond-breaking and rearrangement at the crystal-amorphous (c-a) interface [40]; according to a kinetic analysis [39] of the Spaepen-Turnbull interfacial dangling bond mechanism [40], E_a is equal to $\Delta H_f + \Delta H_m$, where ΔH_f is the enthalpy for formation of a pair of dangling bonds, and ΔH_m is the enthalpy for motion of a dangling bond. However, the SPE rate is lower in the present work, which may be either a result of the film thickness or the difference in interface

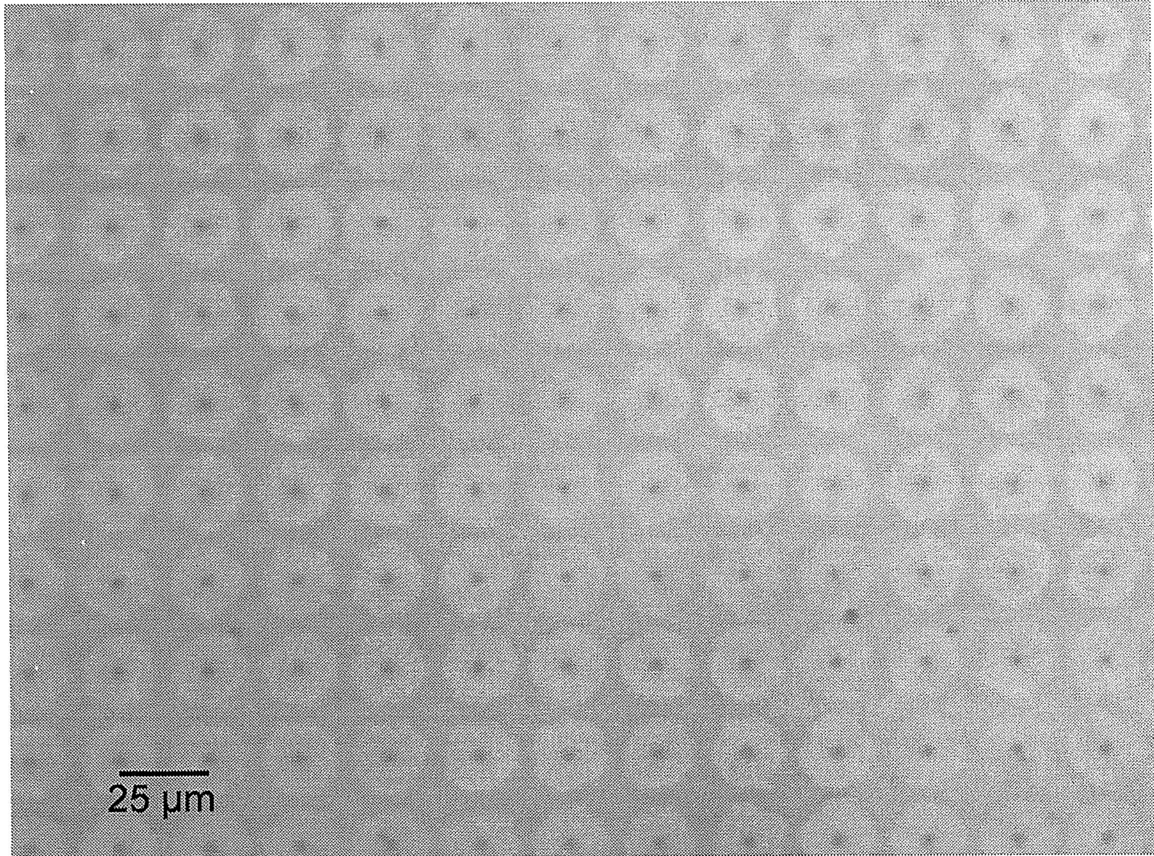

Figure 4.14: Optical micrograph of 100-nm-thick a-Ge on SiO_2, implanted with 50 keV $^{31}P^+$ to a dose of 2×10^{15} at./cm^2, and then annealed at 400 °C for 100 min. The implantation dose and energy correspond to a peak concentration of 0.7 at. % at the center of the Ge film.

orientation, as lateral SPE rate is thought to be limited by the slower growth rates of (111) and (110) interface planes. Figure 4.16 shows the temperature dependence of the lateral solid phase epitaxy rate for B-doped and P-doped 50-nm-thick Ge films. The activation energies of the doped Ge films are, within experimental uncertainty, equal to that of the undoped films. Therefore, the changes in v of the doped films are due to changes in the pre-exponential factor v_0. It is interesting to note that Ge films doped concurrently with both B and P atoms exhibited lower SPE rate than undoped films and films doped with only B or only P atoms. Since B is p-type dopant and P is a n-type dopant, this shows that the change in SPE rate by B and P doping is an electronic effect. Dopant compensation effect has also been observed for SPE in Si [38]. However, this is the first report of a dopant effect and of a dopant compensation

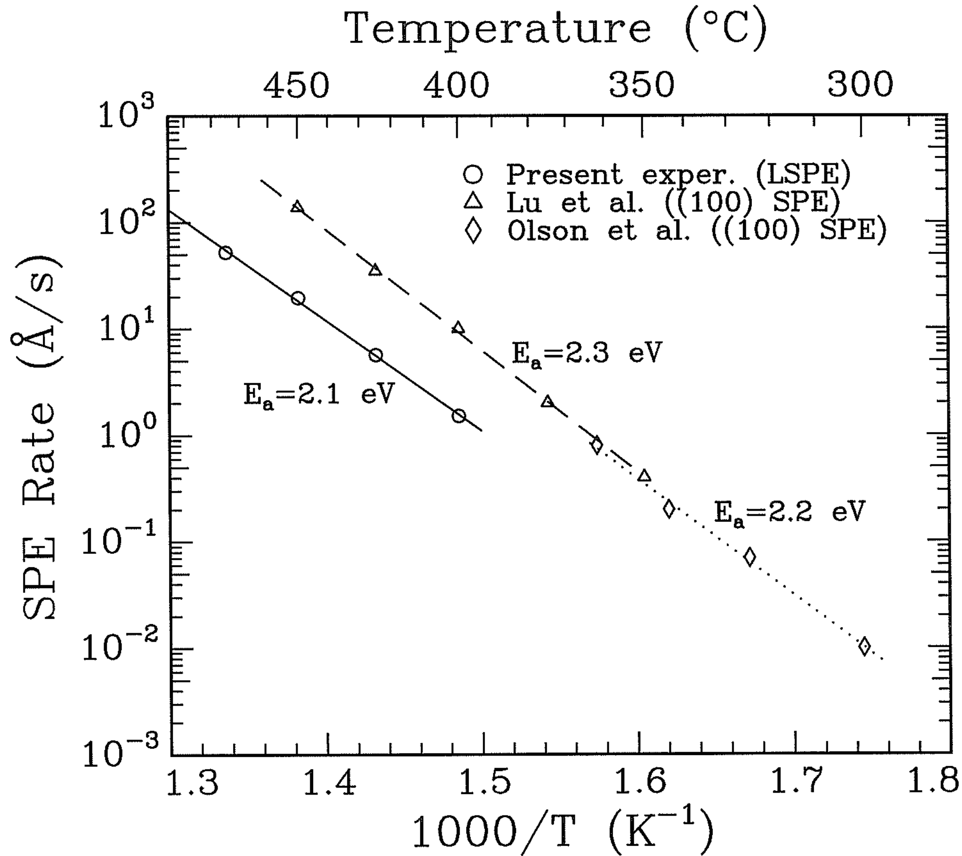

Figure 4.15: Arrhenius plot of lateral solid phase epitaxial growth rate with temperature in 50 nm amorphous Ge films on SiO_2 (circles). The solid phase epitaxial growth rate of (100)-oriented single crystals (triangles and diamonds) from Ref. [38] and [39] are also plotted.

effect in Ge SPE rate. The enhancement of SPE rate by electronic dopants in Si was thought be due to the shifting of the Fermi level, resulting in a change in the density of charged kink sites at the c-a interface [41] (a change in v_0 but not in E_a).

In order to find the effect of the Ge film thickness on lateral SPE rate, amorphous Ge films with thicknesses of 20 nm, 50 nm, or 80 nm were covered with a patterned 20-nm-thick In film and annealed at 350 °C for 20 min, and then annealed 425 °C for 2 hr. The results indicate that, within the range studied, film thickness had no effect on lateral SPE rate. In contrast, Moniwa *et al.* [37] found that lateral SPE rate in Si increased linearly with increasing film thickness, possibly due to the stress in the Si film developed during cooling after deposition, caused by the difference between the

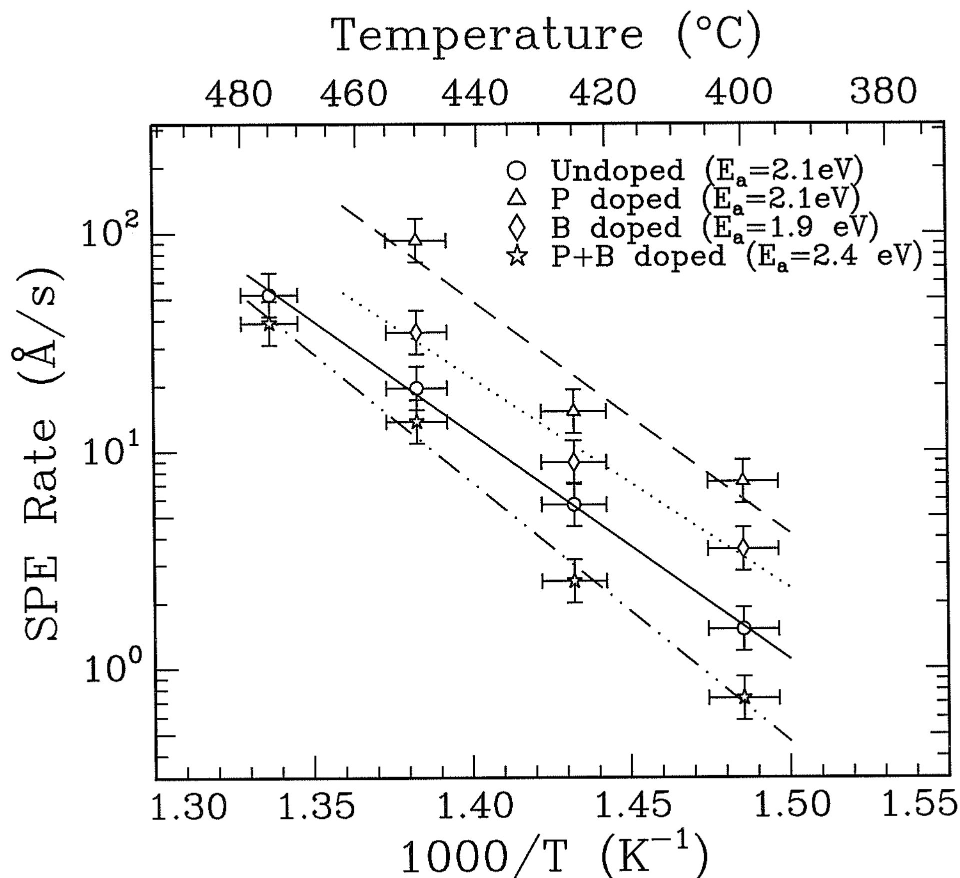

Figure 4.16: Arrhenius plot of lateral solid phase epitaxial growth rate with temperature in 50 nm amorphous Ge films on SiO_2. There were four type of films: (1) undoped, (2) doped with 0.6 at. % B, (3) doped with 0.6 at. % P, and (4) doped with both 0.6 at. % B and 0.6 at. % P.

thermal expansion coefficient of the SiO_2 substrate and the Si film.

The effect of amorphous Ge film thickness on the random nucleation rate of Ge crystals was also investigated. Pure (no metal overlayer or electronic dopant) amorphous Ge films of 20 nm, 50 nm, or 80 nm thickness were annealed at 475 °C for 10 min. The crystal density per unit area (from plan-view TEM) was approximately the same for all three film thicknesses. Since homogeneous nucleation should produce a crystal density that increases linearly with film thickness, this result indicates that random crystal nucleation in our experiment was due to heterogeneous nucleation, possibly at the Ge free surface or at the Ge/SiO_2 interface.

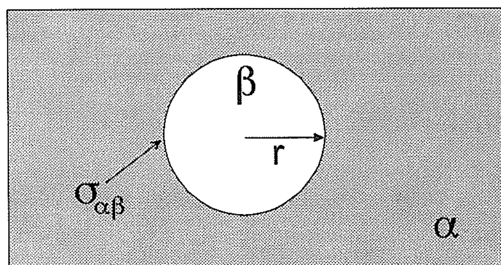

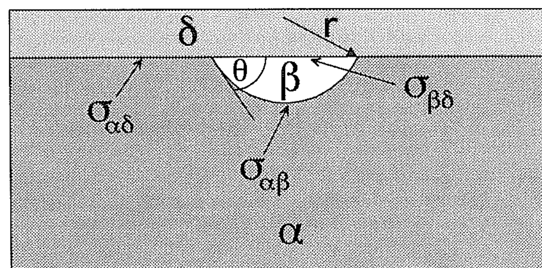

Figure 4.17: Schematic of homogeneous nucleation vs. heterogeneous nucleation.

4.4 Discussion

4.4.1 Metal-induced heterogeneous nucleation

The results of selective nucleation using In and Au islands suggest that the metal islands not only provided sites for heterogeneous nucleation, but also a different mechanism for crystal growth, as discussed below. The classical view of heterogeneous nucleation vs. homogeneous nucleation is shown in Fig. 4.17. As the figure shows, in heterogeneous nucleation the nucleus is a spherical cap with contact angle θ. The contact angle is determined by the static equilibrium condition

$$\sigma_{\alpha\delta} = \sigma_{\beta\delta} + \sigma_{\alpha\beta} \cos\theta, \tag{4.2}$$

where $\sigma_{\alpha\delta}$ is the interfacial energy between the α phase and the δ phase, and so on. Assuming that the incubation time for homogeneous nucleation is t_m and that for heterogeneous nucleation is t_t, scaling arguments by Greer *et al.* [42] have shown that the ratio t_t/t_m is a function solely of θ. Theoretical results by Kashchiev [43] indicate that the temperature dependence of t_m is given by

$$t_m \propto T \exp(E_d/kT), \tag{4.3}$$

where E_d is the activation energy for nuclei growth. In the case of Si and Ge crystal nucleation, E_d is the activation energy for crystal growth, E_a. An Arrhenius plot of

$\ln(t_m)$ as a function of $1/kT$ gives an apparent activation energy E_m, where

$$E_m = \frac{d\ln(t_m)}{d(1/kT)} \quad (4.4)$$

$$= E_d - kT. \quad (4.5)$$

Assuming that the contact angle θ is temperature independent in the range of interest (200–600 °C), then the ratio t_t/t_m is temperature independent, and $E_t = E_m$, where E_t is the apparent activation energy for t_t. At the crystallization temperatures of Si and Ge, $kT \approx 0.07$ eV, much less than the measured 2.7 eV [38] for E_a of Si and 2.2 eV [38] for E_a of Ge; thus,

$$E_m = E_t \approx E_a, \quad (4.6)$$

for Si and Ge crystal nucleation. Therefore, for both homogeneous and heterogeneous crystal nucleation, the activation energy for incubation time is the same as that of crystal growth. (This result can be understood qualitatively as follows: crystal growth in amorphous Si and Ge is controlled by a interfacial process; in both homogeneous and heterogeneous nucleation, a nucleus grows by attachment of atoms at the c-a interface; thus, the dominant factor in determining the temperature dependence of incubation time is the activation energy for the interfacial process, and a heterogeneous nucleation process such as the one shown in Fig. 4.17 merely reduces, as a function of θ, the critical volume for thermal stability.) The above equation is in good agreement with experiment: Iverson and Reif [44] obtained E_m of 2.7 eV for the crystallization of amorphous Si films on SiO_2; Edelman *et al.* [30] obtained E_t (or E_m) of 2.0 eV for crystallization of amorphous Ge films. The incubation time for crystallization of pure amorphous Ge can also be estimated from the micrographs shown in Figs. 4.5, 4.6, and 4.10. An Arrhenius plot of t_t, shown in Fig. 4.18, gives an activation energy E_t of 2.2 eV, in good agreement with the E_a of 2.1 eV obtained in the current experiment. However, reports of metal-induced germanium crystallization have indicated values of E_t dramatically less than 2.2 eV [30, 32]. In particular, Edelman *et al.* showed that 50 nm a-Ge covered with 120 nm Al or 20 nm Au crystallized

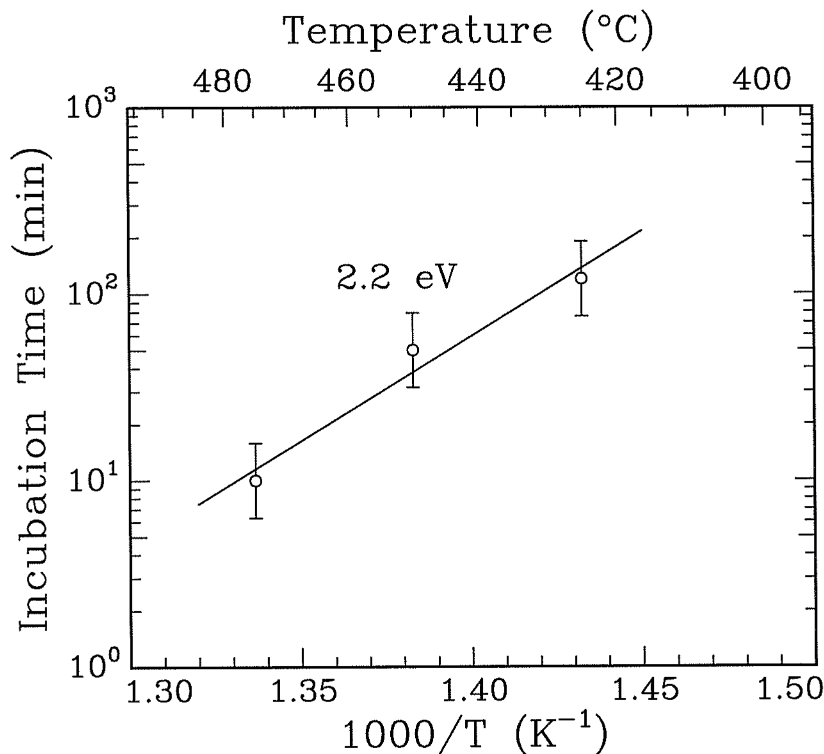

Figure 4.18: Incubation time for crystal nucleation in 20 nm and 50 nm pure amorphous Ge at various temperatures.

between 200 °C and 300 °C, with an activation $E_t = 0.9$ eV. Because $E_t \approx E_a$, this implies that the microscopic mechanism for crystal growth in metal-covered amorphous Ge is different from that in pure amorphous Ge. The same conclusion can also be drawn from the current experimental data: using the E_a (2.1 eV) and v_0 of the lateral SPE rate of undoped Ge films obtained in Fig. 4.15, a crystal growth distance d_{spe} of 7×10^{-4} nm is calculated for a 20 min anneal at 225 °C; even assuming that v_0 was increased by a factor of 66—the largest observed for the well-studied Si SPE [38]—by the presence of In or Au, $d_{spe} = 0.05$ nm, which is much too small to account for the 10–50 nm Ge crystals found in amorphous Ge films covered with a blanket Au or In thin film and annealed at 225 °C for 20 min. Therefore, growth of the crystals could not have taken place at the c-a interfaces. On the other hand, a low activation energy mechanism for crystal growth, one which only operates when Ge is in direct contact with Au or In clusters, can explain why the crystal sizes are directly

correlated to the sizes of the Au or In spots above them, as shown in Figs. 4.7, 4.8, and 4.9. In short, any possible mechanism for Ge crystal growth under metal covered areas must satisfy the following requirements: (a) sufficiently active below 300 °C, possibly due to a low activation energy, and (b) can only operate when Ge is in direct contact with metal clusters. At least one mechanism which satisfies the two above requirements has been observed by *in-situ* transmission electron microscopy, namely, diffusion of Ge atoms from amorphous Ge through an intermediate metal layer to the growing crystal. For example, as mentioned previously, Konno and Sinclair [33] have observed (at 270 °C) in Ag/a-Ge layered systems the migration of Ag grains into the interfaces between a-Ge and c-Ge and the subsequent motion of the grains toward a-Ge, leaving c-Ge behind; they showed that the interfaces between the Ag layers and the a-Ge layers remained almost perfectly smooth (no movement of Ag grains into a-Ge) in areas without c-Ge. Similarly, Lereah *et al.* [31] reported growth of Ge crystals in $Ge_{0.5}Al_{0.5}$ alloy at 250 °C by diffusion of Ge atoms from amorphous Ge through Al crystals into the Ge crystals. The above results can be understood through the following thermodynamic arguments: since c-Ge has lower free energy per atom than a-Ge, a difference in chemical potential exists between a-Ge and c-Ge; hence, a mass transfer from a-Ge to c-Ge is thermodynamically favored; however, transfer of atoms at the crystal-amorphous interface is kinetically inhibited at 200–300 °C due to a high activation energy for formation and migration of dangling bonds; however, grains in a metal layer can migrate partially into the boundary between c-Ge and a-Ge, to reduce the Ge crystal-amorphous interfacial energy, and in the process provide a fast reaction path for crystal growth via interdiffusion of the metal grains and amorphous Ge. (Indium melts at 156 °C, so transport of Ge atoms above this temperature should be very rapid inside In.) It is important to note that metals that form binary compounds with Ge can diffuse long distances into amorphous Ge in large quantities, inducing crystallization in areas far away from where the metals are initial deposited (as in the case of Cu), whereas metals that form eutectic phases with Ge can only induce crystallization directly below the elemental metals because they have relatively small solubilities in Ge (as in the case of In and Au). This is

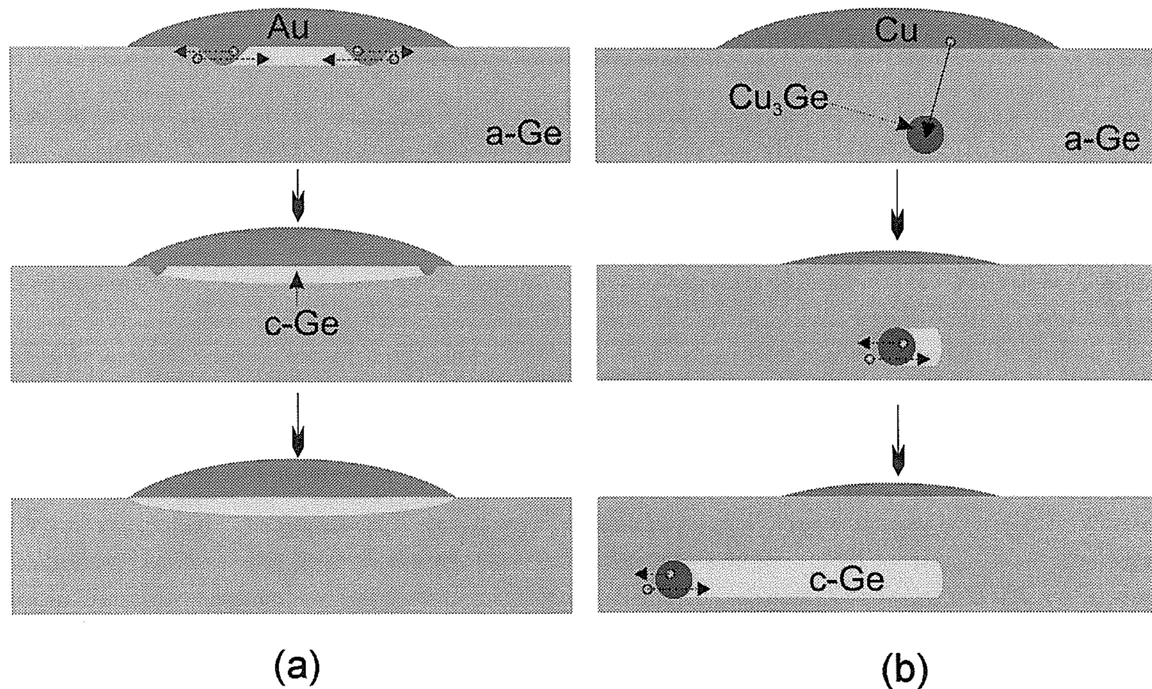

Figure 4.19: Illustration of possible mechanisms for metal-induced crystallization in Ge: (a) metals which form eutectics with Ge, such as Au and In, and (b) metals which form germanides, such as Cu and Ti. Metals can induce crystallization by (1) providing heterogeneous nucleation sites, and (2) enhancing crystal growth rate by dissolving surrounding amorphous Ge and transporting it to the crystals. Eutectic-forming metals can induce crystallization only in areas beneath them, because of their low solubilities in Ge. Germanide-forming metals can induce crystallization in areas not in direct contact with the elemental metals, because diffusion of these metals into amorphous Ge to form binary compounds is energetically favorable.

illustrated in Fig. 4.19.

4.4.2 Possible methods for obtaining one crystal per nucleation site

Currently each nucleation site produces more than one crystal, due to the fact that the In island is discontinuous. The size of a crystal in a nucleation site is the same as the size of the In spot above the crystal, as Fig. 4.9 shows, suggesting that an In island consisting of a single continuous film might produce one crystal of the same size underneath. From Fig. 4.9 it is clear that the edge of an In island has smaller spots, because the film thickness is smaller near the island edge. The variation in

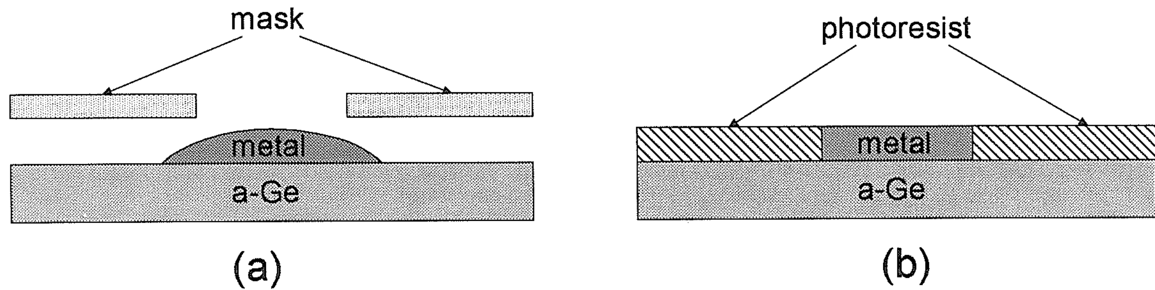

Figure 4.20: Scenarios of In island deposition on amorphous Ge. In (a), the current method, where the mask is not in intimate contact with the Ge thin-film, resulting in decreased film thickness near island edge, making it discontinuous. In (b), formation of In island via photolithography, which should result in uniform film thickness, and hopefully result a continuous film.

In film thickness is probably due to the fact that the mechanical mask was not in intimate contact with the amorphous Ge film during In deposition. This implies that even if the center of the island was continuous (perhaps by evaporating thicker films so that the spots agglomerate), the edge of the island would still be discontinuous. However, it might be possible to use photolithography to produce a thick ($>$ 100 nm), continuous In islands with uniform thickness, as illustrated in Fig. 4.20. Another way of producing a continuous metal island might be to use a different metal, one that would wet the amorphous Ge surface instead of bead up like the In film.

Another promising approach for producing a single crystal per nucleation site, similar to one which has been tried successfully in liquid phase recrystallization of Si [45], is to selectively remove amorphous Ge in order to block the growth of most of the crystals growing radially outward from the In island, as illustrated in Fig. 4.21. The idea is to etch away a pattern of amorphous Ge around the In island, like a moat around a castle, so that only one crystal can “escape” through an opening in the “moat”. This crystal then becomes the seed for subsequent growth.

4.4.3 Methods for increasing ultimate grain size

There are two possible ways to increase the grain size that can be obtained with the current method of selective crystallization: (1) reduce the random heterogeneous nucleation rate; and (2) increase the crystal growth rate even further. Cross-sectional

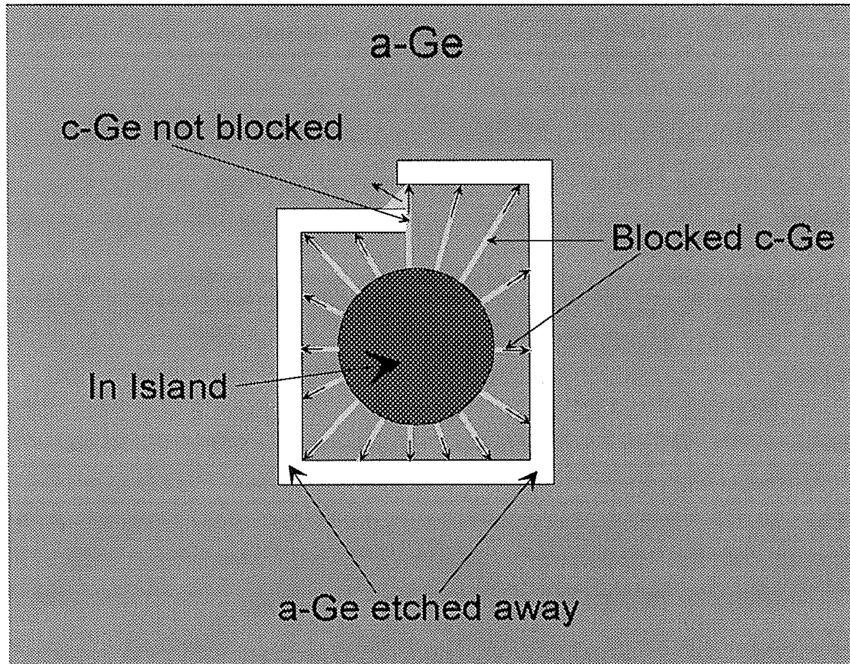

Figure 4.21: Illustration of Ge crystal seed selection by patterned removal of amorphous Ge. The white area is the portion of amorphous Ge film etched away. Crystals growing radially from the In island will be stopped when they reach these areas. Only one Ge crystal will escape through the opening and act as the crystal seed.

transmission electron microscopy can be performed on samples containing randomly nucleated crystals to determine the source of the random nucleation, i.e., free surface, film/substrate interface, or others. Then methods for passivating the source can be investigated. Crystal growth rate might be improved further by using heavier concentration of P, or using another dopants such as As or Al. In fact, heavier concentration of P or other dopants can be used as long as the dopant does not induce heterogeneous nucleation, possibly by precipitation or generation of defects in Ge.

4.5 Summary

In summary, selective solid phase crystallization has been shown to lead to grain sizes as large as 10–20 μm in undoped 50-nm-thick Ge films at temperatures less than 475 °C, for a grain-size-to-film-thickness aspect ratio of 400:1. It has been demonstrated

that a further increase in grain size by a factor of 10 can be achieved by doping with 0.7 at. % of P, which would lead to a grain size of more than 100 μm, representing a 3 orders of magnitude improvement over previous efforts. Dopant enhancement and dopant compensation of SPE rate in Ge has been shown for the first time, using B and P doping. Selective nucleation by metal-induced crystallization does not at present lead to growth of a single crystal per nucleation site. Nonetheless, the results indicate that the present method of selective solid phase crystallization is a simple process for achievement of large grain sizes that is compatible with the use of low-cost substrates.

Bibliography

[1] A. G. Fisher, D. J. Tizabi, and H. Blanke, IEEE Elec. Dev. Lett. **4**, 447 (1983).

[2] S. S. Chu, T. L. Chu, and Y. X. Han, J. Appl. Phys. **20**, 811 (1986).

[3] S. P. Tobin, S. M. Vernon, C. Bajgar, V. E. Haven, L. M. Geoffroy, and D. R. Lillington, IEEE Elec. Dev. Lett. **9**, 256 (1988).

[4] Y. Ohmachi, T. Nishioka and Y. Shinoda, Appl. Phys. Lett. **43** 971 (1983).

[5] T. Okabe, Y. Kagawa, and S. Takai, Phil. Mag. Lett. **65**, 233 (1991).

[6] M. Yamaguchi and Y. Itoh, J. Appl. Phys. **60**, 413 (1986).

[7] R. Reif, and J. E. Knott, Elec. Lett. **17**, 586 (1981).

[8] K. T-Y. Kung, R. B. Iverson, and R. Reif, Appl. Phys. Lett. **46** 683 (1985).

[9] J. S. Im, J. H. Shin, and H. A. Atwater, Appl. Phys. Lett. **59**, 2314 (1991).

[10] C. Spinella, S. Lombardo, and S. U. Campisano, Appl. Phys. Lett. **55**, 109 (1989).

[11] K. Oyoshi, T. Yamaoka, T. Tagami, and Y. Arima, J. Appl. Phys. Lett. **71**, 648 (1991).

[12] J. S. Im and H. A. Atwater, Appl. Phys. Lett. **57**, 1766 (1990).

[13] H. Kumomi and T. Yonehara, Appl. Phys. Lett. **59**, 3565 (1991).

[14] H. Kumomi and T. Yonehara, Appl. Phys. Lett. **54** 2648 (1989).

[15] M. Moniwa, M. Miyao, R. Tsuchiyama, A. Ishizaka, M. Ichikawa, H. Sunami, and T. Tokuyama, Appl. Phys. Lett. **47**, 113 (1985).

[16] Gang Liu and S. J. Fonash, Appl. Phys. lett. **55**, 660 (1989).

[17] T. J. Konno and R. Sinclair, Mater. Sci. and Eng. **A179**, 426 (1994).

[18] S. W. Lee, Y. C. Jeon, and S. K. Joo, Appl. Phys. Lett. **66**, 1671 (1995).

[19] S. W. Lee, private communication, fall MRS, 1995.

[20] S. W. Lee and S. K. Joo, IEEE Elec. Dev. Lett. **17**, 160 (1996).

[21] F. Oki, Y. Ogawa, Japan. J. Appl. Phys. **8** 1056 (1969).

[22] J. Bosnell and U. Voisey, Thin Solid Films **6** 161 (1969).

[23] S. W. Russell, J. Li, and J. W. Mayer, J. Appl. Phys. **70**, 5153 (1991).

[24] C. Hayzelden, J. Batsone, and R. Cammarta, Appl. Phys. Lett. **60** 255 (1992).

[25] E. Nygren, A. P. Pogany, K. T. Short, and J. S. Williams, Appl. Phys. Lett. **52**, 439 (1988).

[26] G. Radnoczi, A. Robertsson, H. T. G. Hentzell, S. F. Gong, and M.-A. Hasan, J. Appl. Phys. **69**, 6394 (1991).

[27] J. S. Custer, M. O. Thompson, D. J. Eaglesham, D. C. Jacobson, and J. M. Poate., J. Mater. Res. **8**, 820 (1992).

[28] F. Oki, Y. Ogawa, and Y. Fujiki, Jpn. J. Appl. Phys. **8**, 1056 (1969).

[29] D. Smith, C. Grovenor, P. Batson, and C. Wong, Ultramicroscopy **14**, 131 (1984).

[30] F. Edelman, Y. Komem, M. Bendayan, and R. Beserman, J. Appl. Phys. **72**, 5153 (1992).

[31] Y. Lereah, J. M. Penisson and A. Bourret, Appl. Phys. Lett. bf 60, 1682 (1992).

[32] Z. Renji, L. Li, and Wu Ziqin, J. Mater. Sci. **28**, 1705 (1993).

[33] T. J. Konno and R. Sinclair, Mat. Res. Soc. Symp. Proc. *311*, 99 (1993).

[34] Z. Tan, S. Heald, M. Rapposch, E. Bouldin, and J. Woicik, Phys. Rev.B **46**, 9505 (1992).

[35] F. Edelman, C. Cytermann, R. Brener, M. Eizenverg, R. Weil, and W. Beyer, Appl. Surf. Sci. **70**, 722 (1992).

[36] C. Hayzelden, J. L. Batstone, J. Appl. Phys. **73**, 8279 (1993).

[37] M. Moniwa, K. Kusukawa, E. Murakami, T. Warabisako, and M. Miyao, Appl. Phys. Lett. **52**, 1788 (1988).

[38] G. L. Olson and J. A. Roth, in *Handbook of Crystal Growth*, edited by D. T. J. Hurle (Elsevier, Amsterdam, 1994), Chap. 7, pp. 256-311.

[39] G. Q. Lu, E. Nygren, and M. J. Aziz, J. Appl. Phys. **70**, 5323 (1991).

[40] F. Spaepen and D. Turnbull, AIP Conf. Proc. **50**, 73 (1979).

[41] J. S. Williams and R. G. Elliman, Phys. Rev. Lett. **51**, 1069 (1983).

[42] A. L. Greer, P. V. Evans, R. G. Hamerton, D. K. Shangguan, and K. F. Kelton, J. Cryst. Growth **99**, 38 (1990).

[43] D. Kashchiev, Surf. Sci. **14**, 209 (1969).

[44] R. B. Iverson and R. Reif, J. Appl. Phys. **62**, 1675 (1987).

[45] H. A. Atwater, H. I. Smith, and M. W. Geis, Appl. Phys. Lett. **41**, 747 (1982).

Appendix A Program for Calculating Crystal Evolution Under Ion Irradiation

A.1 Description

The program used in Ch. 2 to calculate the evolution of crystal size distribution under ion irradiation is shown below. It is written in ANSI C. It accepts a text file containing two columns of data, the first column being the radius r and the second column being the population f:

```
r0    f0
r1    f1
r2    f2
..    ..
..    ..
```

Note that the spacing between the radii must be constant: $r1 - r0 = r2 - r1$, and so on.

A.2 Source code

```
#include <stdio.h>
#include <stdlib.h>
#include <string.h>
#include <sys/types.h>
#include <math.h>

#define MAXBINS 400

#define FILES 4
/* total no. of files for storing f vs. r. */

#define XX .1
```

```
/* constant used in the equation relating dt and dr */

/* The following constants are used in setting filename extensions and
   other stuff.  For example, FILENAME_EXT is appended to the filenames
   that the user choose to store the files of f vs. r in.  If the user
   specifies 'log' for filename, then f vs. r will be stored in files
   'logxx.rf'. */

#define FILENAME_EXT "xx.txt"
#define FILEDIGITS 2
#define NAME_LENGTH 32

long bins;
char buf[256];
double f[MAXBINS], *g, radius[MAXBINS], *drdt;
double *ftmp, *gtmp, *rtmp, *drdttmp, dr;
double Lambda, N0, N1, phi, sigma2, sigma, v0, Em, kT, Gv, Va;
double t0, a0, l0, const_rate;
double Ej(double r);
double vf(double r);
double vb(double r);
double v1(double r);
double v2(double r);
double G(double r);
double A(double r);
double logterm(double r);
double rate(double r);
void recalc_var(void);
void setup_filenames(char *filenames[], char *name, int files);
void write_file(char *filename, double t);
void setvar(char *name);
void free_filenames(char *filenames[], int n);
void setup_input(char *fn);

struct variable
{
    char  name[2];
    double *var;
};

struct variable varlist[] =
{
    "La", &Lambda, "N1", &N1, "ph", &phi, "s2", &sigma2, "s1", &sigma,
    "v0", &v0, "Em", &Em, "kT", &kT, "Gv", &Gv, "Va", &Va, "a0", &a0,
    "cr", &const_rate, "l0", &l0
};

#define NVARS (sizeof(varlist) / sizeof(struct variable))

main(int argc, char *argv[])
{
    char *filenames[FILES];
    long iterations, i, iperfile, file_count;
```

```
    double t, dt, duration;
    double dtdr, f1, f2, f3, ff;
    int j;

    if (argc < 4)
    {
        printf("Usage:\n\tibiec input_file time filename "
               "[var1=? var2=? ...]\n");
        printf("Example:\n\tibiec ion 250 log N0=1 La=2 ph=3\n");
        exit(0);
    }

/* The following are the default values for the variables Lambda, N1,
   etc.  If the user does not assign a value to a variable, then
   the default value for that variable will be used in the program. */

    Lambda = 1e-23;
    l0 = .17e-12;
    N1 = .5e8;
    N0 = N1/10;
    phi = 1e12;
    sigma2 = 2.93e-15;
    sigma = 4.8e-5;
    v0 = 4.265e15;
    Em = 1.922e-19;
    kT = 6.117e-21;
    Gv = 801.000;
    Va = .15e-20;
    t0 = 1/l0/phi;
    a0 = 5.43e-8;
    const_rate = 0.0;

/* set the variables from the strings on the command line
   For example, the function setvar() takes the string "Em=3.14" and sets
   the variable Em to 3.14 */

    for (i = 4; i < argc; i++)
       setvar(argv[i]);

    recalc_var();

    duration = atof(argv[2]);

    setup_filenames(filenames, argv[3], FILES);
    setup_input(argv[1]);

    t = 0.0;
    file_count = 0;

    dt = fabs(-XX * dr / rate(radius[0]));
    dtdr = dt / dr;

    iterations = (long)(duration / dt);
```

```
iperfile = iterations / FILES;

for (i = 0; i < iterations; i++)
{
    for (j = 0; j < bins; j++)
        g[j] = f[j] * drdt[j];

    for (j = 0; j < bins - 1; j++)
    {
        if (drdt[j] > 0)
        {
            if (j == 0)
                f1 = 0;
            else
                f1 = f[j] + .5 * (f[j] - f[j-1]);
            f2 = .5 * (f[j] + f[j+1]);
            f3 = f[j];
            if (f[j+1] <= f[j])
                ff = min(f3, max(f1, f2));
            else
                ff = max(f3, min(f1, f2));
        }
        else
        {
            f1 = f[j+1] + .5 * (f[j+1] - f[j+2]);
            f2 = .5 * (f[j] + f[j+1]);
            f3 = f[j+1];
            if (f[j+1] <= f[j])
                ff = max(f3, min(f1, f2));
            else
                ff = min(f3, max(f1, f2));
        }
        ftmp[j] = ff - .5 * dtdr * (g[j+1] - g[j]);
    }

    for (j = 0; j < bins; j++)
        gtmp[j] = ftmp[j] * drdttmp[j];

    for (j = 1; j < bins - 1; j++)
    {
        f[j] = f[j] - dtdr * (gtmp[j] - gtmp[j-1]);
        if (f[j] < 0.0)
            f[j] = 0.0;
    }

    t = (i+1) * dt;

    if (((i+1) % iperfile) == 0)
    {
        write_file(filenames[file_count], t);
        file_count++;
    }
}
```

```
    free_filenames(filenames, FILES);
    return(0);
}


/*
    setup_filenames() initializes filenames to be used for storing files of
    f(r) vs. r.
*/
void setup_filenames(char *filenames[], char *name, int files)
{
    int i;
    char number[NAME_LENGTH];

    for (i = 0; i < files ; i++)
    {
        filenames[i] = (char *) malloc(NAME_LENGTH);
        number[1] = '0' + (i+1) % 10;
        number[0] = '0' + (i+1) / 10;
        strcpy(filenames[i], name);
        strcpy(filenames[i] + strlen(name), FILENAME_EXT);
        strncpy(filenames[i] + strlen(name), number, FILEDIGITS);
    }
}


#define RFHEADER "/* \tr\t\tf(r)\n"
/*
    write_file() stores f(r) vs. r in a file.
*/
void write_file(char *filename, double t)
{
    int i;
    FILE *stream;

    stream = fopen(filename, "w+");
    fprintf(stream, "/* t = %-14.8g\n", t);
    fprintf(stream, RFHEADER);

    for (i = 0; i < bins; i++)
        fprintf(stream, "%-16.8g\t%-16.8g\n", radius[i], f[i]);

    fclose(stream);
}


double Ej(double r)
{
    return ((-Gv+2*sigma/(r/1e7))*Lambda);
}


double vf(double r)
```

```
{
    return (v0*exp(-(Em+.5*Ej(r))/kT));
}


double vb(double r)
{
    return(v0*exp(-(Em-.5*Ej(r))/kT));
}


double v1(double r)
{
    return(vf(r)-vb(r));
}


double v2(double r)
{
    return(vf(r)+vb(r));
}


double G(double r)
{
    return(N0*sigma2*a0*t0*v2(r));
}


double A(double r)
{
    return(Lambda*l0*phi/sigma2*(v1(r)/v2(r)));
}


double logterm(double r)
{
    return(log(1+G(r)/2*(1+sqrt(1+4/G(r)))));
}


double rate(double r)
{
    if (const_rate != 0.0)
        return (const_rate);
    else
        return((A(r)*logterm(r)-Va*phi)*1e7);
}


void recalc_var()
{
    N0 = N1/l0;
```

```
    t0 = 1/10/phi;
}


#define MAXLINE 256
/*
    setup_input() sets up a distribution for f(r) by reading the file 'fn'.
*/
void setup_input(char *fn)
{
    FILE *fp;
    char line[MAXLINE];
    int i;

    fp = fopen(fn, "r");
    if (fp == NULL)
    {
        printf("Cannot open input file!\n");
        exit(1);
    }

    i = 0;
    while (fgets(line, MAXLINE, fp) != NULL && i < MAXBINS)
    {
        if (sscanf(line, "%lf %lf", &radius[i], &f[i]) == 2)
            ++i;
    }
    fclose(fp);
    bins = i;

    dr = radius[1] - radius[0];
    i +=5;

    f[0] = 0.0;
    ftmp = (double *) malloc(i*sizeof(double));
    rtmp = (double *) malloc(i*sizeof(double));
    g = (double *) malloc(i*sizeof(double));
    gtmp = (double *) malloc(i*sizeof(double));
    drdt = (double *) malloc(i*sizeof(double));
    drdttmp = (double *) malloc(i*sizeof(double));
    for (i = 0; i < bins; i++)
    {
        if (f[i] < 0.0)
            f[i] = 0.0;
        rtmp[i] = radius[0] + (i+.5) * dr;
        drdt[i] = rate(radius[i]);
        drdttmp[i] = rate(rtmp[i]);
    }
}


/*
    free_filenames() frees the memory allocated for storing filenames.
```

```
*/
void free_filenames(char *filenames[], int n)
{
    int i;

    for (i = 0; i < n; i++)
        free(filenames[i]);
}


/*
    setvar() takes a string like "Em=3.14" and set the variable Em to 3.14
*/
void setvar(char *name)
{
    double value;
    int i;

    for (i = 0; i < NVARS; i++)
    if (name[0] == varlist[i].name[0] && name[1] == varlist[i].name[1])
    {
        value = *(varlist[i].var) = atof(&name[3]);
        printf("%c%c = %g\n", name[0], name[1], value);
        return;
    }
    if (i == NVARS)
    {
        printf("\nVariable %c%c not found!\n", name[0], name[1]);
        exit(0);
    }
}
```

Appendix B Program for Calculating Time-Dependent Nucleation

B.1 Introduction

A program for calculating time-dependent nucleation is described in this appendix. A description of the program is contained in Sec. B.2. Some sample outputs are shown in Sec. B.3. The numerical algorithm of the program is discussed in Sec. B.4, and the source code for the program is listed in Sec. B.5.

B.2 Description

The program calculates temporal evolution of nuclei size distribution using classical nucleation theory. The initial nuclei population is assumed to consist of only monomers. The program can compute the effect of (a) ion irradiation and (b) oscillating annealing temperature on the nucleation rate. Ion irradiation is modeled by assuming that nuclei containing fewer than r^* atoms are obliterated instantaneously at time t^*. The annealing temperature is assumed to oscillate between T_1 and T_2 with a square profile of period τ.

B.3 Sample outputs

Some sample plots of the outputs from the program is shown below. In each of these cases, the critical size for nucleation is 64 atoms. Figures B.1 and B.2 show the evolution of nuclei population and nuclei flux (in size space, which corresponds to nucleation rate), respectively, without ion irradiation or temperature oscillation. Figures B.3 and B.4 show the results of ion irradiation at $t^* = 200$ sec with $r^* = 64$

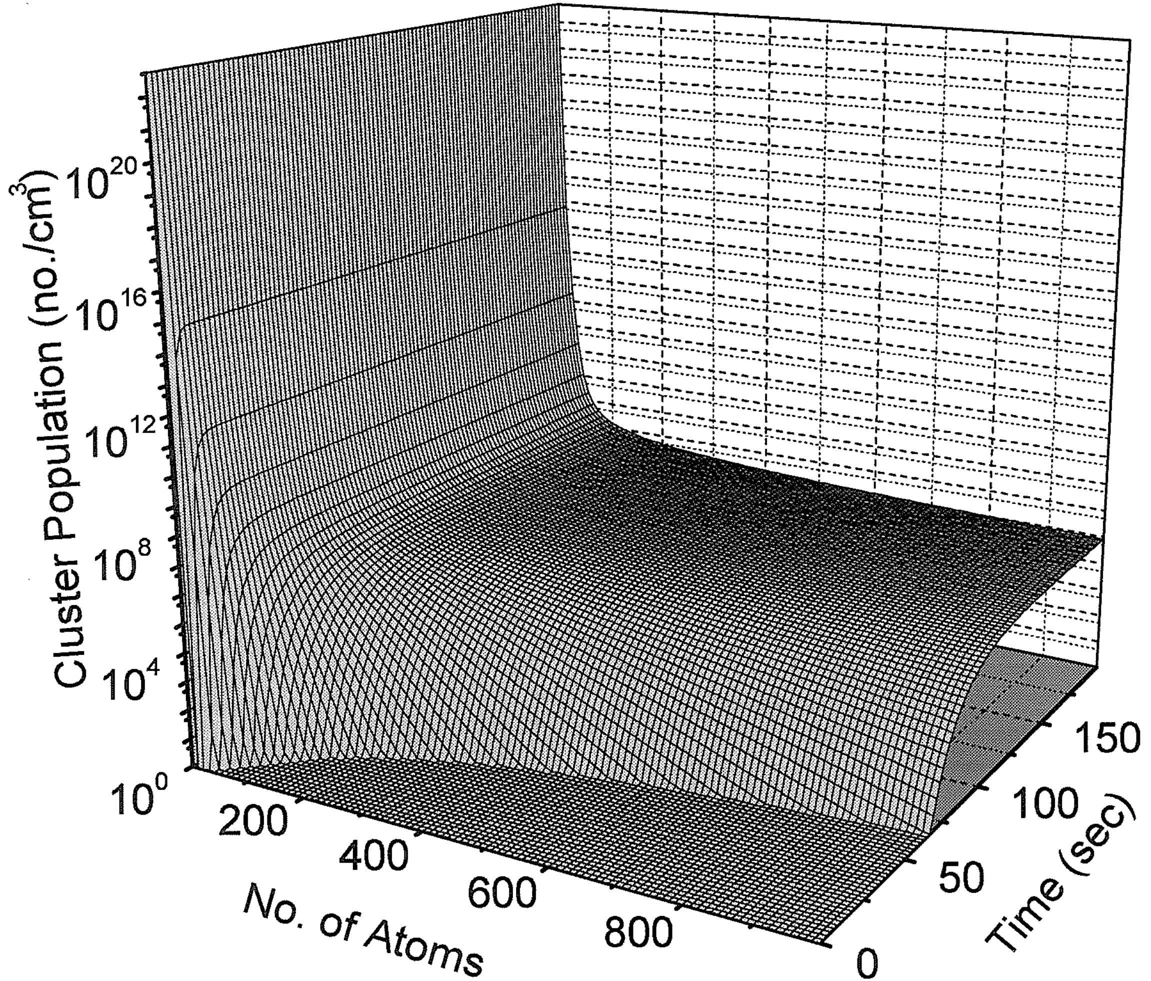

Figure B.1: Temporal evolution of nuclei population. No ion irradiation or temperature oscillation was assumed.

atoms. Similarly, Figs. B.3 and B.4 show the results of ion irradiation at $t^* = 200$ sec with $r^* = 400$ atoms. Finally, Fig. B.7 shows the nucleation rates during anneals with $T_1 = 600$ °C, $T_2 = 625$ °C, and $\tau = 4$ sec, 20 sec, 60 sec, or 80 sec.

B.4 Algorithm

The number of nuclei containing x to $x + dx$ atoms at time t, $W(x,t)$, is calculated using the Fokker-Planck equation:

$$\frac{\partial W(x,t)}{\partial t} = \frac{\partial}{\partial x}\left[\Gamma(x)\frac{\partial}{\partial x}\left(\frac{W(x,t)}{Z(x)}\right)\right] \tag{B.1}$$

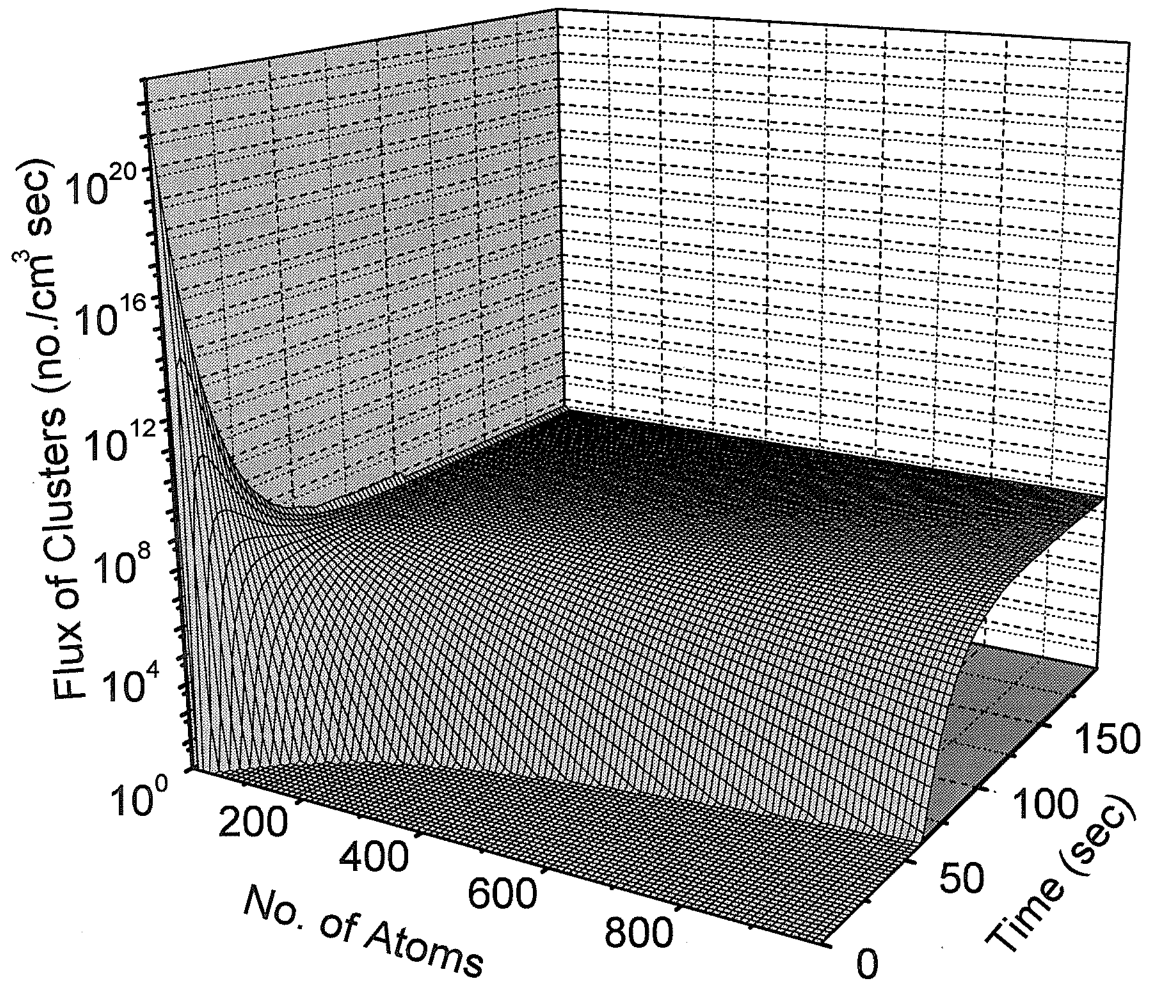

Figure B.2: Temporal evolution of nuclei flux. No ion irradiation or temperature oscillation was assumed.

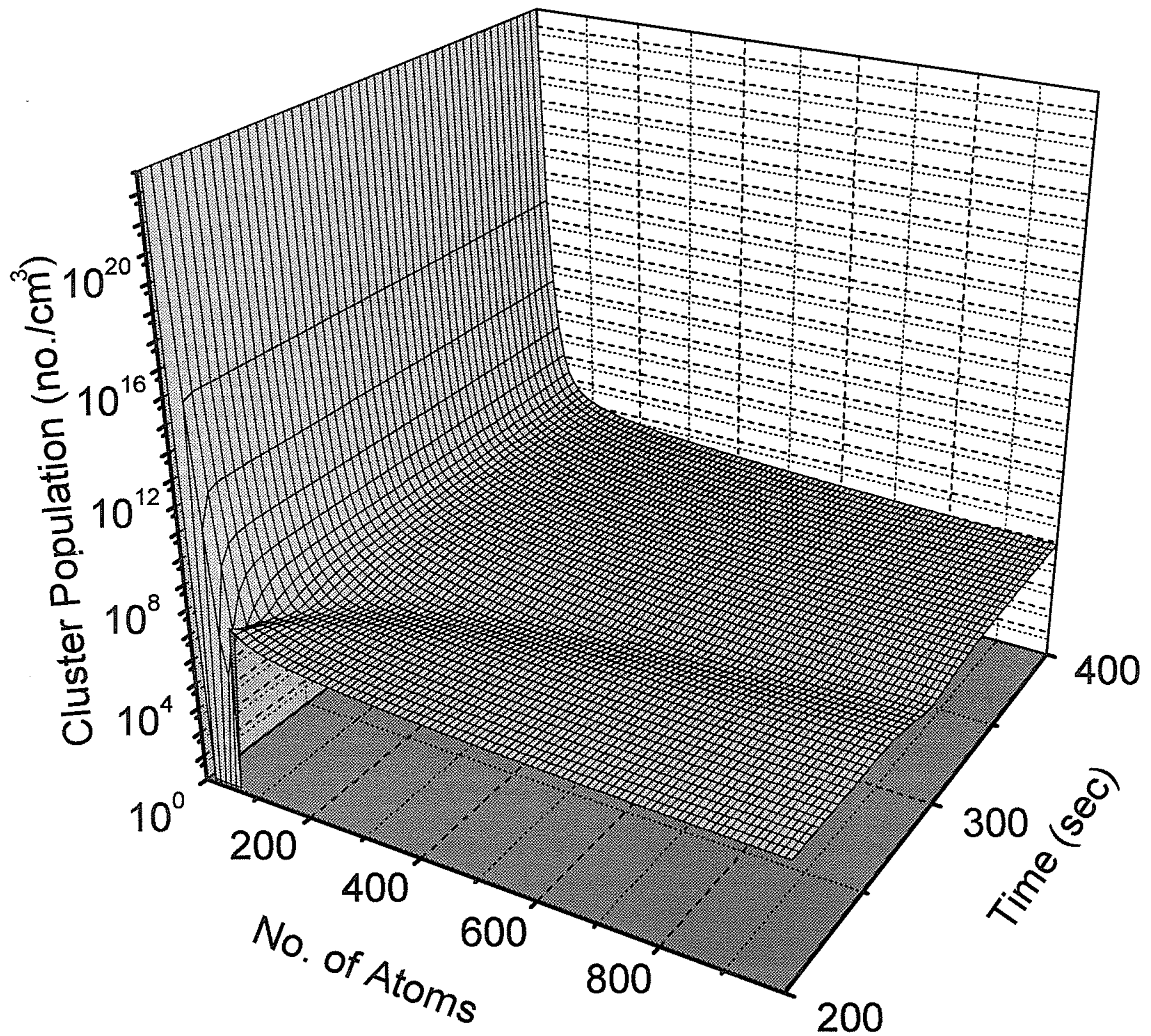

Figure B.3: Temporal evolution of nuclei population. r_* is 64 atoms, and t^* is 200 sec.

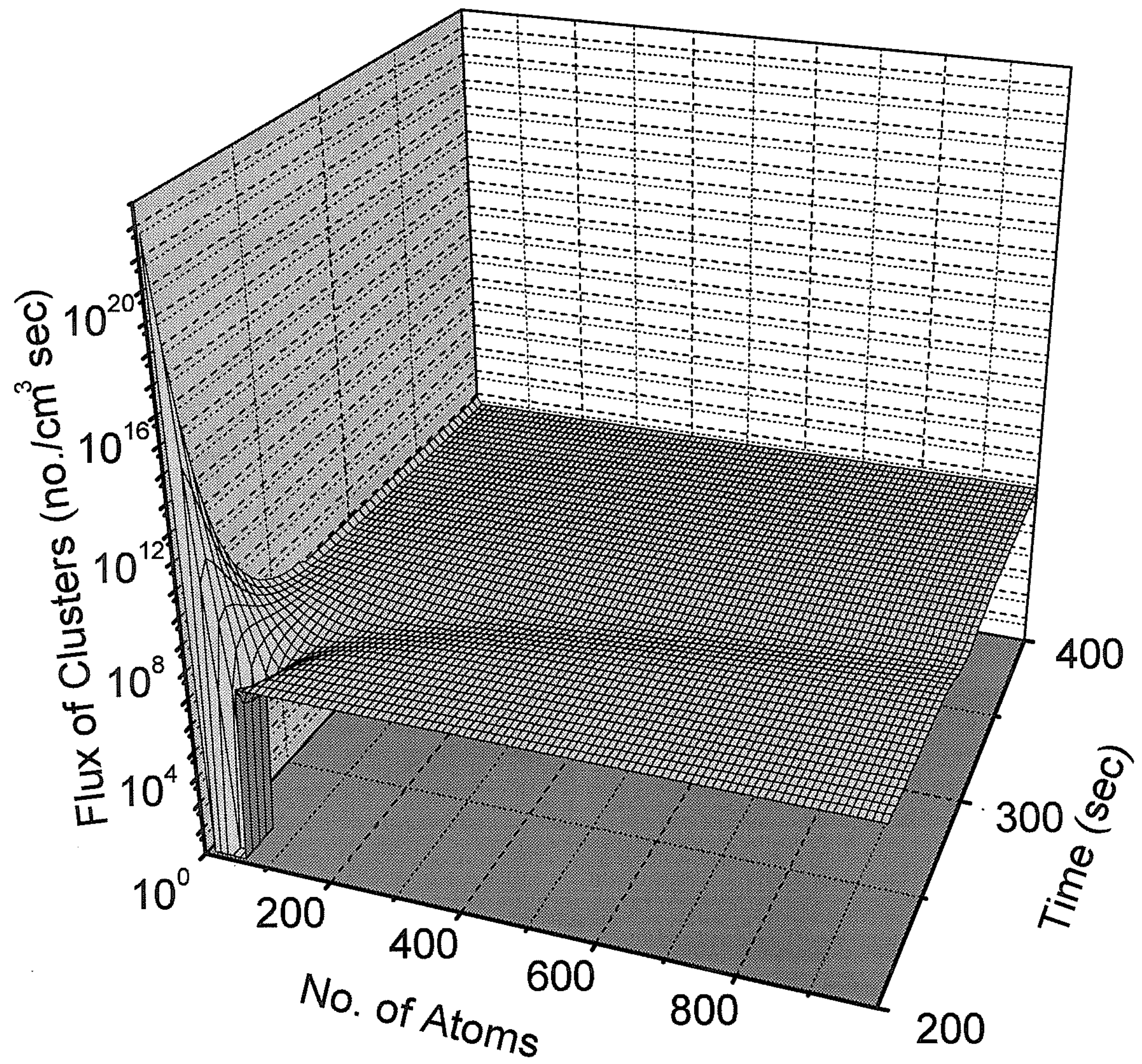

Figure B.4: Temporal evolution of nuclei flux. r_* is 64 atoms, and t^* is 200 sec.

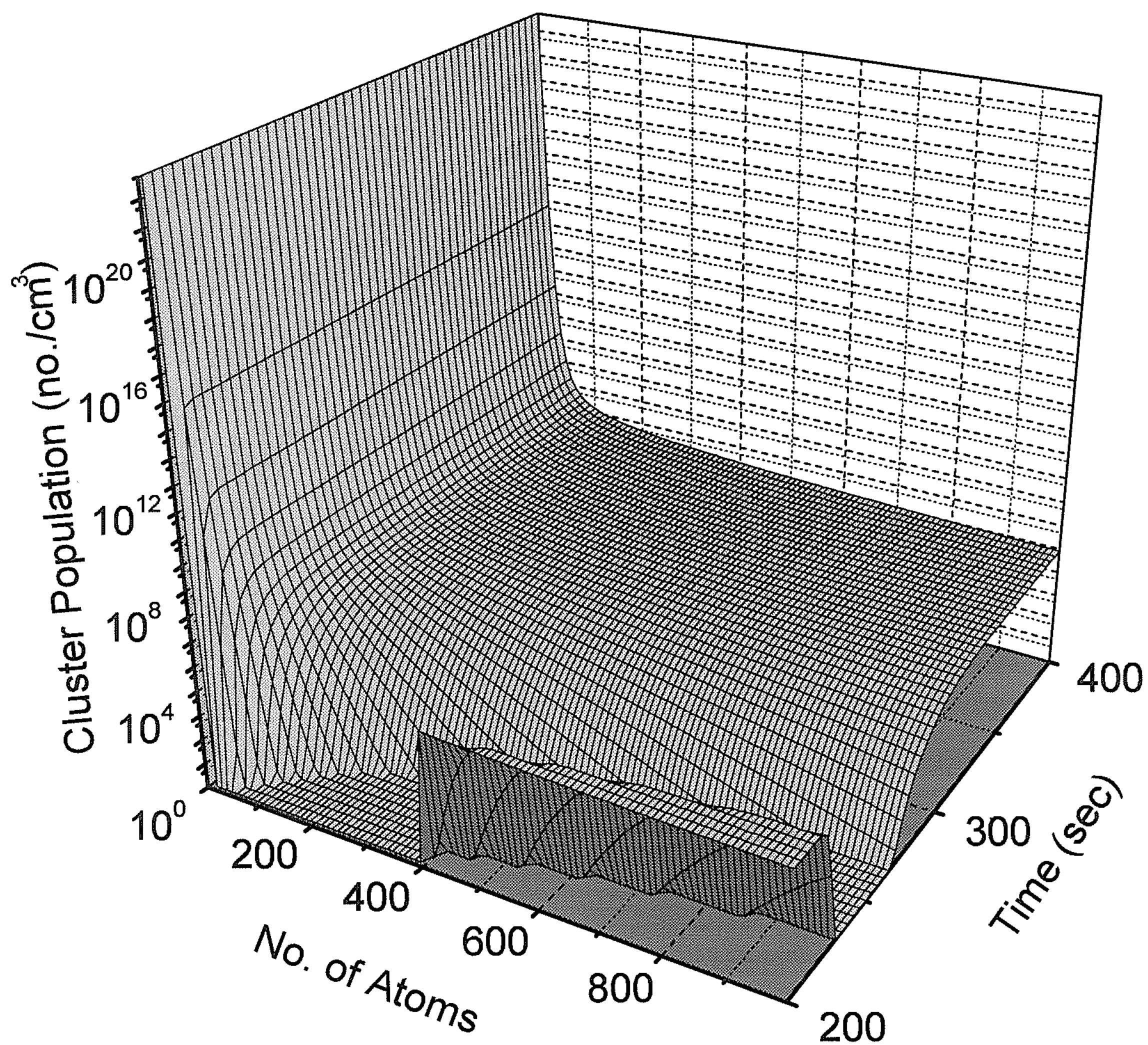

Figure B.5: Temporal evolution of nuclei population. r_* is 400 atoms, and t^* is 200 sec.

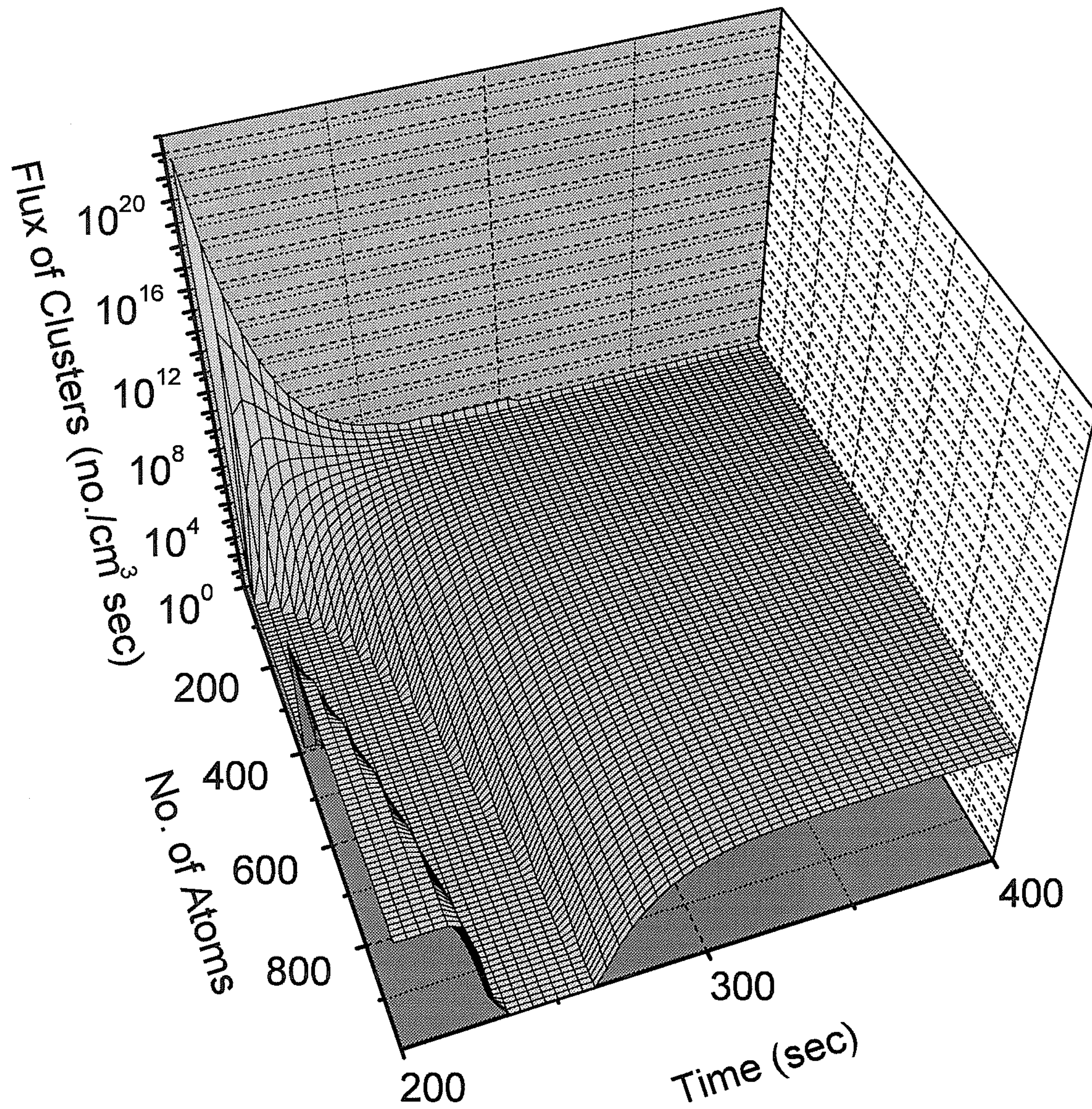

Figure B.6: Temporal evolution of nuclei flux. r_* is 400 atoms, and t^* is 200 sec.

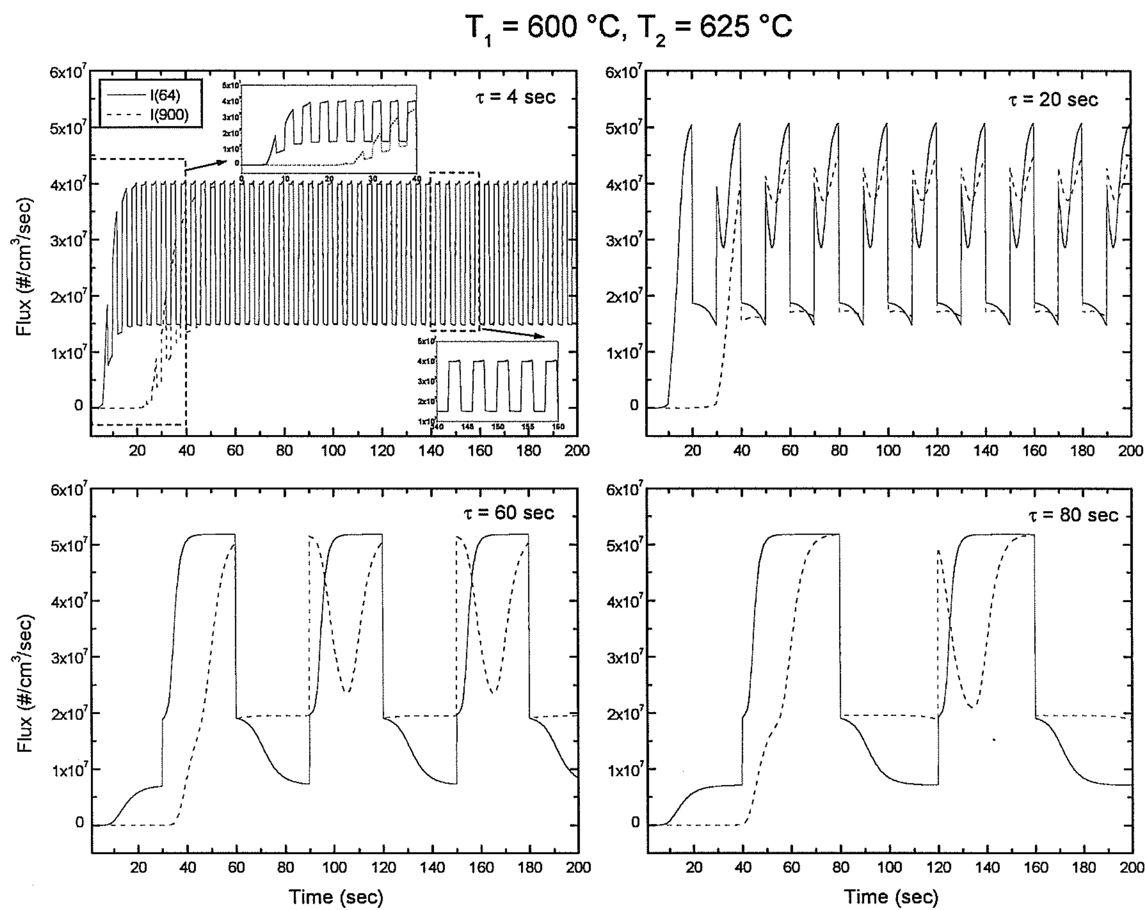

Figure B.7: Nucleation rate during temperature oscillation.

where

$$\Gamma(x) = \begin{cases} \beta(x)Z(x) & \text{Frenkel, Kaschev} \\ \beta(x-1/2)Z(x-1/2) & \text{Wu} \\ \frac{\alpha(x)+\beta(x)}{2}Z(x) & \text{Shizgal and Barret} \end{cases} \tag{B.2}$$

β and α are the forward and backward transition coefficients, respectively, and $Z(x)$ is the steady-state distribution:

$$\beta_n Z_n = \alpha_{n+1} Z_{n+1}. \tag{B.3}$$

Let

$$Y(x,t) = \frac{W(x,t)}{Z(x)}. \tag{B.4}$$

Then Eq. B.1 becomes

$$\frac{\partial W(x,t)}{\partial t} = \frac{\partial}{\partial x}\left[\Gamma(x)\frac{\partial Y(x,t)}{\partial x}\right]. \tag{B.5}$$

Taking the FTCS (forward-time center-space) discrete representation of the RHS we get

$$\frac{\partial W(x,t)}{\partial t} = \frac{1}{\Delta x}\left[\left(\Gamma(x)\frac{\partial Y(x,t)}{\partial x}\right)\Bigg|_{i+1/2}^{j} - \left(\Gamma(x)\frac{\partial Y(x,t)}{\partial x}\right)\Bigg|_{i-1/2}^{j}\right]. \tag{B.6}$$

where

$$x = i\Delta x \tag{B.7}$$

$$t = j\Delta t. \tag{B.8}$$

Thus,

$$\frac{\partial W(x,t)}{\partial t} = \frac{1}{(\Delta x)^2}\left[\Gamma_{i+1/2}^{j}(Y_{i+1}^{j} - Y_i^j) - \Gamma_{i-1/2}^{j}(Y_i^j - Y_{i-1}^{j})\right]. \tag{B.9}$$

The program uses the $\Gamma(x)$ given by Wu [1]; of the different forms that have been proposed for $\Gamma(x)$, his is the most accurate. To see this, take $\Delta x = 1$. Then the

above equation becomes

$$\frac{\partial W(x,t)}{\partial t} = \Gamma(x+1/2)[Y(x+1)-Y(x)] - \Gamma(x-1/2)[Y(x)-Y(x-1)]. \quad \text{(B.10)}$$

Substituting $\Gamma(x) = \beta(x-1/2)Z(x-1/2)$ into Eq. B.10 we obtain

$$\frac{\partial W(x,t)}{\partial t} = \beta(x)Z(x)[Y(x+1)-Y(x)] - \beta(x-1)Z(x-1)[Y(x)-Y(x-1)]. \quad \text{(B.11)}$$

Using Eq. B.3 and 4 we get

$$\frac{\partial W(x,t)}{\partial t} = \alpha(x+1)W(x+1) - \beta(x)W(x) - \alpha(x)W(x) + \beta(x-1)W(x-1). \quad \text{(B.12)}$$

This is exactly the master equation that governs the growth and decay of clusters with discrete sizes (x has only integral values). Thus, for the case of $\Delta x = 1$, Eq. B.1 is equivalent to the original discrete master equation, provided that we take $\Gamma(x) = \beta(x-1/2)Z(x-1/2)$. To solve Eq. B.1 numerically, take the finite difference of LHS of Eq. B.9. We get

$$Z_i\left(\frac{Y_i^{j+1} - Y_i^j}{\Delta t}\right) = \frac{1}{(\Delta x)^2}\left[\Gamma_{i+1/2}^j (Y_{i+1}^j - Y_i^j) - \Gamma_{i-1/2}^j (Y_i^j - Y_{i-1}^j)\right]. \quad \text{(B.13)}$$

We can solve this equation directly; however, the resulting stability requirement will make the timestep too small. We can overcome this problem by transforming the right hand side using the Crank-Nicholson method [2]. That is, we take the average value of RHS at time step j and $j+1$.

$$\begin{aligned} Z_i\left(\frac{Y_i^{j+1} - Y_i^j}{\Delta t}\right) &= \frac{1}{2(\Delta x)^2}\left[\Gamma_{i+1/2}^{j+1}(Y_{i+1}^{j+1} - Y_i^{j+1}) - \Gamma_{i-1/2}^{j+1}(Y_i^{j+1} - Y_{i-1}^{j+1})\right. \\ &\quad \left. +\Gamma_{i+1/2}^j (Y_{i+1}^j - Y_i^j) - \Gamma_{i-1/2}^j (Y_i^j - Y_{i-1}^j)\right]. \end{aligned} \quad \text{(B.14)}$$

Let

$$L_i = \frac{\Delta t}{2(\Delta x)^2}\Gamma_i. \quad \text{(B.15)}$$

Then

$$-L_{i-1/2}Y_{i-1}^{j+1} + (Z_i + L_{i-1/2} + L_{i+1/2})Y_i^{j+1} - L_{i+1/2}Y_{i+1}^{j+1} =$$
$$L_{i-1/2}Y_{i-1}^{j} + (Z_i - L_{i-1/2} - L_{i+1/2})Y_i^{j} + L_{i+1/2}Y_{i+1}^{j}. \quad \text{(B.16)}$$

Now the LHS contains Y's at timestep $j+1$ (to be calculated) whereas the RHS contains Y's at timestep j (which are known). To see if the Crank-Nicholson scheme is stable, perform the von Neumann stability analysis [2] by writing

$$Y_i^j = \xi^j e^{Iki\Delta x}, \quad \text{(B.17)}$$

where $I = \sqrt{-1}$. The above solution is stable if $|\xi| \leq 1$. Substituting Eq. B.17 into Eq. B.16 we get

$$\xi^{j+1}[-L_{i-1/2}e^{-Ik\Delta x} + (Z_i + L_{i-1/2} + L_{i+1/2}) - L_{i+1/2}e^{+Ik\Delta x}]e^{Iki\Delta x} =$$
$$\xi^{j}[L_{i-1/2}e^{-Ik\Delta x} + (Z_i - L_{i-1/2} - L_{i+1/2}) + L_{i+1/2}e^{+Ik\Delta x}]e^{Iki\Delta x}. \quad \text{(B.18)}$$

So the propagation amplitude ξ becomes

$$\xi = \frac{Z_i - L_{i-1/2}S - L_{i+1/2}S + I(L_{i+1/2} - L_{i-1/2})\sin(k\Delta x)}{Z_i + L_{i-1/2}S + L_{i+1/2}S - I(L_{i+1/2} - L_{i-1/2})\sin(k\Delta x)}, \quad \text{(B.19)}$$

where

$$S = 1 - \cos(k\Delta x). \quad \text{(B.20)}$$

To simplify the expression for ξ, write it as

$$\xi = \frac{p + Iq}{r - Iq}, \quad \text{(B.21)}$$

where p, q, and r are real. Since

$$L_i \geq 0, \quad \text{(B.22)}$$

$$1 - \cos(k\Delta x) \geq 0, \quad \text{(B.23)}$$

and

$$Z_i \geq 0 \tag{B.24}$$

for all i, k and Δx,

$$|r| \geq |p|. \tag{B.25}$$

Thus,

$$|\xi| \leq 1. \tag{B.26}$$

So the Crank-Nicholson method produces an unconditionally stable difference equation. To solve for Y_i^{j+1} we write Eq. B.16 as:

$$B_1 T_1 + C_1 T_2 = D_1 \tag{B.27}$$

$$A_i T_{i-1} + B_i T_i + C_i T_{i+1} = D_i \tag{B.28}$$

$$A_M T_{M-1} + B_M T_M = D_M. \tag{B.29}$$

This can be turned into a matrix equation:

$$\begin{pmatrix} B_1 & C_1 & 0 & . & . & 0 & 0 & 0 \\ A_2 & B_2 & C_2 & . & . & 0 & 0 & 0 \\ 0 & A_3 & B_3 & . & . & 0 & 0 & 0 \\ . & . & . & & & . & . & . \\ . & . & . & & & . & . & . \\ 0 & 0 & 0 & . & . & A_{M-1} & B_{M-1} & C_{M-1} \\ 0 & 0 & 0 & . & . & 0 & A_M & B_M \end{pmatrix} \begin{pmatrix} T_1 \\ . \\ . \\ . \\ . \\ . \\ T_M \end{pmatrix} = \begin{pmatrix} D_1 \\ . \\ . \\ . \\ . \\ . \\ D_M \end{pmatrix}; \tag{B.30}$$

where

$$A_i = -L_{i-1/2} \tag{B.31}$$

$$B_i = Z_i + L_{i-1/2} + L_{i+1/2} \tag{B.32}$$

$$C_i = -L_{i+1/2} \tag{B.33}$$

$$D_i = L_{i-1/2} Y_{i-1}^j + (Z_i - L_{i-1/2} - L_{i+1/2}) Y_i^j + L_{i+1/2} Y_{i+1}^j,$$

$$i = 2, 3, .., M \tag{B.34}$$

$$\begin{aligned} D_1 &= -A_1 T_0 + L_{1/2} Y_0^j + (Z_1 - L_{1/2} - L_{3/2}) Y_1^j + L_{3/2} Y_2^j \\ &= L_{1/2} Y_0^j + L_{1/2} Y_0^j + (Z_1 - L_{1/2} - L_{3/2}) Y_1^j + L_{3/2} Y_2^j \end{aligned} \tag{B.35}$$

$$T_i = Y_i^{j+1}. \tag{B.36}$$

Since the following conditions are satisfied:

$$\begin{aligned} B_i &> 0, \qquad i = 1, ..., M \\ B_1 &> |C_1| \\ B_i &\geq |C_i| + |A_i|, \quad \text{and } A_i \neq 0, C_i \neq 0 \text{ for } i = 2, 3, ..., M-1 \\ B_M &\geq |A_M| \end{aligned} \tag{B.37}$$

the solution can be written as:

$$\begin{aligned} b_1 &= \tfrac{C_1}{B_1}, \quad b_i = \tfrac{C_i}{B_i - A_i b_{i-1}}, \quad i = 2, 3, ..., M-1 \\ q_1 &= \tfrac{D_1}{B_1}, \quad q_i = \tfrac{D_i - A_i q_{i-1}}{B_i - A_i b_{i-1}}, \quad i = 2, 3, ..., M \\ T_M &= q_M, \quad T_i = q_i - b_i T_{i+1}, \quad i = M-1, M-2, ..., 1. \end{aligned} \tag{B.38}$$

B.5 Source code

The source code for the program, written in ANSI C, is listed below.

```
#include <stdio.h>
#include <stdlib.h>
#include <string.h>
#include <sys/types.h>
#include <math.h>

#define AS 1000            /*  array size of A, B, C, etc.  */
#define DT 0.1             /*  time step size  */
#define dx 1.0             /*  space step size  */
#define N0 5.00e22         /*  equilibrium cluster constant, in atoms/cm^3*/
#define n0 1.0             /*  # of atoms in the smallest nuclei  */
#define GV .10             /*  volume free energy in eV  */
#define GS .15             /*  surface free energy in eV  */
#define V0 1e15
#define EA 2.75            /*  activation energy for SPE  */
#define kTC(x) (8.617e-5 * (x+273.15))  /*  kT at x degree C in eV */
#define SHAPE 4.0          /* shape factor, 4.836 for sphere, 4.0 from */
                           /* Kelton et al. */
```

```
double A [AS], B [AS], C[AS], D [AS], W [AS], Y[AS], L [AS];

double x(double);
double Z (double);
double dG (double);
double kn (double);
double flux (int);

double t, kT, test, kT1, kT2, gs, gv, dt, Ea, v0;
long icn, ict, T1, T2, of;

void init (void);
void init_var (void);
void write_file (char *filename, double time);
int set_var (int i);
void calculate_D (void);
void solve_for_Y (void);
void calculate_L (void);
void calculate_W (void);
void calculate_Y (void);
void calculate_ABC (void);
int set_const(char *name);

char filename [100];
char drdtfile [100];

struct i_variable
{
    char  name[2];
    long *var;
};

struct f_variable
{
    char  name[2];
    double *var;
};


struct i_variable i_varlist[] =
{
    "cn", &icn, "ct", &ict, "T1", &T1, "T2", &T2, "of", &of
};

struct f_variable f_varlist[] =
{
    "gs", &gs, "gv", &gv, "dt", &dt, "Ea", &Ea, "v0", &v0
};

#define IVARS (sizeof(i_varlist) / sizeof(struct i_variable))
#define FVARS (sizeof(f_varlist) / sizeof(struct f_variable))
```

```
main (int argc, char *argv[])
{
    int i, j, iterations, fname_length;
    int ipertstep, jpertstep;
    FILE *nc_64, *nc_900, *drdt, *file_cluster, *file_flux;
    double I;

    if (argc < 3)
    {
        printf("Usage:\n\t nc2_3D iterations filename v1=xx v2=yy ...\n");
        printf("\nVariables are:\n\t");
        for (i = 0; i < IVARS; i++)
             printf("%c%c  ", i_varlist[i].name[0], i_varlist[i].name[1]);
        for (i = 0; i < FVARS; i++)
            printf("%c%c  ", f_varlist[i].name[0], f_varlist[i].name[1]);
          exit(0);
    }

    init_var();

    /* set the variables from the strings on the command line
    For example, the function set_const() takes the string "VM=3.14" and sets
    the variable Vm to 3.14 */

    for (i = 3; i < argc; i++)
        set_const(argv[i]);

    init ();

    iterations = atol (argv[1]);
    ipertstep = iterations / 1000;
    jpertstep = ipertstep * 10;
    fname_length = strlen (argv[2]);
    strcpy (filename, argv[2]);

    strcpy (filename+fname_length, "_64.dat");
    nc_64 = fopen (filename, "w");
    strcpy (filename+fname_length, "_900.dat");
    nc_900 = fopen (filename, "w");
    strcpy (filename+fname_length, "_n.dat");
    file_cluster = fopen (filename, "w");
    strcpy (filename+fname_length, "_f.dat");
    file_flux = fopen (filename, "w");


    fprintf (nc_64, "/* n = %g\n/* t\t I(n)\n", x(63+.5));
    fprintf (nc_900, "/* n = %g\n/* t\t I(n)\n", x(899+.5));

    fprintf(file_cluster, "/* x0 = %g\t x1 = %g \t t0 = %g\t t1 = %g\n",
            x(0), x(990), 0.0, (iterations - 1) * dt);
    fprintf(file_flux, "/* x0 = %g\t x1 = %g \t t0 = %g\t t1 = %g\n",
            x(0), x(990), 0.0, (iterations - 1) * dt);
```

```
    for (i = 0; i < iterations; i++)
    {

        set_var (i);

        t = i * dt;

        if ((i % jpertstep) == 0)
        {
            for (j = 0; j < 100; j++)
            {
                fprintf(file_cluster, "%g ", Y[j*10] * Z(x(j*10)));
                fprintf(file_flux, "%g ", flux(j*10));
            }
            fprintf(file_cluster, "\n");
            fprintf(file_flux, "\n");
        }
        if ((i % ipertstep) == 0)
        {
            I = flux (63);
            fprintf (nc_64, "%g\t %g\n", t, I);

            I = flux (899);
            fprintf (nc_900, "%g\t %g\n", t, I);
        }

        calculate_D ();
        solve_for_Y ();
    }

    strcpy (drdtfile, argv[2]);
    strcat (drdtfile, "_drdt.dat");
    drdt = fopen (drdtfile, "w");
    for (i = 0; i < AS; i++)
        fprintf (drdt, "%g\t %g\n", x(i), kn(x(i)));

    return(0);
}


double x (double i)
{
    return (n0 + i*dx);

}


double Z (double x)
{
    return (N0 * exp (-dG (x) / kT));
}
```

```
double dG (double x)
{

    return (-gv * x + SHAPE * gs * pow (x, 2.0/3.0));
}


double kn (double x)
{
    double gamma;

    gamma = v0 * exp (- Ea / kT);
    return (SHAPE * pow (x, 2.0/3.0) * gamma * exp (.5 * (dG(x) - dG(x+1)) / kT));
}


/* flux() calculates the flux of clusters across cluster size x(i),
   where i is the bin number, or array index */

double flux (int i)
{
    return ((kn(x(i+.5)-.5) * Z(x(i+.5)-.5) * (Y[i]-Y[i+1])) / dx);
}


void calculate_L (void)
{
    int i;

    for (i = 1; i < AS; i++)
        L [i] = dt / 2.0 / dx / dx * kn (x(i-.5)-.5) * Z (x(i-.5)-.5);

}


void calculate_ABC (void)
{
    int i;

    calculate_L();

    for (i = 1; i < AS - 1; i++)
    {
        A [i] = - L [i];
        B [i] = Z (x(i)) + L [i] + L [i+1];
        C [i] = - L [i+1];
    }
}


void init (void)
{
    int i;
```

```
    if (T1 != 0)
    {
        kT1 = kTC(T1);
        kT2 = kTC(T2);
        kT = kT1;
    }
    else
        kT = kTC(600);

    W [0] = N0;
    Y [0] = W[0]/Z(x(0));

    calculate_ABC();

    for (i = 1; i < AS - 1; i++)
    {
        Y [i] = W [i] = 0;
    }

    Y [AS-1] = W [AS-1] = 0;
}


void init_var (void)
{
    t = 0.0;
    gs = GS;
    gv = GV;
    dt = DT;
    Ea = EA;
    v0 = V0;
}


void calculate_D (void)
{
    int i;

    for (i = 1; i < AS - 1; i++)
        D [i] = L [i] * Y [i-1] + (Z (x(i)) - L [i] -
                L [i+1]) * Y [i] + L [i+1] * Y [i+1];

    D [1] = D [1] + L [1] * Y [0];
}


void calculate_W (void)
{
    int i;

    for (i = 1; i < AS - 1; i++)
        W [i] = Y[i] * Z(x(i));
```

```
}


void calculate_Y (void)
{
    int i;

    for (i = 0; i < AS - 1; i++)
        Y [i] = W[i] / Z(x(i));
}


void solve_for_Y (void)
{
    static double b [AS - 1], q [AS - 1];
    double den;
    int i;

    b [1] = C [1] / B [1];
    q [1] = D [1] / B [1];

    for (i = 2; i < AS - 1; i++)
    {
        den = B [i] - A[i] * b[i-1];
        b [i] = C [i] / den;
        q [i] = (D [i] - A [i] * q [i-1]) / den;
    }

    Y [AS - 2] = q [AS - 2];
    for (i = AS - 3; i > 0; i--)
        Y [i] = q [i] - b [i] * Y [i+1];
}


void write_file (filename, time)
char *filename;
double time;
{
    FILE *nc_out;
    int i;
    double I;

    nc_out = fopen (filename, "w");
    fprintf (nc_out, "/*  t = %g sec\n", time);
    fprintf (nc_out, "/*  n \t N(n) \t I(n)\n");

    for (i = 0; i < AS - 1; i++)
    {
        I = flux (i);
        fprintf (nc_out, "%g\t%g\t%g\n", x(i), Y[i] * Z (x(i)), I);
    }
    fprintf (nc_out, "%g\t%g\t%g\n", x(i), Y[i] * Z (x(i)), 0.0);
```

```
    fclose (nc_out);
}


int set_var (int i)
{
    int j;

    if (icn != 0 && i == ict)
    {
        for (j = 1; j < icn; j++)
            Y[j] = 0.0;
    }


    if (T1 !=0)
    {
        if ((i % of) == 0 && i != 0)
        {
            /* Before T or gs or gv is changed we must calculate W */
            calculate_W();

            if (kT == kT1)
                kT = kT2;
            else
                kT = kT1;

            /* After T or gs or gv is changed we must recalculate Y and A, B, C */
            calculate_Y();
            calculate_ABC();
        }
    }

    return (0);
}


/*
    set_const() takes a string like "VM=3.14" and set the variable Vm to 3.14
*/
int set_const(char *name)
{
    int i;

    for (i = 0; i < IVARS; i++)
        if (name[0] == i_varlist[i].name[0] && name[1] == i_varlist[i].name[1])
        {
            *(i_varlist[i].var) = atol(&name[3]);
            printf("%c%c = %d\n", name[0], name[1], *(i_varlist[i].var));
            return(0);
        }
    for (i = 0; i < FVARS; i++)
```

```
        if (name[0] == f_varlist[i].name[0] && name[1] == f_varlist[i].name[1])
        {
           *(f_varlist[i].var) = atof(&name[3]);
               printf("%c%c = %g\n", name[0], name[1], *(f_varlist[i].var));
           return(0);
        }

    printf("\nVariable %c%c not found!\n", name[0], name[1]);
    exit(0);
}
```

Bibliography

[1] D. T. Wu, J. Chem. Phys. **97**, 1922 (1992).

[2] W. Press, B. Flannery, S. Teukolsky and W. Vetterling, *Numerical Recipes in C* (Cambridge University Press, New York, 1988).